



**WIND TUNNEL STUDY OF INTERFERENCE EFFECTS RELATING TO AFT  
SUPERSONIC EJECTION OF A STORE**

THESIS

Timothy P. Jung, Major, USAF

AFIT/GAE/ENY/06-04

**DEPARTMENT OF THE AIR FORCE  
AIR UNIVERSITY**

**AIR FORCE INSTITUTE OF TECHNOLOGY**

---

---

**Wright-Patterson Air Force Base, Ohio**

APPROVED FOR PUBLIC RELEASE; DISTRIBUTION UNLIMITED

The views expressed in this thesis are those of the author and do not reflect the official policy or position of the United States Air Force, Department of Defense, or the U.S. Government.

AFIT/GAE/ENY/06-04

**WIND TUNNEL STUDY OF INTERFERENCE EFFECTS RELATING TO AFT  
SUPERSONIC EJECTION OF A STORE**

THESIS

Presented to the Faculty

Department of Aeronautics and Astronautics

Graduate School of Engineering and Management

Air Force Institute of Technology

Air University

Air Education and Training Command

In Partial Fulfillment of the Requirements for the  
Degree of Master of Science in Aeronautical Engineering

Timothy P. Jung, BS

Major, USAF

December 2005

APPROVED FOR PUBLIC RELEASE; DISTRIBUTION UNLIMITED

AFIT/GAE/ENY/06-04

**WIND TUNNEL STUDY OF INTERFERENCE EFFECTS RELATING TO AFT  
SUPERSONIC EJECTION OF A STORE**

Timothy P. Jung, BS

Major, USAF

Approved:

\_\_\_\_\_  
Dr. Mark F. Reeder (Chairman)

\_\_\_\_\_  
Date

\_\_\_\_\_  
Raymond C. Maple, Lt Col, USAF (Member)

\_\_\_\_\_  
Date

\_\_\_\_\_  
Richard J. McMullan, Major, USAF (Member)

\_\_\_\_\_  
Date

## **Abstract**

An investigation into the issues surrounding the release of a store into a supersonic wake was conducted. A 10-degree half-angle cone was used to model the carrier vehicle and a 10-degree half-angle cone 42% smaller was used to model the store. The experiments were conducted at a freestream Mach number of 2.93 and at zero degrees angle of attack. Real-time sequences of Schlieren images were used to obtain a visual understanding of these effects. Fast-response pressure transducers and pressure-sensitive paint (PSP) provided pressure information on the carrier vehicle and store models.

This study analyzed the effects of a diamond-shaped strut mounted under the wind tunnel model. Visualizations showed the strut caused the reattachment shock to move closer to the base. The transducers recorded a slight mean pressure drop and an increase in standard deviation of pressure behind the strut. From a PSP profile image, the interaction of the oblique shock of the strut with the model's conical shock was found to create a vertical pressure gradient. However, base pressure was only modestly affected.

Research was conducted on the effects of a store at various positions in the wake. The store caused the pressure to rise as the store moved aft. At distance equal to half of the vehicle's base diameter, the store had maximum effect, causing an increase in the base's coefficient of pressure.

The cavity, simulating a weapons bay in the carrier vehicle, was found to have minimal effects on the flowfield. However, the vehicle model with a cavity did have a lip shock that was not present for a solid vehicle of same geometry. Also, the cavity caused a drop in the vehicle's base pressure, which is opposite of the documented effect of a cavity at sub-sonic speeds. The cavity also lowered the pressure on the surface of the store in the near wake. A frequency analysis of the pressure fluctuations in the cavity was performed. When the store was inserted into the cavity it excited a characteristic frequency corresponding to a Strouhal number of 0.25.

AFIT/GAE/ENY/06-04

*To my family, for allowing me to pursue my dreams*

## Acknowledgments

I would like to express my sincere appreciation to my faculty advisor, Dr Reeder. I appreciated Dr. Reeder's expert help. However, more than that, I enjoyed his enthusiasm and compassion. I would also like to thank my sponsor, Dr. Rudy Johnson from the AFRL/VA for the support that made this research possible. Also, I would like to acknowledge the Ohio Center of Advanced Propulsion and Power who provided funding for the high-speed camera used in this thesis. A big thanks also goes out to Dr. Jim Crafton, the pressure-sensitive paint *guru*, from Innovative Scientific Solutions, Inc. I am thankful toward Dr. Crafton for taking the time to educate me and providing me the intellectual tools required complete this project. I would also like to acknowledge Lt John "McFly" McElroy, USN for the concept of transforming information from Schlieren images into the frequency domain. This thesis would not have happened if not for the dedication of the lab technicians. Jay Anderson leads a great team. No one ever said, "That is not my job." Everyone was eager to help. The MVP of this team was Mr. Andy Pitts. He put up with a very complex test set-up and he never took an easy way out. Most of all I would like to thank him for letting me do it *my way*.

Timothy P. Jung



## Table of Contents

	Page
Abstract .....	v
Dedication .....	vii
Acknowledgments.....	viii
Table of Contents .....	ix
List of Figures .....	xi
List of Tables .....	xv
List of Symbols .....	xvi
I. Introduction .....	1
Section 1- Motivation .....	1
Section 2 – Overview of Test Equipment.....	2
Section 3 - Research Focus and Goals .....	4
Section 4 - Preview.....	7
II. Literature Review .....	8
Section 1 - Chapter Overview .....	8
Section 2 – Supersonic Base Flow Overview.....	8
Section 3 – Research Concerning Experimental Methods .....	10
Section 4 – Research Concerning the Store’s Effects .....	14
Section 5 – Research Concerning the Effects of a Cavity.....	19
Section 6 – Research Concerning Frequency Signals in a Supersonic Wake .....	20
III. Methodology .....	22
Section 1 - Wind Tunnel System.....	22
Section 2 - Wind Tunnel Models and Geometry .....	24
Section 3 - Schlieren Imaging System.....	28

	Page
Section 4 - Pressure Transducers and Data Acquisition.....	32
Section 5 - Pressure-Sensitive Paint .....	34
Section 6 – Power Spectrum Density from Schlieren Images.....	39
IV. Analysis and Results.....	41
Section 1 – Model Design Validation .....	41
Section 2 – Evaluation of a Diamond-Shaped Strut.....	48
Section 3 – Analysis of the Effects of the Store .....	59
Section 4 - Analysis of the Effects of a Cavity .....	67
Section 5 – Frequency Analysis .....	76
V. Conclusions and Recommendations .....	86
Section 1 - Conclusions of Research .....	86
Section 2 - Recommendations for Future Research .....	88
Appendix A: Pressure Transducer Specifications.....	91
Appendix B: Additional Schlieren Images .....	94
Appendix C: Profile Views of Various Vehicle Models .....	96
Bibliography .....	98

## List of Figures

	Page
Figure 1: Vehicle and store models in AFIT's supersonic wind tunnel .....	3
Figure 2: Supersonic base flow (10:19) .....	9
Figure 3: Martellucci and Agnone's wind tunnel models used to investigate supersonic wakes (reproduced from Reference 17:386) .....	11
Figure 4: Wind tunnel support used by Burt et al. (reproduced from Reference 4) .....	13
Figure 5: Base $C_p$ verses radial distance from experimental methods (reproduced from Reference 10) .....	18
Figure 6: Velocity profile ( $U/U_\infty$ ) in a supersonic wake of a cylinder (reproduced from Reference 10:20) .....	19
Figure 7: PSD profiles from transducers on the base of a cylinder (reproduced from Reference 14) .....	21
Figure 8: AFIT's supersonic wind tunnel .....	23
Figure 9: Vehicle wind tunnel models: (a) cavity, (b) solid .....	25
Figure 10: Vehicle model was secured in wind tunnel by inserting square block into cavity in the floor of wind tunnel .....	26
Figure 11: Model of store .....	26
Figure 12: Store model in the tunnel. The store model was mounted on a treaded rod, which allowed easy placement at various axial positions .....	27
Figure 13: Non-dimensionalizing axial position.....	28

Figure 14: Examples of Schlieren images of store at $x/D = 0.48$ : (a) 20.1 kfps, not averaged, (b) 20.1 kfps, averaged over 100 frames, (c) 94,500 fps, not averaged ....	31
Figure 15: Schlieren image of empty wind tunnel operated at Mach 2.93; flow is from right to left.....	31
Figure 16: Kulite pressure transducers: (a) in recessed slot in the store, (b) on the top wall of the cavity of the vehicle model .....	33
Figure 17: Generic PSP System (reproduced from Reference 5) .....	35
Figure 18: Pressure response for ISSI's Binary FIB paint (reproduced from Reference 20) .....	38
Figure 19: Possible wind tunnel configurations to study base flow .....	41
Figure 20: AFIT's wind tunnel nozzle is not symmetric .....	43
Figure 21: Schlieren images of first-generation vehicle models .....	45
Figure 22: Schlieren images of second-generation vehicle models.....	46
Figure 23: Model with a support similar to Configuration A: (a) Schlieren image, (b) profile view of model design.....	47
Figure 24: Schlieren image of store model with excellent symmetry .....	48
Figure 25: Schlieren images of two identical models except size of diamond strut: (a) 25 mm strut, (b) 35 mm strut .....	50
Figure 26: $C_p$ of store verses angular position of transducer .....	51
Figure 27: Schlieren images which correspond to the pressure transducer data in Figure 26: (a) cavity at $x/D = 0$ , (b) cavity at $x/D = 0.22$ , (c) solid at $x/D = 0.22$ .....	52
Figure 28: Standard deviation ratio of store pressure verses angular position .....	53

Figure 29: PSP profile view of support and vehicle model .....	54
Figure 30: PSP profile view of support and vehicle model with scale changed to highlight the pressure gradient on the rear of the cone caused by the strut .....	55
Figure 31: Schlieren image of solid vehicle used to estimate expansion angle.....	56
Figure 32: PSP pressure profile of the base of the vehicle with the store at $x/D = 2.2$ ...	57
Figure 33: Comparison of PSP base pressure profile to theory and experimental data...	58
Figure 34: (a) PSP of store at $x/D = 0.92$ trailing solid vehicle, (b) associated Schlieren image .....	59
Figure 35: Schlieren images of the store behind the vehicle model with a cavity at various axial positions.....	60
Figure 36: Schlieren images of the store behind the solid vehicle model at various axial positions .....	61
Figure 37: Carrier vehicle base $C_p$ versus store's distance .....	63
Figure 38: Pictorial representation of the store's apparent affect on the streamlines (streamlines not to scale).....	65
Figure 39: Standard deviation ratio of vehicle base pressure versus distance.....	66
Figure 40: Vehicle base pressure profiles for various store positions (from PSP) .....	67
Figure 41: Schlieren images of initial vehicle models: (a) solid, (b) cavity .....	68
Figure 42: Schlieren images of final vehicle models: (a) solid, (b) cavity .....	69
Figure 43: Schlieren images of vehicle models: (a) solid model with no lip shock, (b) cavity model with lip shock .....	70

Figure 44: Cavity verses solid vehicle model: (a) base pressure, (b) store pressure, (c) vehicle base pressure standard deviation ratio, (d) store pressure standard deviation ratio .....	73
Figure 45: PSP profiles of the store at various axial positions .....	75
Figure 46: Pressure on the store from PSP images: (a) $x/D = 0.22$ , (b) $x/D = 0.92$ .....	76
Figure 47: Sample time trace of vehicle's cavity pressure with store at $x/D = 0$ .....	78
Figure 48: PSD from cavity transducer: (a) $x/D = -1.5$ , (b) $x/D = -0.92$ , (c) $x/D = 0$ , (d) $x/D = 0$ with no data acquisition feedback.....	80
Figure 49: Sample time trace of pixel intensity over time from a Schlieren image .....	81
Figure 50: Schlieren images of solid vehicle model taken at 94.5 kfps. Xs on first image indicate locations investigated using Schieren PSD technique.....	83
Figure 51: Schlieren images of solid vehicle model with store at $x/D = 0.22$ , taken at 94.5 kfps. Xs on first image indicate locations investigated using Schieren PSD technique .....	84
Figure 52: Schlieren PSDs based off of 10,000 images: (a) $x/D = 0.22$ for cavity model and no store, (b) $x/D = 0.22$ for solid model and no store, (c) $x/D = 2.0$ for solid model and no store, (d) $x/D = 0.22$ for solid model with store at $x/D = 0.22$ .....	85

## **List of Tables**

Page

Table 1: Comparison of PSD processes.....	77
---	----

## List of Symbols

- A -- Term used to calculate the base pressure coefficient in the corrector step (from method developed in Reference 26)
- B -- Term used to calculate the base pressure coefficient in the corrector step (from method developed in Reference 26)
- C<sub>p</sub> -- Coefficient of pressure
- C<sub>p,B</sub> -- Coefficient of base pressure which accounts for variations in thinness ratio (L/h) and Reynolds number (from Reference 26)
- C<sub>p,esc</sub> -- Coefficient of base pressure which accounts for Mach number variations (from Reference 26)
- D -- Diameter of the vehicle model's base
- L -- Length of cone
- h -- Radius of cone (height)
- k -- Constant of proportionality equating refractive index to density
- $M_{\infty}$  -- Freestream Mach number
- $M_1$  -- Mach number after the cone's expansion wave (in the inviscid outer region)
- n -- Refractive index
- $n_o$  -- Refractive index of surrounding gas
- p -- Pressure
- $p_{\infty}$  -- Freestream pressure
- Re<sub>L</sub> -- Reynolds number calculated using the length of a cone
- x -- Distance from the base of the vehicle model to the tip of the store
- y -- Vertical distance from the wind tunnel's centerline
- $\varepsilon_x$  -- Optical deflection angle



$\gamma$  -- Ratio of specific heats

$\rho$  -- Density

# **WIND TUNNEL STUDY OF INTERFERENCE EFFECTS RELATING TO AFT SUPERSONIC EJECTION OF A STORE**

## **I. Introduction**

### **Section 1- Motivation**

Future military attack vehicles will be employed at supersonic or hypersonic speeds, possibly releasing their weapons from a rear cavity. As can already be seen in the latest generation of attack aircraft, F/A-22, B-2, etc., future attack vehicles will not have external stores. Stealth and drag drive this design decision (22:186-188). However, unlike current aircraft, which release their weapons from a bay under the aircraft, this may not be practical for the next generation aircraft. A weapon bay door opening in the freestream greatly increases drag and radar cross sectional area. The weapon must transition through the highly unsteady bomb bay and then transverse a free-shear layer and finally a shock (20:1). It is possible to avoid these problems by releasing the weapons out the back into the subsonic near-wake. In addition to stealth and drag benefits, this design would allow the structure in the belly of the aircraft to be optimized for strength and thermal protection. In addition, the near-wake is a relatively benign environment compared to under the vehicle. The near wake is subsonic, thus the store will initially have low drag and negligible aerodynamic heating (2:3). Therefore, the next generation of attack aircraft may use an aft ejection concept to employ their weapons at supersonic speeds.

The aft supersonic ejection is not without its share of problems. An object released from a rear cavity will initially be in a subsonic recirculation region. The store will not have a leading shock. Since the attack aircraft or *carrier vehicle* has a shock and the store does not, the carrier will have higher drag. The combination of the reverse flow and low drag may prevent a clean release and cause the store to impact the carrier vehicle. As the store moves through the near wake it will influence the wake by entrainment and displacement. At some distance from the carrier, the store will enter supersonic flow and the two objects will no longer influence one another.

In order to simulate this aft ejection in a wind tunnel, it is critical that the wake behind the vehicle be as close as possible to a wake without any support. Traditional wind tunnel experiments use stings mounted from the rear of the wind tunnel models. This allows the flow to traverse the model as it would in free flight. The only interference from the sting is in the flow behind the model and around the sting. This traditional design is incompatible with an aft ejection study because the sting is in the main area of interest. If the sting is relocated to the bottom or front of the model it will still disturb the flow behind it, and thus the wake. Therefore, a support system needs to be developed that will minimize these effects.

## **Section 2 – Overview of Test Equipment**

In order to study the aft ejection concept, wind tunnel experiments were performed in AFIT's supersonic wind tunnel. The results obtained in this study will be combined with a separate CFD analysis using the same geometry. The combination of

the two studies should create a comprehensive analysis of the supersonic aft ejection concept. Since the goal of this research was to gain a fundamental understanding of the problem, a 10-degree half-angle cone was used to model both the vehicle and the store. This geometry allowed easy comparison to previous research. The models set up in the wind tunnel can be seen in Figure 1. Two models were created to simulate carrier vehicles. The first was a solid cone used to obtain a base pressure profile on the rear of the cone. The second had an aft cavity to simulate a weapons bay. Both models had a 21.75 mm base. A diamond-shaped strut replaced the conventional sting. This strut was mounted to the bottom of the model and was secured to the test section floor. The vehicle models were made from photopolymer resins in a 3D printer. The store was also simulated using a 10-degree half-angle cone, but was 42% smaller. The store used a threaded rod as a sting, which allowed manual relocation to a variety of positions. The store was made from stainless steel.

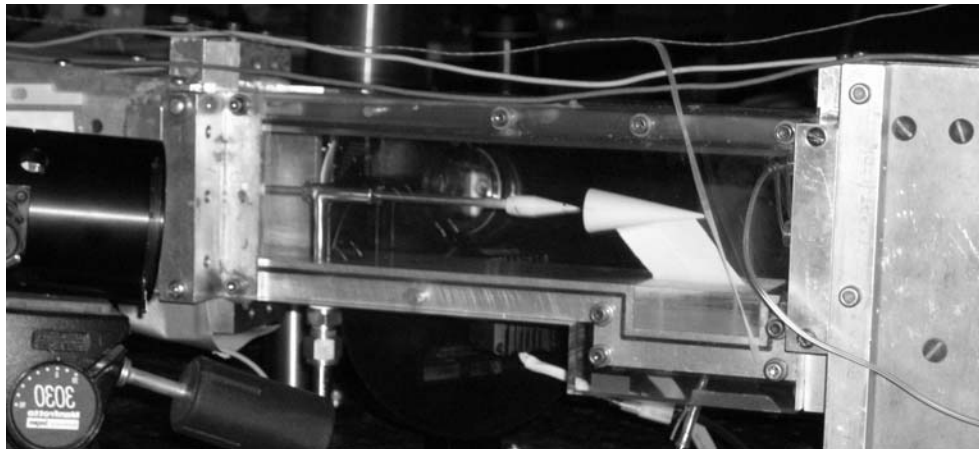


Figure 1: Vehicle and store models in AFIT's supersonic wind tunnel

The tests were accomplished in AFIT's supersonic wind tunnel at Mach 2.93 and nominal test section pressure of 1.2 psi. One pressure transducer was used in the vehicle's cavity and another was in a slightly recessed slot on the side of the store model. These transducers served two purposes. They provided insight into how the store interacted with the flow as well as a way to validate pressure-sensitive paint (PSP) data. The transducers and PSP complemented each other. The PSP system provided only mean pressure, but over the entire model. On the other hand, the transducers provided time-accurate data up to a frequency of 50 kHz, but only at a point. In addition to the pressure data obtained from the PSP and the transducers, Schlieren images were also taken to provide a global picture of the flowfield. The combination of the three: pressure transducer data, PSP and Schlieren images, provided a comprehensive study of the flowfield between the vehicle and store, as well as the effects of the wind tunnel support.

### **Section 3 - Research Focus and Goals**

The research conducted was limited in scope to answer the following questions:

- Can a strut based on diamond geometry be used effectively for wake studies?
- What are the effects of the store on the wake?
- What changes when a cavity is added to the leading vehicle?
- What is the frequency of the pressure variations in the wake?

The discussion below will examine each one of these questions in detail.

### ***Use of a Diamond-shaped Strut.***

Before one can study the effects of the store, one needs to have a way to mount a model in a wind tunnel that approximates flow without the support. This research used a diamond strut mounted under the vehicle model. This support needed to have minimal effect on the region of interest, the wake. The Jet Propulsion Laboratory (JPL) wake research from the 1960s stated, “Any use of wires or other seemingly insignificant supports for wake studies, must be proven to be acceptable, as they can produce a noticeable wake effect (7:22).” Therefore, first a qualitative study was performed using Schlieren photography. The JPL study noted that the effect of wires or mounts was to move the reattachment point of the wake closer to the vehicle (7:3). Therefore, similar visual checks were performed. Then, pressure transducer data was taken on the store at a variety of radial positions. A wake behind a cone at no angle of attack is axisymmetric. Therefore, if all radial positions had similar pressure profiles, then that was an indication of good axisymmetric flow, and a non-intrusive support. Finally, PSP images of the vehicle and store showed any pressure gradients caused by the strut. Any non-axisymmetric trends in these PSP images were caused by the support. By combining the three above tests, general conclusions were made concerning the diamond strut’s usefulness in wake studies.

### ***Effects of the Store on the Wake.***

During a release, the store affects the flowfield. To gain a better understanding of these changes, Schlieren photographs were taken with and without a stationary store present at various positions aft of the carrier vehicle. By comparing these cases, it

provided an initial indication as to the store's effects. Simultaneous to the Schlieren pictures, pressure transducer data was taken from the vehicle as well as the store. Since the only variation was in the position of the store, changes in pressure data were attributed to the change in store's position. Finally, PSP images of the base of the cone were taken at various positions. Again, any changes were attributed to the store's position. By analyzing all these tests, a basic understanding of the store-to-wake interaction was obtained.

### ***Effects of a Cavity.***

The same procedures as outlined above for analyzing the store were accomplished, except with a vehicle model that had an aft cavity. By comparing these results to those obtained without a cavity, insight was gained into the impact of having an open cavity in a supersonic wake containing a store.

### ***Frequency of Pressure Fluctuations.***

Two techniques were used to access the frequency present in the wake. First, the pressure transducer data obtained to answer the above questions was transformed into a Power Spectrum Density (PSD) graphs. Second, thousands of frames of Schlieren images were compiled into compressed movies. The change in intensity of a given pixel is associated with a change in the density gradient. Thus, by tracking a given point's intensity over the length of the avi file, the change in density gradient was tracked. This information was then transformed into the frequency domain. The two above methods allowed general conclusions to be made about the frequencies the store experienced in the cavity and the wake.

## **Section 4 - Preview**

This chapter has specified the starting point of this thesis. Chapter II provides a thorough summary of pertinent research already conducted on supersonic base flow. Then, in Chapter III the reader will find a thorough discussion of the theory and techniques used in this research. This chapter includes sections on AFIT's wind tunnel, Schlieren photography, pressure transducers and data acquisition, PSP system and Schlieren frequency analysis. Chapter IV presents the results and analysis in graphical and textual form. Finally, Chapter V contains relevant findings and conclusions.



## **II. Literature Review**

### **Section 1 - Chapter Overview**

This chapter summarizes the research that has been conducted to date concerning relevant topics in supersonic base flow. The chapter starts with an overview, which defines features of supersonic base flow. Then, the chapter breaks up research into categories associated with the four questions asked in Chapter I. The first area of interest is the use of a diamond-shaped strut to study base flows. Thus, Section 3 of this chapter contains research associated with how previous researchers set up their wind tunnel to study base flows. Likewise, Section 4 offers research that helped predict the store's impact on the wake. Section 5 contains research associated with a cavity and Section 6 describes relevant research concerning frequency content in a supersonic wake.

### **Section 2 – Supersonic Base Flow Overview**

Base flow refers to the flow in the *near wake* region of a body. Figure 2 illustrates the supersonic base flow of a cone. When the cone abruptly ends, the supersonic flow attempts to remain attached and turns toward the axis of symmetry, creating an expansion fan. However the angle is too great and the flow separates. A triangle shaped, subsonic recirculation region is created behind the cone. Within this region, the flow at the centerline is in the opposite direction of the freestream. As one moves downwind on the centerline from the base, eventually the flow is zero. This location is defined as the *stagnation point*. As one continues downwind, the flow is still

subsonic, but in the same direction as the freestream. Eventually it reaches sonic conditions, which is referred to as the *sonic point*.

The recirculation region is separated from the inviscid outer region above it by a free-shear layer. As this shear layer approaches the axis of symmetry it is turned parallel

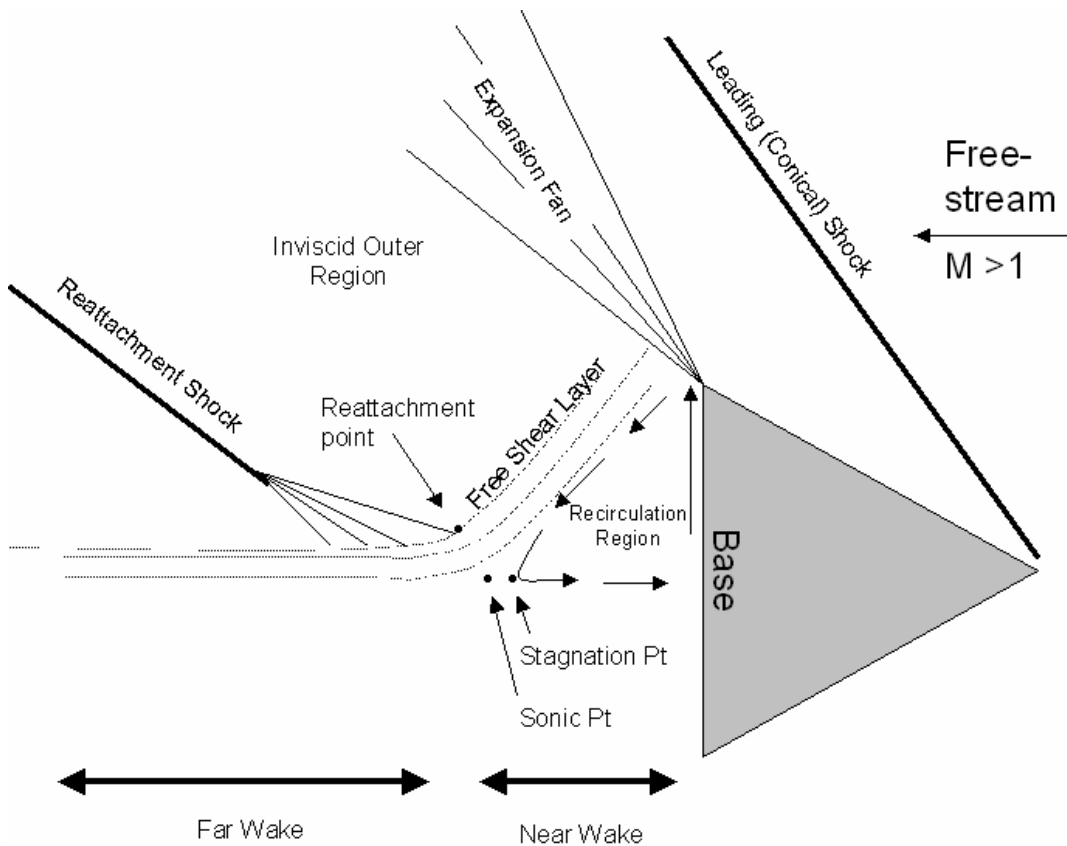


Figure 2: Supersonic base flow (10:19)

to the freestream flow. This turning of the flow into itself creates a series of recompression or *reattachment shocks*, sometimes called the trailing shocks. A fluid element passing through these shocks experiences a large adverse pressure gradient.

Beneath the trailing shock, the *far wake* begins to grow (12:77-78). The far wake is beyond the scope of this research. For the purpose of this research the *reattachment point* has been defined as the point where the reattachment shocks form.

### **Section 3 – Research Concerning Experimental Methods**

During the 1960s several wind tunnel experiments were conducted to study supersonic wakes of cones and spheres (see References 7, 8 and 9). Many of these studies were *free-flight* experiments, which allowed the model to be released in the wind tunnel with no support. This method offered an excellent way to take Schlieren images of the wakes with no sting interference. Also of interest, before the models were released, 0.020-inch vertical wires supported the models. Schlieren pictures of models supported by these wires were obtained and compared to the free flight images. This analysis demonstrated that although the wires were thin, the wires had a significant effect on the wake. In fact, these studies showed a 20% reduction in the distance from the base of the cone to the reattachment point due to the wires (8:11). This indicates that any support system used for wake studies needs to be carefully designed and that the reattachment point can be used to evaluate the support's intrusiveness.

Research conducted by Martellucci and Agnone offered other ideas on how to support a wind tunnel model. In 1966 they conducted wind tunnel tests at Mach 6 to learn about the wakes of cones. Figure 3 contains two designs that they used. The first design, seen in Figure 3(a), used a strut mount and will be referred to as Configuration A. The rod extended 11.5 inches to the front of the cone. Then the rod was secured by a

strut mounted to the floor in the supersonic portion of the tunnel. To stabilize the back of the model, three 0.030-inch wires extended from the base to the tunnel walls. The second design, seen in Figure 3(b), and referred to as Configuration B, used a support similar to the first. Configuration B differed from A in that the rod used in B extended through the nozzle and was bolted in the subsonic portion of the wind tunnel. This design produced no shocks. Also instead of wires, three 0.010-inch thick bands stabilized the aft of the model. These bands were 0.25 inches long with sharp leading edges. Martellucci and Agnone concluded that Configuration B was the superior design. According to their

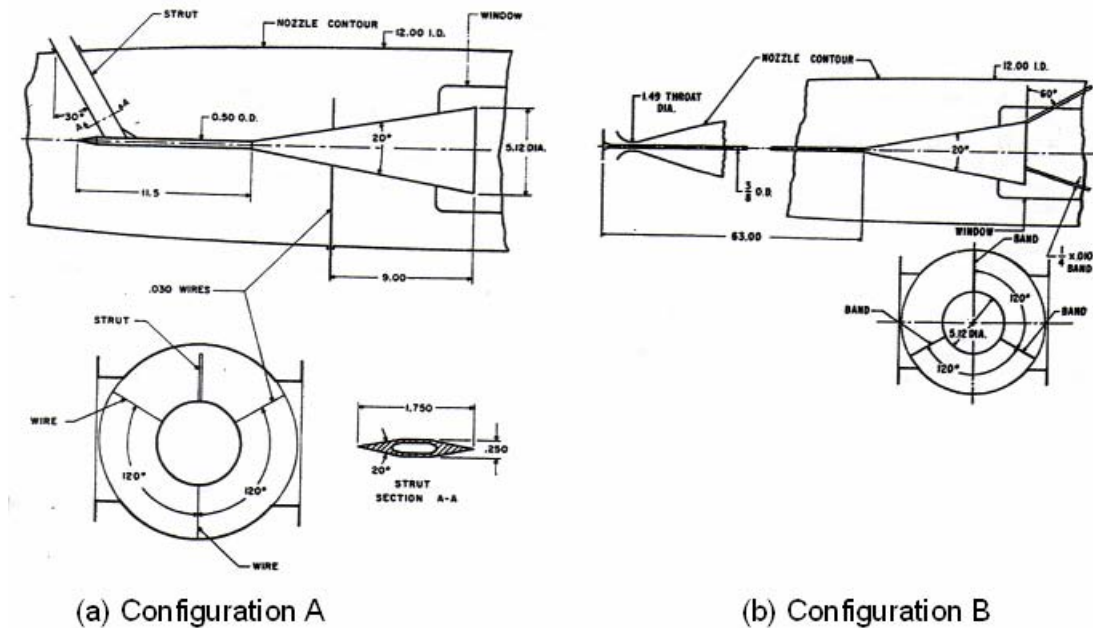


Figure 3: Martellucci and Agnone's wind tunnel models used to investigate supersonic wakes (reproduced from Reference 17:386)

research, a major downfall of Configuration A was the wires on the back of the model. Compared to the wires, the bands used on Configuration B produced no noticeable wake.

Similar to the JPL studies, they also found that any support interference manifested itself in moving the reattachment point toward the base of the model. Martellucci and Agnone used pitot probes to produce pressure and velocity profiles within the wake (17:385-390). However, as stated by Dutton et al., this data acquisition system is considered too intrusive by today's standards (10:3).

In 1994, Burt, Miller and Agrell used a strut mounted from under the model to study axisymmetric wakes in transonic and supersonic flow. Their research concentrated on validating CFD code. A depiction of their design can be seen in Figure 4. The large strut was necessary to pass bleed air into the wake to model an engine plume. They performed laser-doppler anemometry (LDA) tests on the flowfield. They found the support was acceptable for such purposes, although no quantitative results were provided specific to the strut's interference (4:4).

The University of Illinois has accomplished a comprehensive study concerning base flow. J. C. Dutton and multiple co-authors have published dozens of papers on supersonic base flow. Most of their research has used an axisymmetric, Mach 2.5 wind tunnel and a cylindrical model. While this makes comparisons to the 10-degree cone at Mach 2.93 difficult, this research serves as a good benchmark because of its quality and comprehensiveness. Led by Dutton, they have investigated the velocity, pressure and turbulence profiles in the wake (10:4). They also have experimented with the effects of boattailing and base bleed (13, 15). They have used laser-doppler-velocimetry (LDV) to obtain velocity profiles, turbulent intensities, turbulent kinetic energy levels and

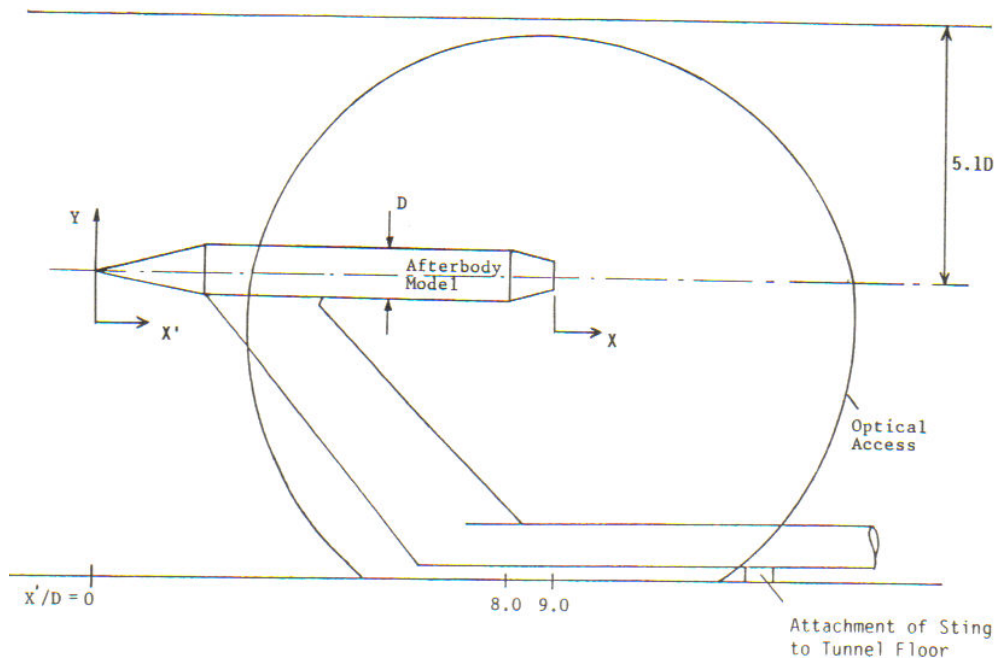


Figure 4: Wind tunnel support used by Burt et al. (reproduced from Reference 4)

Reynolds stresses (12). To compliment the LDV study they used Mie scattering to provide planar images of the structures in the base flow (15). One particularly good source is AIAA Paper 95-0472, which sums up base flow research through 1995. This paper documents all research (not limited to their own) on the subject of supersonic base flow (10).

The University of Illinois team applied and approved upon Configuration B from Martellucci et al. The university had a special annular wind tunnel designed for base flow research. The wind tunnel used a forward rod, which is mounted through the nozzle. Their design differs from Martellucci and Agnone in that it has no rear wires or bands for stabilization; thus, minimizing support interference (12:78). Even with this

design, they found they must take great care in aligning the model in the wind tunnel in order to achieve axisymmetric flow. They use oil droplets to do oil-streak visualization to ensure the model is perfectly aligned in the wind tunnel (12:78). These techniques gave a warning that wind tunnel and support design are critical to achieve true axisymmetric flow.

#### **Section 4 – Research Concerning the Store’s Effects**

##### ***Research that Included a Store.***

There is limited research published concerning two objects in tandem supersonic flow. One of the JPL studies from the 1960s, Reference 9, investigated the drag of a drogue towed behind a supersonic cone. This research used the free-flight concept. Various length and width wires were used to tow the drogue and coefficients of drag for each configuration were computed (9:1335). This research concentrated on drag calculations and had little application to this research. Also a 1975 study by Mishra and Chatterjee looked at the effects of an object behind a 10-degree half-angle cone. They looked at objects the same size as the leading cone or larger. They found that the base pressure rose as the aft object was moved closer to the leading body. When the leading body was the same size as the aft body the effects were much smaller. Unfortunately, the usefulness of this research was limited because the aft object was either the same size as the vehicle or larger. Thus, the aft object created its own shock. This tip shock caused a significant base pressure increase (18:317). The store model used in the present study

was 42% smaller than the vehicle. Therefore, the Mishra and Chatterjee study also had limited applicability.

### ***Research Concerning Base Pressure Profile.***

Unlike research containing a store, there has been much published research conducted concerning base pressure. A thorough understanding in base pressure theory will aide the reader in understanding how a store in the wake changes the vehicle's base pressure. The definition of coefficient of pressure adds insight into understanding base pressure trends:

$$C_p = 2/(\gamma M_\infty^2)(p/p_\infty - 1) \quad (1)$$

where p in this study is the base pressure. Base pressure will be low compared to freestream pressure. The lowest this pressure can be is zero, which provides the absolute minimum:

$$C_{p,\min} = -2/(\gamma M_\infty^2) \quad (2)$$

Equation 2 demonstrates two key concepts concerning base pressure. First base  $C_p$  is heavily influenced by the inverse of the freestream Mach number and second there is a minimum base pressure possible. For this study, using Mach number of 2.93,  $C_{p,\min} = -0.17$  (largest negative) (24:565-566).

In 2001, van Raalte and van Oudheusden developed an analytical model to predict the base pressure. There are multiple other base pressure theories. Some of which can be found in Reference 24. However, the van Raalte and van Oudheusden model was used in this research, because it could explain the store's effect on the vehicle's base pressure. The analytical model is based on the concept that base  $C_p$  is a function of Mach



number, Reynolds number using the length,  $Re_L$ , the thinness ratio,  $L/h$ , and boundary layer conditions. They used a predictor-corrector method to combine all of these parameters.

The predictor analysis is based on the conservation of mass principle in the mixing layer. Essentially not all of the shear layer can enter the wake, thus some is recirculated and creates the base pressure. In order to get a velocity profile in the shear layer, they assumed a laminar boundary layer on the cone and used a Blasius velocity profile to model the mixing layer. This resulted in a prediction of base pressure as a function of just Mach number and specific heat ratio:

$$C_{p,esc} = \frac{2}{\gamma M_\infty^2} \left( \left( 1 + \frac{0.18(\gamma-1)M_1^2}{1+0.32(\gamma-1)M_1^2} \right)^{\frac{-\gamma}{\gamma-1}} - 1 \right) \quad (3)$$

$M_1$  is the Mach number after the expansion in the inviscid outer region. This equation followed the same inverse proportional relation to freestream Mach number as was shown earlier.

The corrector method predicts the base pressure as caused by the expansion of the boundary layer. It assumes that the boundary layer develops into the mixing layer. Any change to the Reynolds number or thinness ratio will affect the boundary layer thickness and thus the amount of expansion required to create the same size mixing layer. These two factors have been modeled relying again on a Blasius solution to produce the relationship:

$$C_{p,B} = A \frac{L/h}{\sqrt{\text{Re}_L}} + B \quad (4)$$

where:

$$A = \frac{14\sqrt{2}}{\gamma M^2 \pi} \sqrt{\frac{1 + \frac{\gamma-1}{2} M_\infty^2}{1 + \frac{\gamma-1}{2} M_1^2}} \frac{M_\infty}{0.015 M_1} \quad (5)$$

$$B = -\frac{2}{\gamma M_\infty^2} \quad (6)$$

From Equation 4 one can see that this  $C_{p,B}$  is inversely proportional to Reynolds number and directly proportional to the thinness ratio. Comparing Equation 6 to Equation 2, one will note that B in equation 6 is the  $C_p$  one would experience in a vacuum. Thus, the first term in Equation 4 corrects this vacuum pressure based off of  $\text{Re}_L$  and thinness ratio. An increase in Reynolds number will make the first term small and cause a decrease in  $C_{p,B}$  (more negative) and an increase in  $L/h$  will make the first term larger and thus make  $C_{p,B}$  bigger (less negative). The two coefficients  $C_{p,esc}$  and  $C_{p,B}$  are averaged to produce a final  $C_p$  that is a function of  $\text{Re}_L$ ,  $L/h$  and Mach (26:1-7).

$$C_p = \frac{C_{p,esc} + C_{p,B}}{2} \quad (7)$$

To compliment this theoretical research, Herrin and Dutton experimentally investigated the base pressure profile of a Mach 2.5 cylindrical body. Using pressure taps they confirmed earlier findings of a near uniform pressure distribution on the base with an average  $C_p$  of  $-0.102$ , which slightly increased toward the edges. These results can be

seen in Figure 5, which includes a case of a boattailed cylinder. If the boattailing increased  $C_p$ , then we could expect a cone should decrease the cylindrical  $C_p$  (10:4-5).

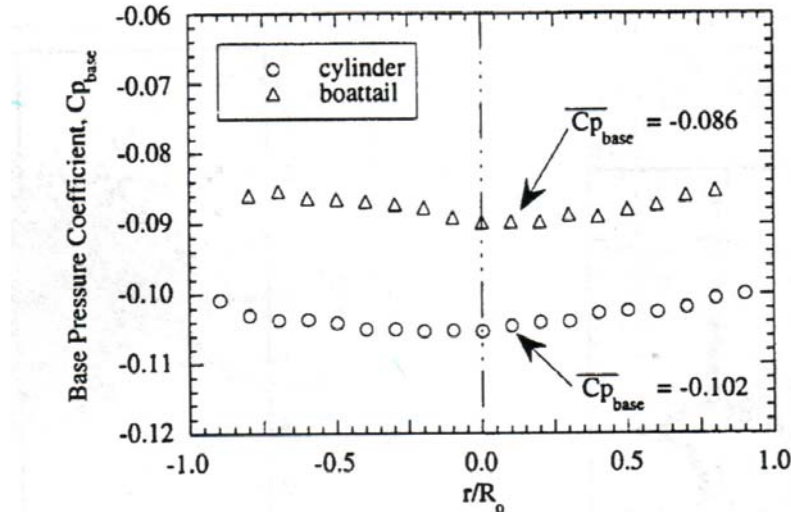


Figure 5: Base  $C_p$  verses radial distance from experimental methods (reproduced from Reference 10)

### ***Wake Research.***

Dutton et al. has extensively looked at the flow characteristics in the wake. Two findings that apply to this research deal with pressure and velocity profiles. They found that the shear layer began recompressing at the distant equivalent to one base diameter down stream. Dutton et al. also developed a velocity profile for the near-wake region that can be seen in Figure 6. The  $S$  on the x-axis denotes the stagnation point at  $x/R = 2.65$  or  $x/D = 1.325$  (10:4-5). These results for a cylinder at Mach 2.5 were compared to our research with a store in the wake. Martelucci and Agnone found the stagnation point to be  $x/D = 0.88$  and the sonic point to be  $x/D = 0.98$  for a 10-degree cone at Mach 6 (17:390).

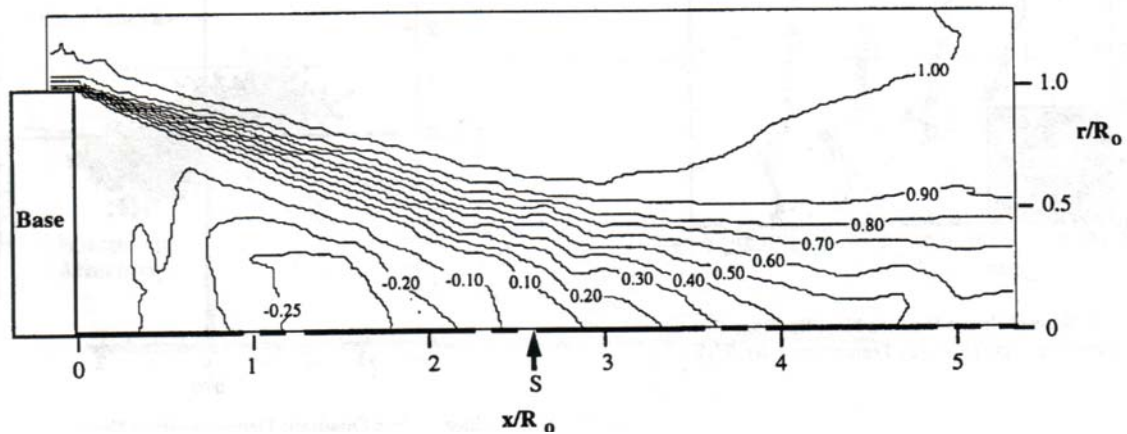


Figure 6: Velocity profile ( $U/U_\infty$ ) in a supersonic wake of a cylinder (reproduced from Reference 10:20)

## Section 5 – Research Concerning the Effects of a Cavity

Molezzi and Dutton investigated cavity effects on a subsonic wake using particle image velocimetry (PIV). Their goal was to explain the drag reductions documented in previous research, which found up to 30% less drag due to an aft cavity. These researchers used a variety of cavities to include cusp-shaped and rectangular-shaped cavities. Notably, they found that the same drag reduction occurred independent of the cavity's depth or shape. Molezzi and Dutton found that the drag reduction was a result of a 10 to 14% increase in base pressure. Their PIV analysis allowed them to conclude that the cavity increased base pressure, and thus reduced drag, by allowing the flow to converge to the centerline faster. They also observed the diffusion of vortices into the cavity, which reduced their strength. The cavity causes a modest 3 to 6% increase in vortex shedding frequency and associated Strouhal number. Although this research was

accomplished on subsonic base flow, it provides insight as to what should be expected in a supersonic base flow with a cavity (19:1-2).

## **Section 6 – Research Concerning Frequency Signals in a Supersonic Wake**

Janssen and Dutton did a comprehensive base-pressure study using transducers. Although their research used a cylinder, their experimental equipment was very similar to the equipment used in this paper and their data acquisition and processing approach was closely followed. Their data acquisition and reduction system consisted of:

- Kulite XCS-062, 10 psi pressure transducers
- 4,000,000 data points sampled at 166,667 Hz
- 50 kHz low-pass filter (20 pole Butterworth)
- Data sets of 8192 were analyzed using Cooley-Tukey fast Fourier transform (FFT), then results were averaged
- Hanning window was applied to suppress side lobes
- 50 % overlap to correct normalized random error caused by Hanning window
- Multiplied power in PSD by frequency “so the area under the curve corresponded to the fluctuating energy at the given frequency (14:607)”

From this research they found the base pressure varied only 0.25% over five circumferential locations and the RMS fluctuations were 5% of the mean base pressure. Their PSD graphs shown in Figure 7 have spikes ranging from 500 to 850 Hz. These low frequency spikes equate to a Strouhal number of 0.092 (14:605-609).

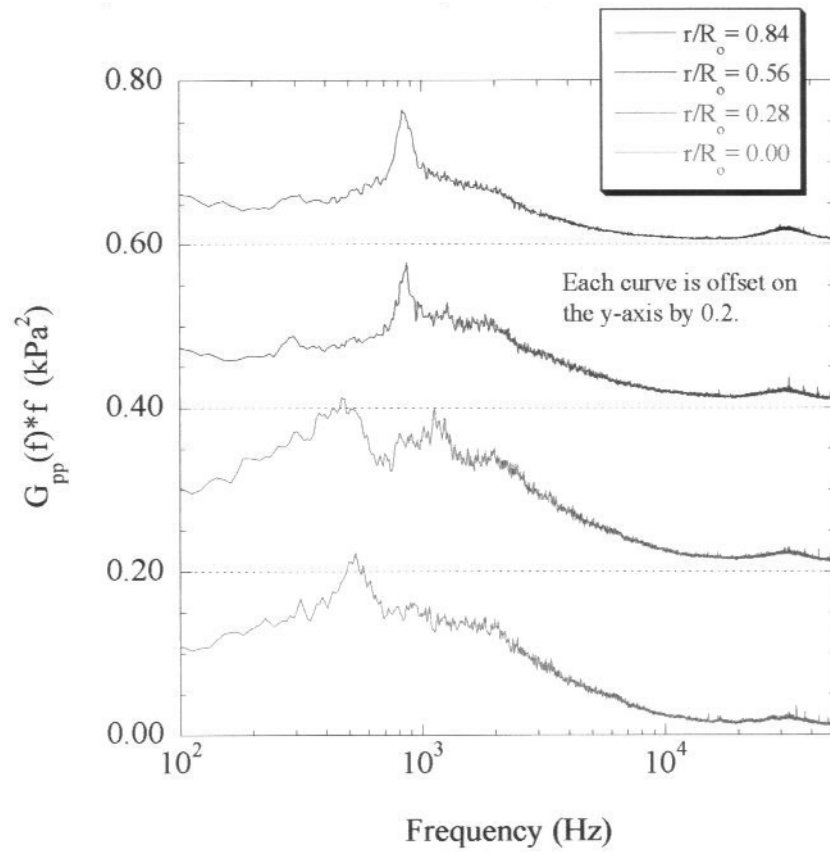


Figure 7: PSD profiles from transducers on the base of a cylinder (reproduced from Reference 14)

### **III. Methodology**

#### **Section 1 - Wind Tunnel System**

The experiments contained in this thesis were conducted in AFIT's supersonic blow-down wind tunnel. Two Ingersoll Rand compressors and electronic driers provided dry high-pressure air at approximately 145 psi. This dry air was stored in a 6000-gallon pressure tank located external to the building. After the tank, a regulator dropped the pressure to 115 psi. The user controlled the pressure sent to the stilling chamber by manually adjusting a reducing valve located near the tunnel. For the purpose of this experiment, the nominal stagnation pressure setting was 38 psi. The air leaving the stilling tank passed through honeycomb flow straighteners and then entered the converging-diverging nozzle. It is significant to this research that the nozzle was 2D, meaning the nozzle was not annular in design. The test section was 2.5 x 2.5 inches with Plexiglas windows on three sides for viewing. These 12-inch long windows extend the entire length of the test section, which was optimum for wake studies. The air leaving the test section then flowed through a variable area diffuser to assist starting and to accommodate various Mach number nozzles. This wind tunnel system terminated with a vacuum tank. Like the pressure tank, the vacuum tank was a 6,000-gallon tank located external to the building. The purpose of the vacuum was to drop the pressure in the test section, which reduced the pressure required to run the wind tunnel. Therefore, the vacuum was turned on prior to the compressed air. This tunnel was capable of running for about 20 seconds before the vacuum pressure became too high. The wind tunnel was

operated at Mach 2.93, based off pressure ratios, and at a freestream static pressure of 1.17 psi. The test section static temperature was 110 degree Kelvin and a Reynolds number of  $3.9 \times 10^8$  per meter was calculated. A picture of the tunnel can be seen in Figure 8.

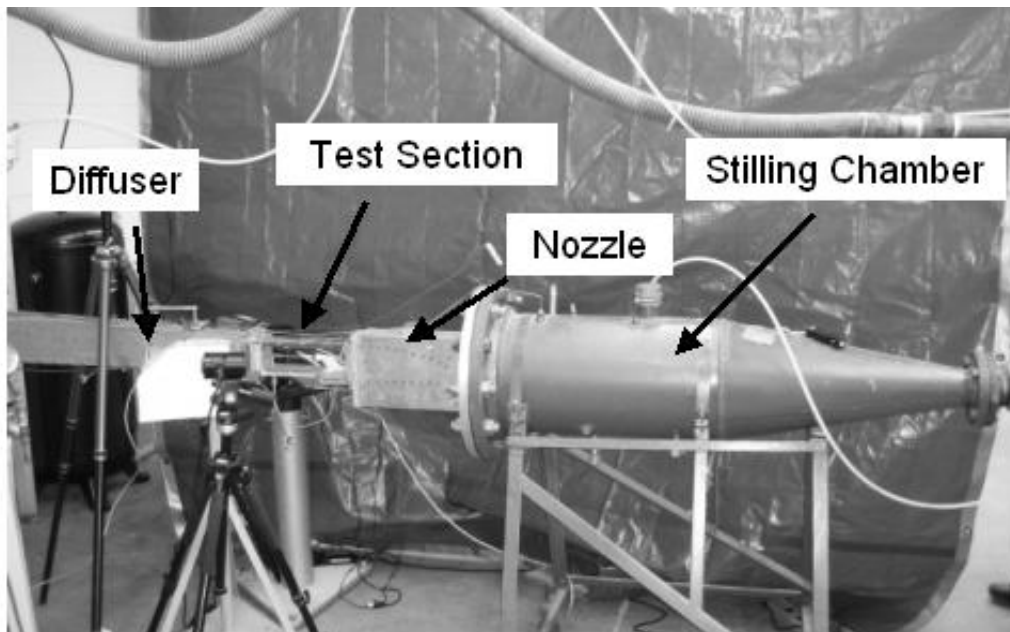


Figure 8: AFIT's supersonic wind tunnel

Three pressure transducers and one thermocouple monitored the wind tunnel system. The three transducers monitored stilling tank, test section and vacuum pressures. The thermocouple monitored the stilling chamber temperature. Information from these sensors was sent to a data acquisition system, which is discussed in Section 4.



## Section 2 - Wind Tunnel Models and Geometry

### *Vehicle Model Description.*

Two types of cones were constructed to simulate the vehicle, one with and one without a cavity. A Stratasys 3D printer created the models from photopolymer resins in 0.010-inch layers. A profile view of the two models used most frequently can be seen in Figure 9. As stated earlier they were 10-degree half-angle cones. Both were 61 mm long and had a 21.75 mm diameter base, which equates to a thinness ratio ( $L/h$ ) of 5.6. The vertex of these cones had a  $\frac{1}{2}$  mm radius spherical tip. The model in Figure 9(a) had a cavity, which was 30 mm long. The walls of the cavity ran parallel to the cone angle. At the base, the cavity had a 14.75 mm diameter opening. The walls of the cavity were approximately 3.5 mm thick. In this paper, this vehicle model with a cavity will be referred to as the *cavity* model. The model in Figure 9(b) was identical to the model in Figure 9(a) minus the cavity. Instead of a cavity it had a 2.5 mm pressure tap. This model was used for PSP tests and to set a baseline to compare to the cavity model's results. This model will be referred to as the *solid* model. The bottom rectangular base or *block* was used for mounting the model in the wind tunnel. This feature will be referred to as a block to avoid confusion with the word *base*, which is reserved for the back of the cone. The block was mounted in a recessed cavity in the wind tunnel and secured by four screws as can be seen in Figure 10. The support or strut, which connected the model to this base, and took the place of a sting, was a diamond 35 mm long and 5.5 mm wide. In Chapter IV, the rationale for these dimensions will be

explained. The diamond was swept back 40 degrees from vertical to reduce the strength of the oblique shock associated with it. This design was inspired by the Martellucci's

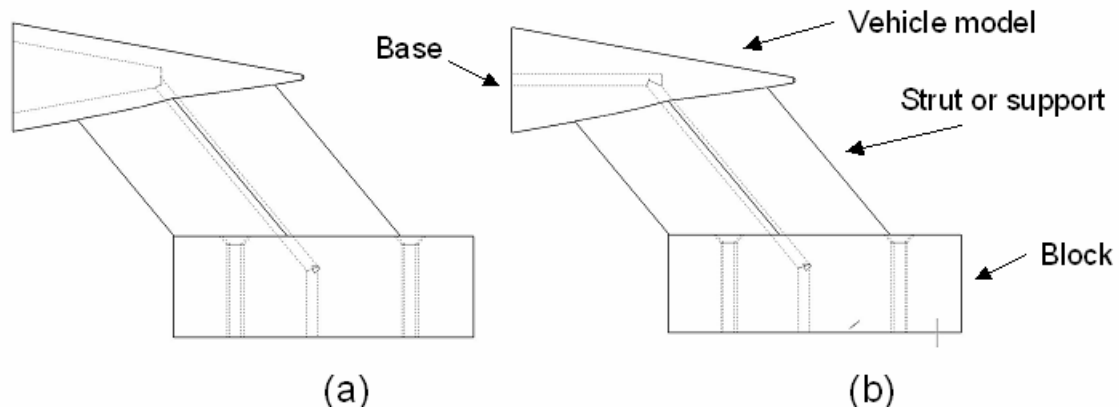


Figure 9: Vehicle wind tunnel models: (a) cavity, (b) solid

Configuration A. The support intersected the cone 5.5 mm back from the tip. This position was a compromise of two factors. First, it was desired to have a conical shock form on the front of the model. Thus, the support could not start at the vertex of the cone. Second, the distance behind the support was to be maximized so the flow could return to conical, axisymmetric flow. Several other designs were experimented with and are discussed in Chapter IV.

#### ***Store Model Description.***

A 10-degree half-angle cone with a  $\frac{1}{2}$  mm-spherical tip was also used to model the store, as can be seen in Figure 11. As stated earlier, the base diameter of the store was 9.21 mm. Thus, the ratio of the diameters of the store to the vehicle was 42%.

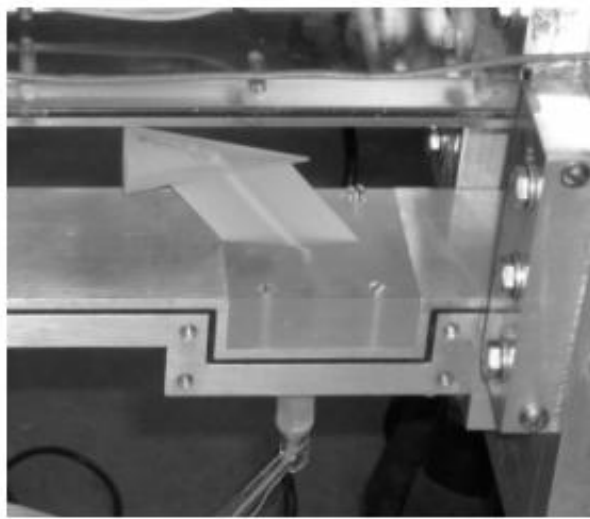


Figure 10: Vehicle model was secured in wind tunnel by inserting square block into cavity in the floor of wind tunnel

The vehicle's cavity's diameter was 14.75, so when the store was fully inserted into the vehicle there was a 2.75 mm gap that separated the store from the vehicle. The conical portion of the store model was 25 mm long. To the rear of this conical section was a 10 mm long cylinder extension. This store model was

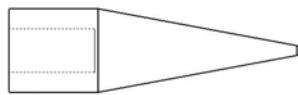


Figure 11: Model of store

affixed to a 3/8-inch diameter threaded rod, which effectively was a sting. The threaded rod allowed manual location of the store at various axial positions in the wind tunnel as can be seen in Figure 12. The store and its support system were

made from stainless steel. Neither the store nor the vehicle model were designed to easily vary angle-of-attack, which was zero for all configurations.



Figure 12: Store model in the tunnel. The store model was mounted on a treaded rod, which allowed easy placement at various axial positions

### ***Non-dimensional Measurements.***

In order to non-dimensionalize the results, all the pressure data was converted from pounds per square inch (psi) to coefficient of pressure ( $C_p$ ). The standard deviation of pressure was non-dimensionalized into a *standard deviation ratio* by dividing the standard deviation by the mean pressure of the associated data file. This allowed easy comparisons to the results of Janssen and Dutton's research in Reference 14. In addition, the axial position of the store behind the vehicle was non-dimensionalized by the

vehicle's base diameter as can be seen in Figure 13. Radial positions were recorded with zero degrees being the top. Looking from behind of the store, radial position was measured with a counter-clockwise rotation.

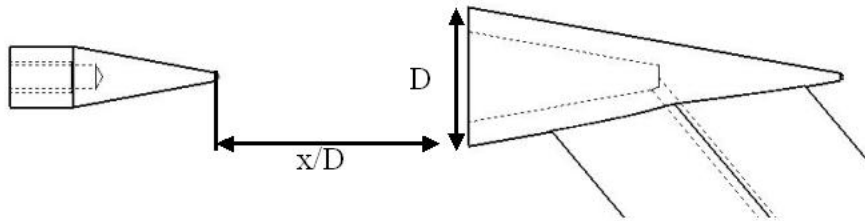


Figure 13: Non-dimensionalizing axial position

### Section 3 - Schlieren Imaging System

A Schlieren system was used to acquire high-speed digital images. The Schlieren mirrors had a 13-inch diameter and a focal length of 80 inches. They were placed 24 feet apart with the test section in the middle. The light source was a continuous wave, high DC voltage, mercury arc lamp with an intensity of 140,000 candles per centimeter. The light source and the knife-edge were offset on opposite sides of the collimated light in a standard z-formation, offset by 11 degrees. The knife-edge was set to a horizontal cut-off for all images. G. S. Settles compiled a great deal of information concerning Schlieren photography in Reference 27, and his procedures for setting up the Schlieren system were used (27: 201-209).

The high-speed Schlieren digital images were acquired using a Dantec IDT X-Stream Vision XS-4 camera. For all the pictures taken using the Schlieren system, the exposure time was set to one microsecond and no binning or filtering was used. This camera was capable of taking images at up to 140,000 frames per second (fps) if the viewing area were minimized to 512 pixels horizontal by 16 pixels vertical (512H x 16V) and 5,100 fps if the view area were at its maximum of 512H x 512V. As one can see, the horizontal width had no impact on camera speed. The number of vertical pixels drove the maximum frame rate because of the scanning pattern of the charged-coupled device (CCD) chip in the camera. Essentially two rates were used in these tests. For most images presented in this thesis, a 20,100 fps (20.1 kfps) rate was used, which equated to 512H x 124V. This allowed the entire height of the test section and eight horizontal inches of the test section to be viewed (some images were cropped to less than eight inches to reduce the memory footprint). The fastest frame rate used was 94,500 fps (94.4 kfps). These images were used for the frequency analysis to be discussed later. For these images the height had to be reduced to 24 pixels, which allowed approximately 11 mm of vertical viewing. The viewing area of these 94.5 kfps pictures was focused from the centerline of the wind tunnel to the top of the cone with no change to the horizontal dimension. Several image formats were used to save the data. Some of these still images were recorded as single frame bitmaps; while others were saved as an average of 100 frames, see Figure 14 for examples. The effect of averaging was the removal of disturbances that were only present for one image. Thus, the averaged pictures appear sharper and make the flow structures, such as shocks and expansions, more prominent,

while minimizing turbulent structures. Averaging had a similar effect as increasing the exposure time. Figure 14(c) shows a 94.5 kfps image. This image is not the same scale as the previous two images in the figure to allow the reader to examine the details of this image. Since it was taken using the same one microsecond exposure, both frame rates, 20.1 and 94.4 kfps, *freeze* the flow for the same time. However, for 20.1 kfps there is a  $4.8 \times 10^{-5}$  second dwell before the next image, but the 94.5 kfps waits only  $9.5 \times 10^{-6}$  seconds before the next image. Therefore, the only difference of the 20.1 kfps and the 94.5 kfps bitmap images is the vertical dimension. The frame rate only is important for the avi files. Typically the avi files used in the frequency analysis were 10,000 frames long although some were as long as 33,000 frames.

### ***Wind Tunnel Imperfections.***

Before any Schlieren images are presented, one needs to examine the imperfections associated with the Schlieren system. Refer to Figure 15 to view an image of an empty wind tunnel at Mach 2.93 (flow is from right to left). There were several Mach waves. Two of these waves originated from the right and were caused by the joints between the stilling chamber and test section. There were also waves that start on the bottom caused by the joints where the rectangular block filled the hole in the floor. There were multiple lines caused by scratches in the Plexiglas and spots from the mirrors and camera. One large horizontal scratch was in the middle of the viewing area. This scratch was in the location of the vehicle's wake and might be confused with a flow structure. Also of interest was the boundary layer that can be observed on the top and bottom. One can observe the boundary layer growth with axial position.

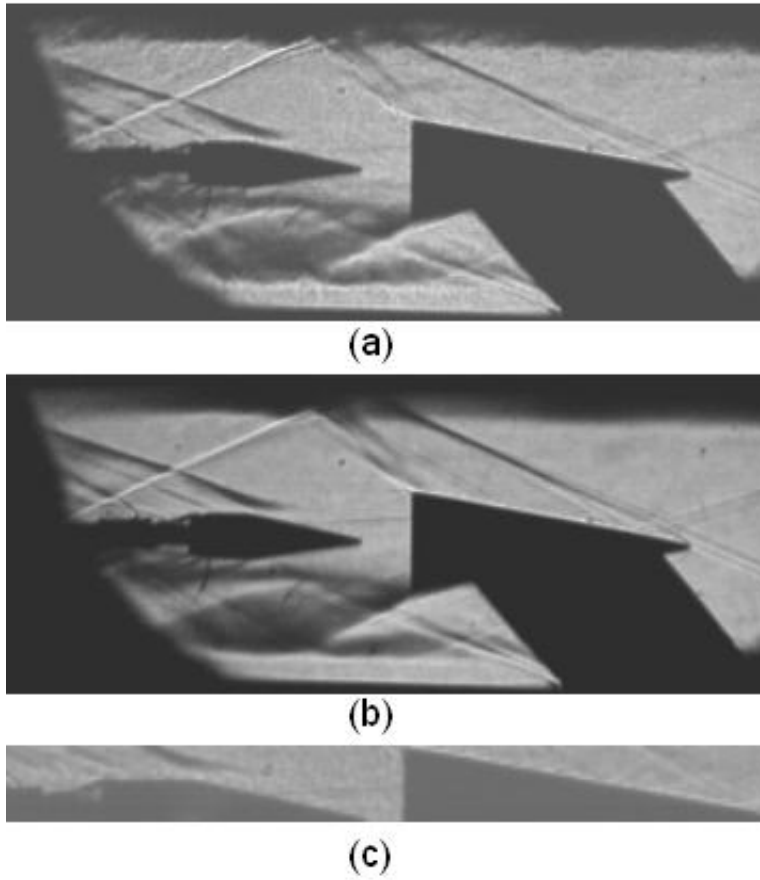


Figure 14: Examples of Schlieren images of store at  $x/D = 0.48$ : (a) 20.1 kfps, not averaged, (b) 20.1 kfps, averaged over 100 frames, (c) 94,500 fps, not averaged

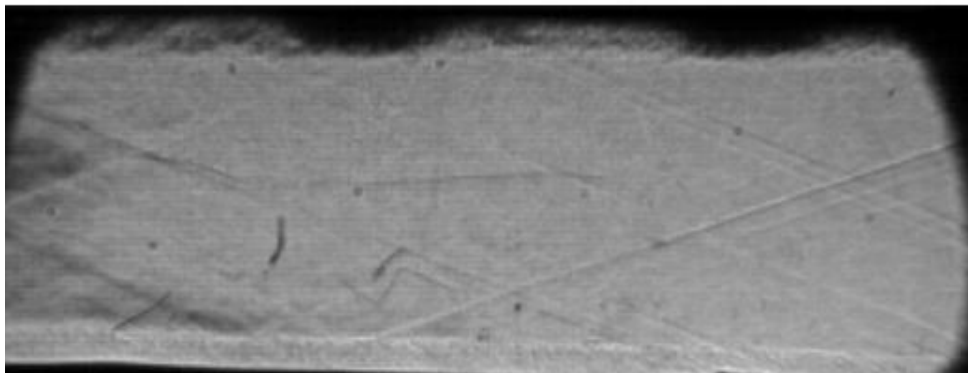


Figure 15: Schlieren image of empty wind tunnel operated at Mach 2.93; flow is from right to left



## **Section 4 - Pressure Transducers and Data Acquisition**

When the vehicle with a cavity and the store were tested together, two high-speed Kulite LQ-062 25 psia pressure transducers were used: one in the lead vehicle and one on the trailing store. Figure 16 shows the Kulites mounted in the models. The transducer mounted in the cavity was placed on the top wall, 5mm back from the base. The Kulite mounted on the store was mounted with epoxy in a recessed slot. According to the manufacturer these transducers have a non-linearity of  $\pm 0.025$  psi (see Appendix A for more information). The output from the transducers was sent to a Vishay Model 2310 Conditioning Amplifier with a 0.02% non-linearity. The amplifier conditioned the signal to  $\pm 10$  volts. This amplifier sent this information to a National Instruments BNC-2120 data acquisition board via BNC cable. Separate boards were used for vehicle and store to reduce cross talk. The boards then sent this data to a National Instruments PXI-6120 card in a PC. The user monitored the signals and recorded data by a Labview computer program.

When the solid cone was used to model the vehicle, an Endevco 8530C-50 transducer was attached to the pressure tap on the bottom of the model. This transducer was certified for up to 50 psia with a manufacturer-rated accuracy of  $\pm 0.05$  psi (see Appendix A). The transducer set-up was capable of only giving mean pressures because the length of the tap made instantaneous pressure readings unreliable. This pressure transducer was connected to an Endevco Model 4428A Pressure Indicator (conditioner) with a 0.1% error. The conditioned signal of  $\pm 5$  volts was sent to the same data acquisition board used by the Kulite mounted in the cavity of the vehicle model.

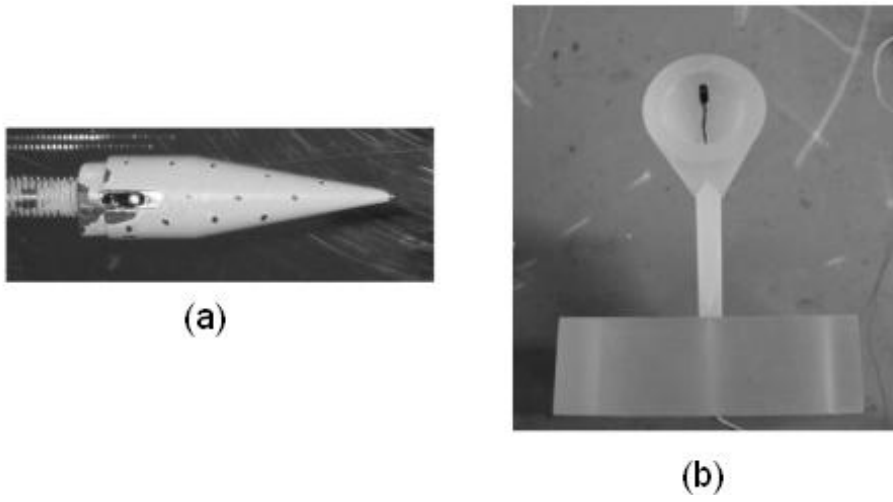


Figure 16: Kulite pressure transducers: (a) in recessed slot in the store, (b) on the top wall of the cavity of the vehicle model

Wind tunnel data, discussed in Section 1, was sent to its own BNC-2120 board. The stilling chamber and test section transducers were sent to individual Endevco Pressure Indicators prior to connecting to the board. This board was connected to a PXI-6070E card in the PC.

Pressure data was taken at a rate of 200 kHz for half a second. Initial tests showed a strong spike at 50 to 60 kHz for the store's Kulite transducer, which was also encountered by Janssen and Dutton who speculated that it was caused by the screen protective cover hitting the diaphragm (14:607). This problem was minimized by using a 9-pole low-pass Butterworth filter.

## Section 5 - Pressure-Sensitive Paint

### *General Pressure-Sensitive Paint Theory.*

PSP operates on the fact that certain molecules in the paint fluoresce inversely proportional to pressure. A light source at a given frequency illuminates the object that has been painted with pressure-sensitive paint. When molecules in the paint absorb photons from the light source they are excited to a higher energy state. They can return to their original state in two ways. First they can give off a photon, usually at a longer wavelength than the light source. This is witnessed as visible light at the fluorescent wavelength. The second way an excited molecule can return to its original state is known as oxygen quenching. If an oxygen molecule collides with the excited molecule, the excess energy is passed to the oxygen molecule by exciting its vibrational mode. This process avoids a photon release and fluorescent emissions. Thus, for most PSP applications, the amount of luminescence is inversely proportional to the oxygen content. Therefore, the lower the luminescence, the higher the oxygen content and pressure (3:159-164).

A diagram of a generic PSP system can be seen in Figure 17. The system consists of a light source, PSP and a detector. The detector in this case is a camera. To discriminate between the light source and fluorescence created by photon emissions, a filter is placed in front of the camera lens. PSP uses a binder, which has two properties. First it must hold the paint together. Second it must allow oxygen molecules to penetrate it so the oxygen can contact the luminescent molecules (5:2).

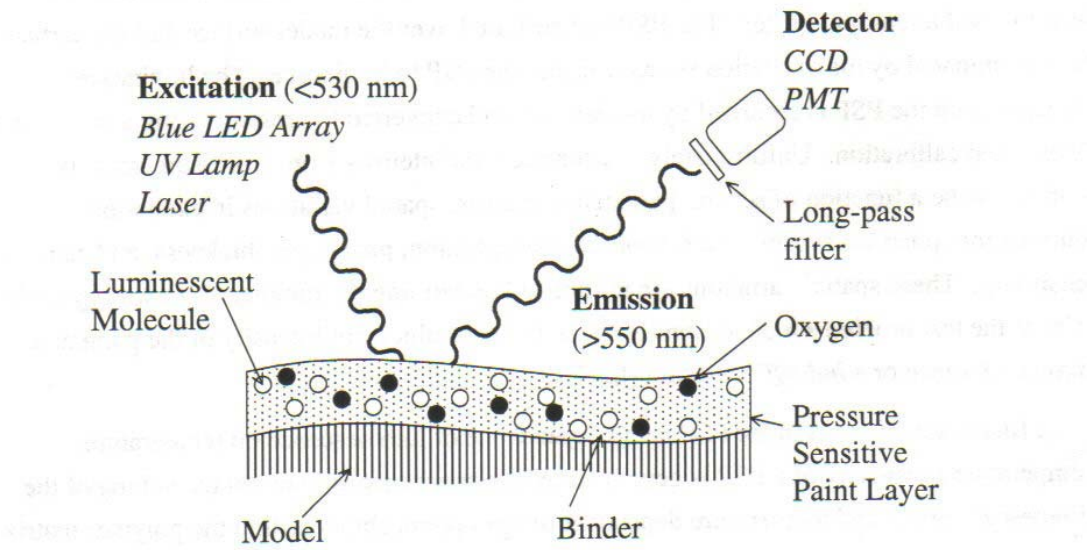


Figure 17: Generic PSP System (reproduced from Reference 5)

### ***Binary/FIB Paint.***

The models used in these experiments were primed and then painted with Innovative Scientific Solutions, Inc. (ISSI) Binary FIB paint. This paint is composed of platinum tetra prophyin (PtTFPP), the pressure-sensitive luminophore or *probe*, flouroacrylic polymer (FIB), the binder, and a reference probe. This reference probe is a secondary illuminating material in the paint and is what makes this paint *binary* because it has a second fluorescing material. This reference material is excited by the same frequency light as the pressure-sensitive molecules. However, it is not sensitive to pressure and it fluoresces at a lower wavelength. The nominal characteristics of ISSI's Binary FIB paint are given by the manufacturer as (21):

- Response time: ~ 0.3 second
- Pressure Sensitivity: ~ 6%/psig at 1 atm

- Photo degradation:  $\sim 1\%/hr$
- Temperature Sensitivity:  $< 0.0075 \text{ psi}/^\circ\text{C}$
- Emission peak: 650 nm
- Excitation spectrum: 380 – 540 nm

***Data Processing--Removing Variations other than Pressure.***

Oxygen content is not the only variable in the system. The intensity can vary due to variations in the paint depth, variations in the light source intensity on the surface due to geometry, variations in the concentration of the luminescent particles and camera sensitivity. These errors cause different areas of similar pressure to fluoresce at different intensities. Taking two measurements can eliminate these variations. First an image is acquired at a known pressure, known as a *wind-off* measurement. Then, an image is acquired in test conditions, known as a *wind-on* measurement. If the only variation is temperature and pressure, then any change in luminescence intensity can only be caused by these changes in flow conditions (3:4).

Binary paint has an additional advantage of two *probes*. This second probe, or illuminating ingredient, can eliminate illumination errors. To use this technique, one needs to take two images for the wind-on case. The first image is taken with a filter that allows only the fluorescence from the signal (pressure-sensitive) probe to pass through to the camera. The second is taken with a filter that will only pass the reference probe. By taking the ratios of these two intensity maps, one can remove any errors due to illumination. The same can be done for the wind-off case. Therefore, a binary paint can almost totally remove illumination errors (5:5).

Temperature variations can be a significant factor. Temperature has two effects. The first is temperature quenching. As temperature increases, the frequency of collisions between molecules increases. Thus, the probability the excited molecule will return to the ground state by colliding with a non-luminescent molecule also increases. Therefore, as temperature increases, less excited molecules will emit photons. Temperature quenching is important because it avoids a photon emission, potentially biasing the pressure reading. The second effect of temperature is that the permeability of the binder increases with temperature. The permeability affects the number of oxygen molecules the pressure-sensitive molecules can contact. Both of these effects can be significant. However, ISSI's binary FIB paint is close to an ideal paint in that its response is nearly independent of temperature. As noted earlier, its temperature variation is less than 0.0075 psi per degree Celsius. A graph of this paint's pressure to fluorescence profile can be seen in figure 18 (5:5).

#### ***Specific PSP Test Procedures.***

PSP was applied to the store model and the solid vehicle model (without a cavity). No PSP images were taken of the vehicle with a cavity. Both models were primed with FIB (FIB is the binder used in ISSI's PSP) to prevent the photopolymer resin used to make the solid model from fluorescing and adding error. Due to the response time of the paint (0.3 seconds), PSP was only used to obtain mean pressures. These mean pressures were compared to transducer data when appropriate to verify PSP readings.

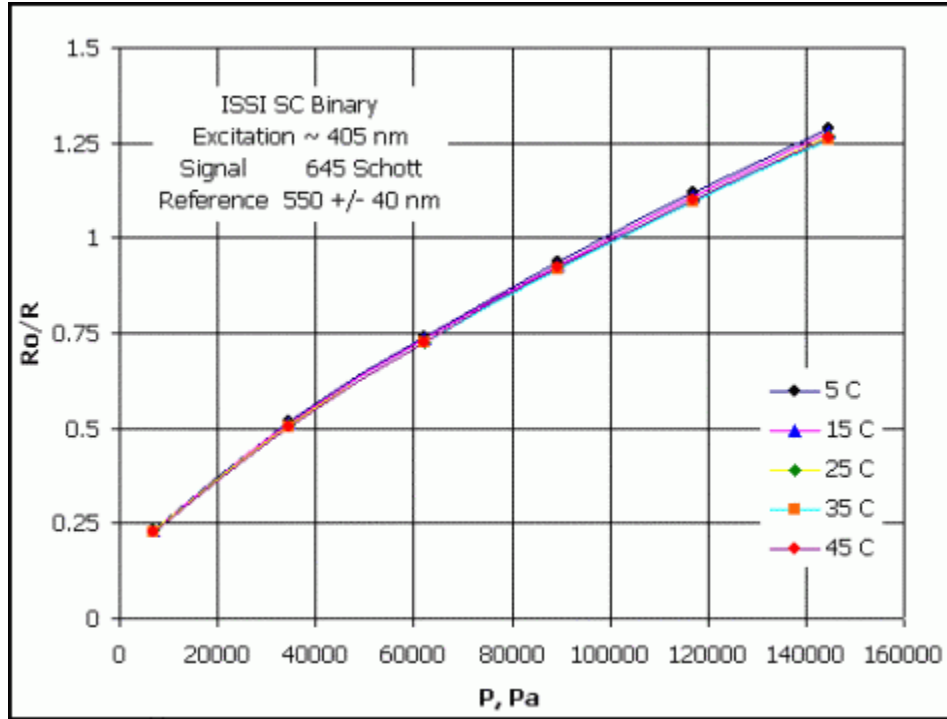


Figure 18: Pressure response for ISSI's Binary FIB paint (reproduced from Reference 20)

One PSP image was taken of the side of the vehicle model and support to assess the effect the strut had on the flow over the conical vehicle model. Other images were taken of the side of the store and the back or base of the solid vehicle model. PSP images were taken at  $x/D = 0.22, 0.92$  and  $2.2$  axial positions. PSP images of the store were taken at the same three distances listed above.

To ensure uniform lighting two ISSI LM2 light sources were used. These 2-inch LED light sources illuminate the paint at 405 nm. As stated earlier, binary paint requires different filters for the reference channel and the pressure channel. In order to switch filters ISSI's filter switch was used. When obtaining reference channel data a 550 +/- 40 nm bandpass filter was used. When obtaining pressure data, a 610 nm Schott glass long-

pass filter was used. Images were acquired on a Cooke PCO 4000 CCD camera with 4008H x 2672V pixel resolution. When taking wind-off measurements, the recorded images were an average of 32 frames, while wind-on images were an average of 8 frames. No filtering or binning was used during acquisition.

Image processing was accomplished on a PC using ISSI Image-Pro software. This software eliminated stray light sources by using background images. These images were taken with all lights off to include the PSP illumination lights. The intensity map from these background images was subtracted from all wind-off and wind-on images.

It is critical when comparing the wind-on and wind-off images, that the exact same point on the model is compared. Although our wind tunnel models were designed to avoid movement and bending, there was some. No movement was visually perceived on the vehicle model. Yet, by comparing wind-on to wind-off images, it was determined that the store model deflected slightly, estimated at 0.1 mm maximum. To resolve the errors induced by movement, *markers* were placed on the models to assist the Pro-Image software in aligning the images. These markers were placed on top of the paint with a permanent pen. The markers show in the PSP images as voids or white spots. After pressure calculations were obtained, a 16 by 16 pixel Gaussian filter was applied to smooth the results.

## **Section 6 – Power Spectrum Density from Schlieren Images**

Schlieren imaging has been known for producing great flow visualization for centuries. However, it is also possible to convert the intensity of Schlieren images into



frequency information. Schlieren imaging is based on the principle of the refractive index,  $n$ , being proportional to density:

$$n - 1 = k\rho \quad (7)$$

The Schlieren concept also relies on the optics principle that the variations in a gas refract light proportional to their gradients:

$$\varepsilon_x = \frac{L}{n_o} \frac{\partial n}{\partial x} \quad (8)$$

where  $\varepsilon_x$  is the deflection angle in the  $x$  direction,  $L$  is the length of the collimated light, and  $n_o$  is the refractive index of surrounding gas. By combining Equation 7 and 8 we obtain an expression for  $\varepsilon_x$  in terms of the density gradient:

$$\varepsilon_x = \frac{Lk}{n_o} \frac{\partial \rho}{\partial x} \quad (9)$$

The physical meaning of the deflection angle is light is bent towards regions of larger density. Thus Schlieren imaging records a density gradient as a variation in light intensity because some light is diverted from its original path by the change in density (27:25-27). If a series of Schlieren images is taken and the intensity at a point is tracked over the series, then one would have a history of the change in the density gradient with time. This time history can be processed with a FFT and converted into a PSD. The end result is a power-versus-frequency plot for that specific point. However, because the values of the constants in Equation 9 are unknown, the magnitude of the power is unitless. The magnitude is based off of the 0 to 256 intensity recorded by the camera.

## IV. Analysis and Results

### Section 1 – Model Design Validation

#### *Rational for Model Support Design.*

All military aircraft to date eject weapons downward from either a pylon or weapon bay, and little is known about how to eject a store from the rear of an aircraft, especially at supersonic speeds. Before we study this flow field, we need to determine *how* to study this flow field. Figure 19 shows four possible ways to support the model.

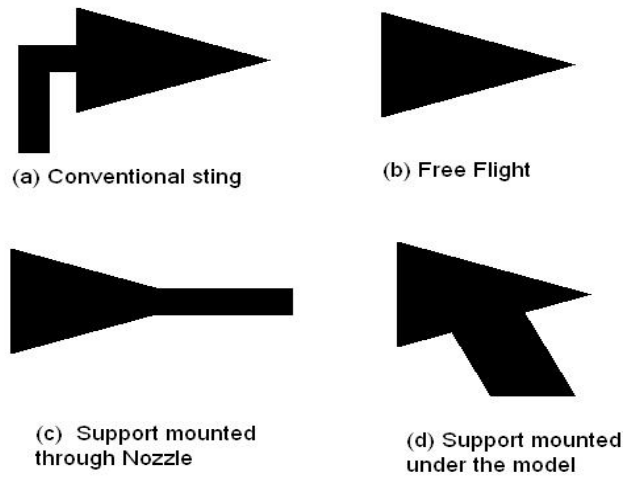


Figure 19: Possible wind tunnel configurations to study base flow

As depicted in Figure 19(a), conventional wind tunnel mounts are usually stings, which attach to the rear of the wind tunnel model. Obviously, this configuration will not work for a study of an aft ejection. The second option, Figure 19(b), is free flight, as

used in the 1960s JPL studies. The obvious advantage of free flight is that the wake can be viewed without any sting interference. However, free flight was not an option for this study because it would prohibit the use of pressure transducers. In addition, it would be very difficult to get two objects (vehicle and store) in free flight in tandem. Therefore, free flight was discarded as an option. Another possibility was to mount the model from the front and have a rod or sting extend through the nozzle and be secured in the subsonic portion of the tunnel, as depicted in Figure 19(c). As stated in Chapter II, Martellucci et al. and Dutton et al. used this design (10 and 17). This forward support presents some application problems. For example, nose bluntness is not easily modeled. Also, the boundary layer will build along the entire length of the rod and model. This can present two problems. First, there may be a separation region at the junction of the rod to the conical model (17:388). Second, the boundary layer will be more developed at the end of the model compared to a model with no forward rod support. The most serious difficulty with this option is the inherent difficulty in applying it to a conventional 2D wind tunnel. As can be seen from Figure 20, AFIT's wind tunnel does not have a symmetric nozzle. Any forward support would have to be curved to follow a streamline of the flow in order not to create shocks. Also, this technique was thought to be impractical for follow-on research in larger wind tunnels because of the length of the nozzles. Therefore, a forward support was not attempted in this study. Rather the option depicted in Figure 19(d), a mount secured underneath the model, was chosen. Clearly, this mount will disturb the flow and influence the base flow behind the model. The goal

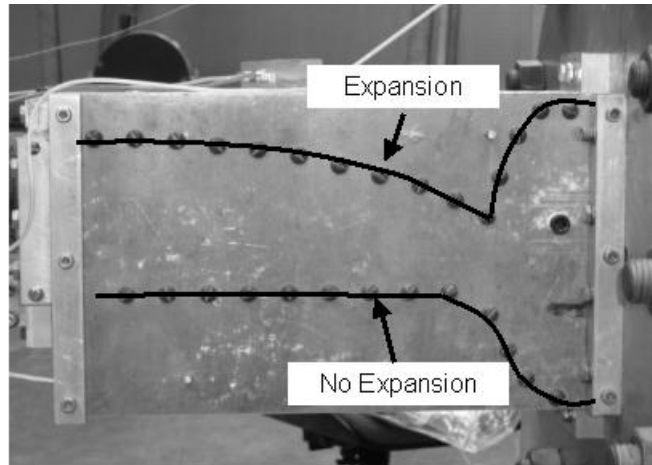


Figure 20: AFIT's wind tunnel nozzle is not symmetric

was to minimize these effects. A symmetric diamond shape was selected for the strut because it returns the flow to near freestream conditions. This geometry had the added benefit of having room to run transducer wires through the center of the diamond. This technique has been used in previous axisymmetric studies. Burt et al. used a similar support to validate CFD code. They verified the flowfield after the strut by LDA measurements and described it as acceptable for wake studies (4:4).

#### ***Vehicle Model Design Validation.***

As stated earlier, a 10-degree half-angle cone was chosen to model the vehicle and a 40-degree swept diamond was chosen as the support. However, other design parameters related to the support were left to the author's judgment. A total of six models with a cavity as well as three solid models were tested in order to solidify these details. A complete set of profile view drawings for these models can be viewed in Appendix C. Schlieren photography was used to assess usefulness of these models.

Initially, two solid and two cavity models were tested. Schlieren images of these models can be seen in Figure 21. S1 and S2 were solid models and C1 and C2 were models with a cavity. All of these early models had a smaller cone: 18 mm diameter versus 21.75 mm diameter for the final design. The supports of models S1, C1 and C2 were only 25 mm long. These small supports were not wide enough to accommodate pressure transducer wires. Small cones and supports characterized these early designs because of concerns of choking the wind tunnel. Once it was confirmed that starting the tunnel was not an obstacle, the larger sized cone and strut enhanced the ease of installing the transducers and increased the fidelity of the Schlieren images. S2 had a larger 35 mm support to assess its usefulness. The results of this size comparison will be discussed later.

Unknown wave structures can be seen in Figure 21 on models S1, S2 and C1, which appear to begin at the bottom of the cones' bases. Model C2 did not have this structure. The design characteristic that made C2 unique was a forward-swept support. Several causes of this unknown structure were theorized. The most obvious cause would be the aft swept base. Second, the structure might be caused by slight misalignment of the cone in the wind tunnel caused by irregularities from errors in the Solidworks designs. This misalignment was assessed to be less than a millimeter front-to-aft. Finally, it was theorized that the structures could be coming from the joints in the floor where the rectangular block fits in the floor.

In order to isolate the cause of the unknown wave structure three new models were constructed. Changes to the models included fixing the alignment error and

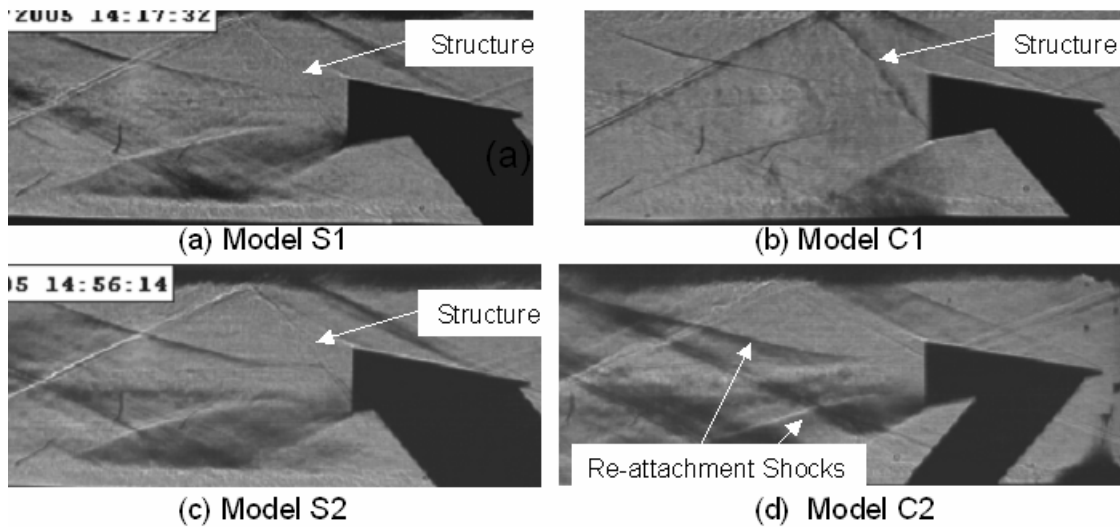


Figure 21: Schlieren images of first-generation vehicle models

increasing the cone's diameter to make it more pronounced compared to the support. The location of the model in the wind tunnel was moved 20 mm to the rear in case the unknown structure was associated with the joints in the floor. Also, the aft swept support was increased in size to 35 mm like S2. Schlieren pictures for these second-generation models can be seen in Figure 22. Ironically, the mysterious structure was now on C4, the forward swept support. C4's cone was at the approximate same distance in the test section as the first generation models with this structure. Therefore, it was concluded that this structure was likely associated with the joints in the floor. Model C6 did not produce any evidence of this structure. This model also had excellent vertical symmetry. The strut had minimum affect on the boundary layer as can be verified by comparing Figure 22 to Figure 15, which is of the empty tunnel. For these reasons C6 was chosen as the final design for the vehicle with a cavity. For similar reasoning and to maintain similarity, S3 was chosen for the solid model of the vehicle.

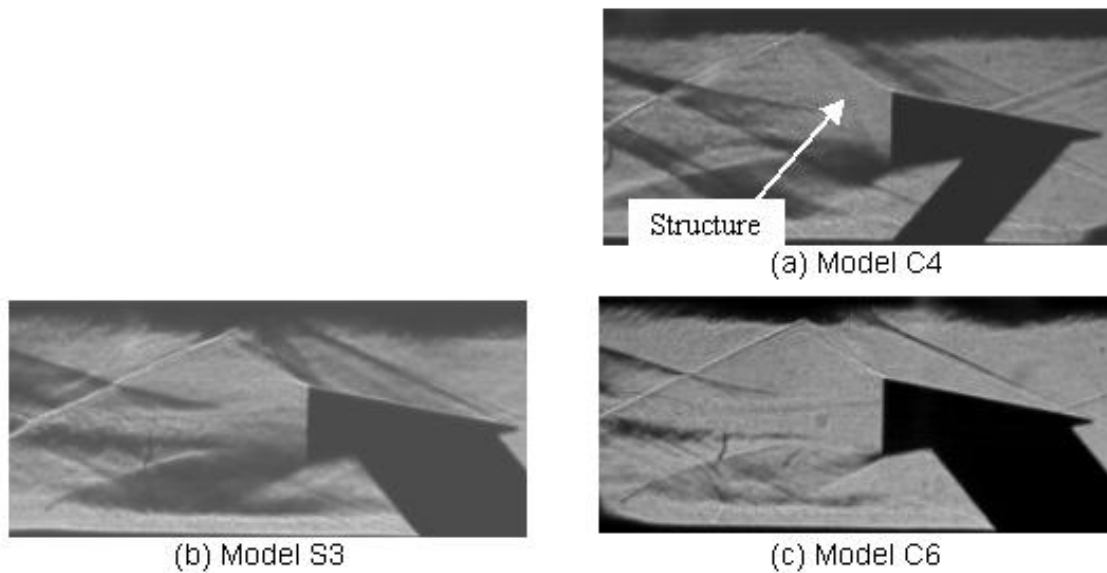


Figure 22: Schlieren images of second-generation vehicle models

There was one last concept that was visually evaluated. As mentioned in Chapter II, Martellucci and Agnone used a mount that secured to the floor of the test section then had a rod extend backwards from it as was seen in Figure 3(a). Based off of this research, a similar model was developed and tested. This model can be seen in Figure 23. The advantage of this design was it maximizes the distance between the support and the base of the cone. This gave the flow maximum time to return to axisymmetric flow before the wake. Thus, one would want to maximize the length of rod before the cone shaped object. Martellucci et al. had 11.5 inches between strut and cone. In our design the length was limited to 35 mm due to the size of the tunnel. Even with this short rod, the reflected shock off of the nose of the model intersected the tunnel's centerline at  $x/D$

= 2, not leaving enough room to do wake studies. Therefore, this design was not used, but the author would recommend it be considered for larger tunnels.

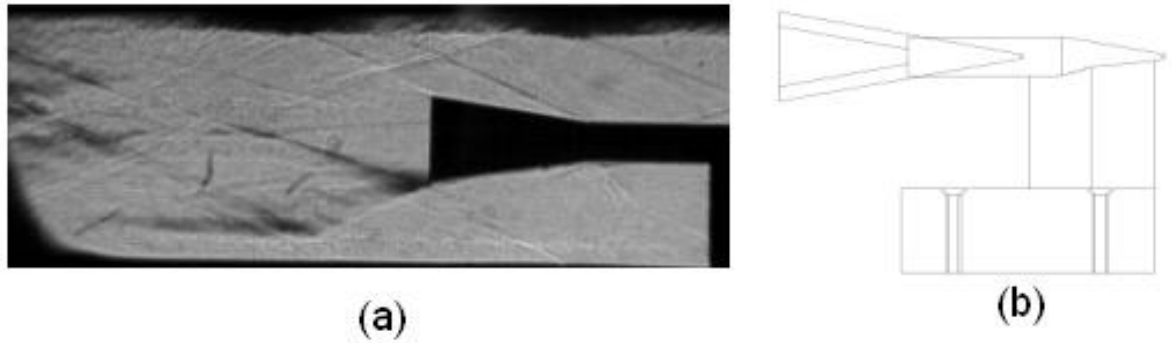


Figure 23: Model with a support similar to Configuration A: (a) Schlieren image, (b) profile view of model design

#### ***Store Model Design Validation.***

The store model was also tested by itself in the wind tunnel. Like the vehicle model, symmetric shock profiles were desirable from an interference standpoint. Also, the strength of the sting needed to be evaluated. A Schlieren image of the store can be seen in Figure 24. No disruptive vibrations were detected and the symmetry was excellent. Movement was assessed to be less than 0.1 mm. No undesirable features were noted and no modifications to the design were made.



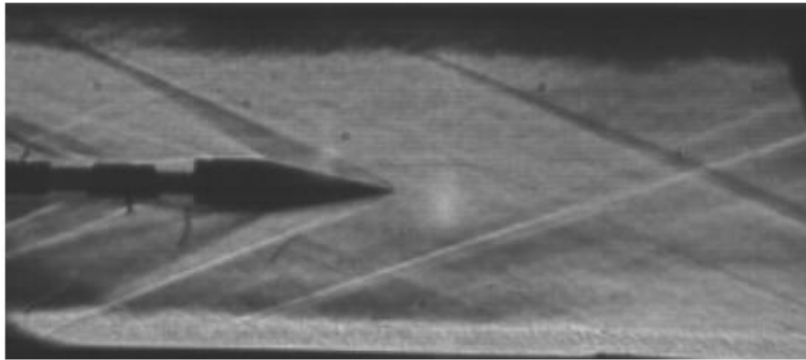


Figure 24: Schlieren image of store model with excellent symmetry

## Section 2 – Evaluation of a Diamond-Shaped Strut

### *Schlieren Image Analysis of the Strut.*

Some insight has already been gained by discussing the design evolution presented earlier. However, a detailed look at additional Schlieren images will add further understanding of the diamond's impact. This analysis used the distance of the reattachment shock as a qualitative tool for evaluating the impact of the strut. As stated in Chapter I, the reattachment point was defined as the point where the reattachment shock starts. In order to obtain an axial position of this point, the images were enlarged 300% and the point where the shock visually began was recorded. Caution must be exercised when comparing these reattachment distances. As stated earlier they are qualitative values. Variations in the Schlieren set-up, such as knife-edge position, may affect these values.

Two solid models are presented in Figure 25. The model in Figure 25(a) has a support with a diamond half-angle of 8 degrees and length of 25 mm. The positions of the reattachment shocks were circled. Their distances were  $x/D = 1.5$  for the top and 1.1 for the bottom (there was a horizontal scratch near the upper reattachment point that may be confused for a shock, refer to Figure 15). The fact that they are not at the same axial location indicates the support's effects. As noted from the JPL reports and Martellucci et al., the support was expected to move the reattachment point closer to the leading body (7:3, 17:388). This is confirmed by noting that the bottom reattachment point in Figure 25(a) is closer. Comparing 1.5 to 1.1 is a 36% decrease, which is larger than the 20% decrease reported by the JPL studies using 0.020-inch wire (8:11). Now compare the reattachment points to those in Figure 25(b). The model in Figure 25(b) is identical to the model in 25(a), except for the support. The support had a 9-degree half-angle and it was increased in scale to a length of 35 mm. Vertical lines have been drawn to allow the reader to compare from image to image. One can see that locations of the top and bottom shocks are nearly identical for both models. This implies that the size of the support has little effect on the wake.

### ***Transducer Data Analysis of the Support***

The pressure transducer on the store was used to collect more information concerning the support's effects. The transducer was rotated to various radial positions to obtain a pressure profile in the wake. If the support had negligible effects, then we would expect no change in pressure with radial position. This rotation was accomplished at various positions behind both solid and cavity vehicle models.

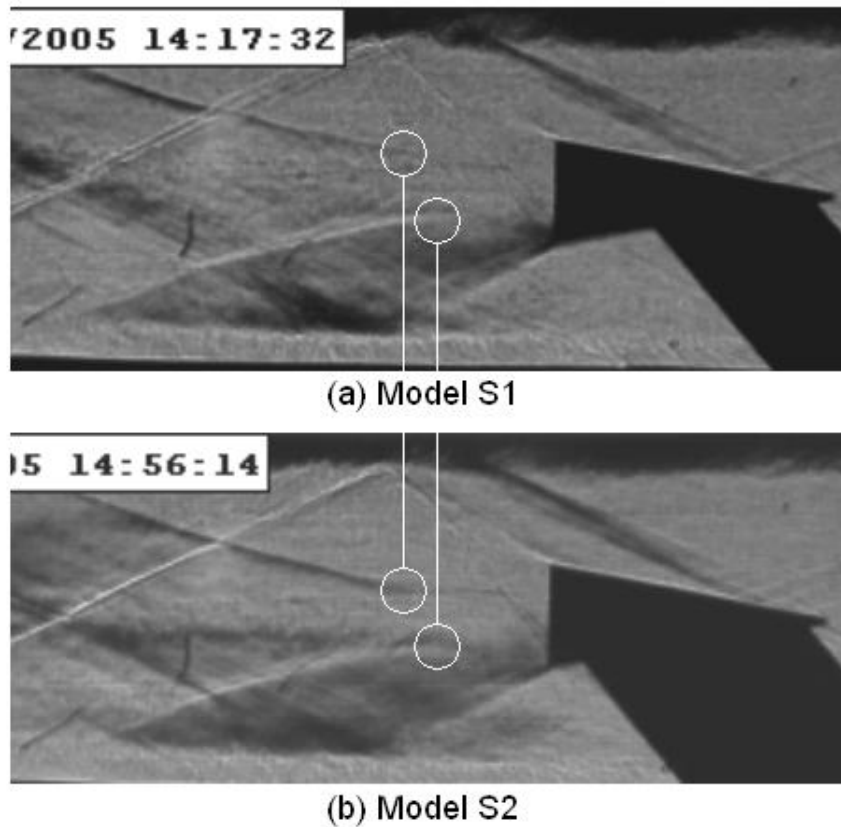


Figure 25: Schlieren images of two identical models except size of diamond strut: (a) 25 mm strut, (b) 35 mm strut

In Figure 26 one can see the results of three rotations performed in the near wake. Schlieren images of these positions can be seen in Figure 27. By examining Figure 26, one will note that all three rotations follow the same trend. For each measurement set, the 180-degree position (the bottom) had a more negative  $C_p$ , thus a lower pressure compared to 0 degrees (the top). This is an indication that the diamond did not recover the flow perfectly to freestream conditions. However, the 90-degree position had an even more negative pressure coefficient. This implies that store alignment could have contributed to the variation in  $C_p$  with circumferential direction, though no alignment

problems were detectable using calipers and a square. Remembering that Dutton et al. and Martellucci et al. used annular wind tunnels (15:1054, 17:386), this variation with angle may be associated with a square or 2D test section. The bottom line is this alignment or wind tunnel design issue resulted in larger differences in  $C_p$  at the 90-degree location than the support interference at the 180-degree location.

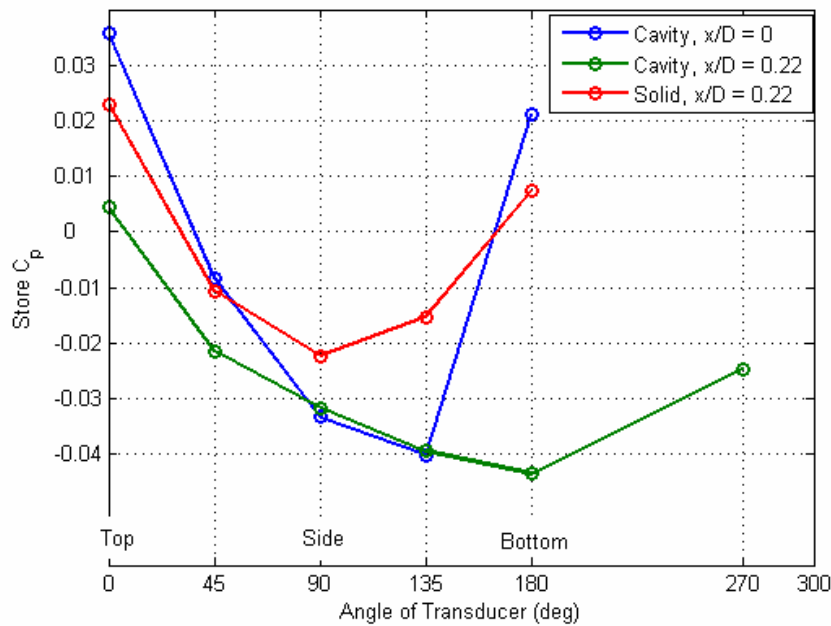


Figure 26:  $C_p$  of store versus angular position of transducer

During the same data runs, the standard deviation of pressure was also calculated. Standard deviation gave an indication of how unsteady the flow was. As one can see in Figure 28, trends observed in the  $C_p$  graph can also be seen in the standard deviation ratio plot. The standard deviation ratio is higher on the bottom than the top. Overall, these

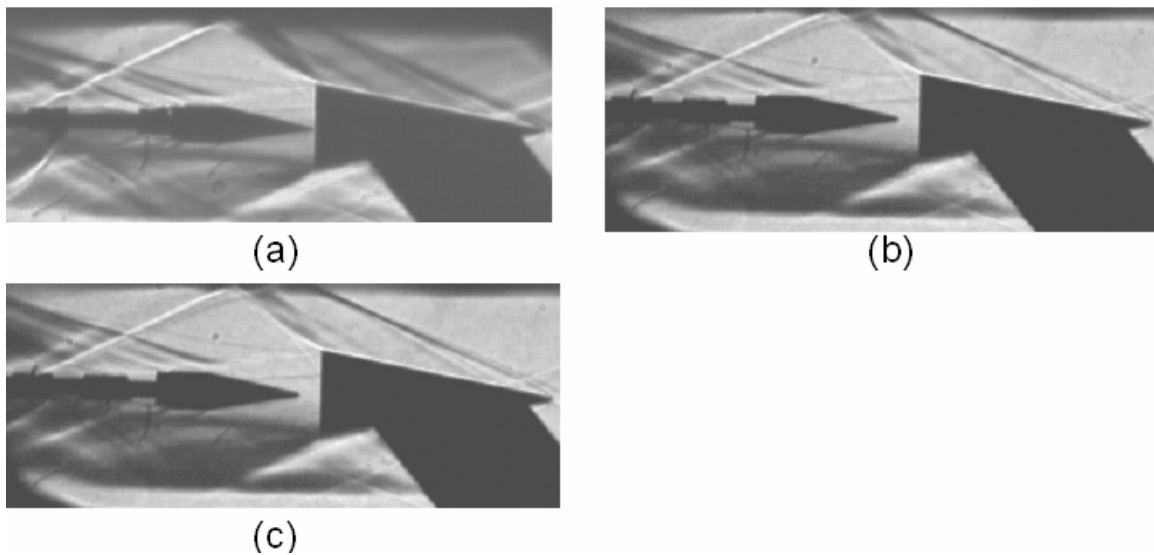


Figure 27: Schlieren images which correspond to the pressure transducer data in Figure 26: (a) cavity at  $x/D = 0$ , (b) cavity at  $x/D = 0.22$ , (c) solid at  $x/D = 0.22$

trends in standard deviation are small compared to the advertised accuracy of the transducer of 0.025 psi. The author was concerned if these were actual flow conditions or just noise of the transducer. Fortunately, there are several cases that added insight to the validity of this data. Transducer data was taken with no flow at all, just the transducer mounted in the tunnel in ambient air. This case provided a 0.004 standard deviation ratio. Then the vacuum was turned on at 0.5 psi, which is close to the run condition of 1.17 psi; again there was no flow, just vacuum. For this case there was a 0.018 standard deviation ratio. Finally the tunnel was run with just a store (no carrier vehicle model), which produced a 0.02 ratio. Lines are drawn on the bottom of Figure 28 to depict the values for these three cases. When the vehicle and strut were present the standard deviation ratio was almost an order of magnitude above these values. Therefore, it was concluded that the trends were not noise nor were they caused by vibrations in the

store's sting. Thus, the high standard deviation ratio of 0.2 seen on the bottom (180 degrees) can be attributed to the strut.

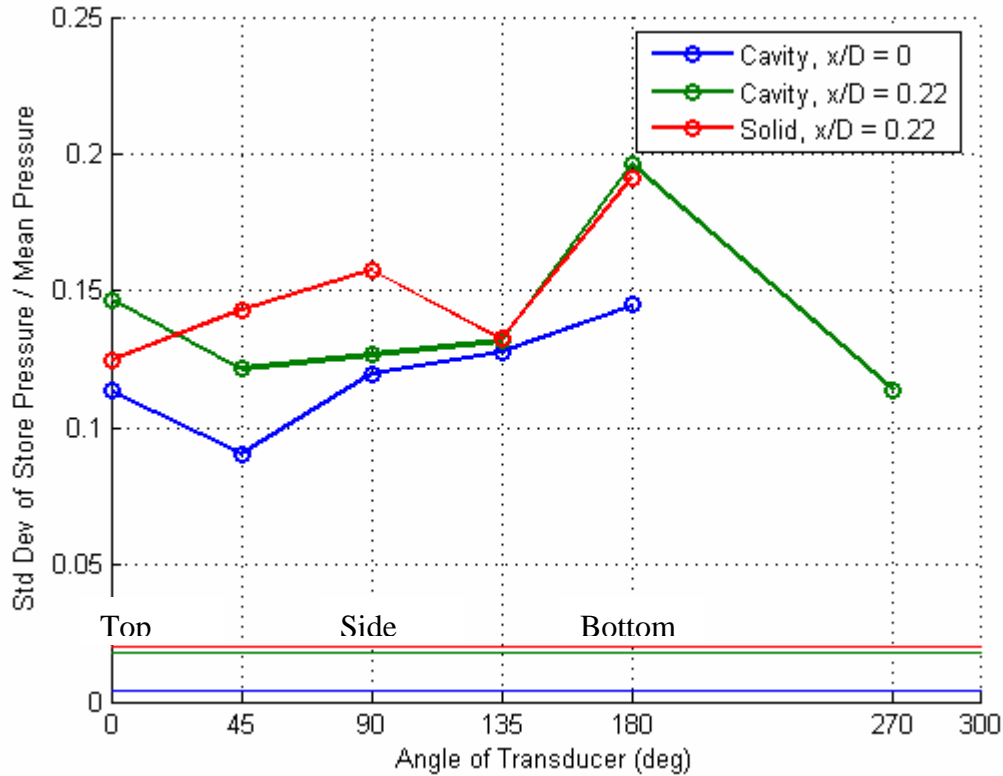


Figure 28: Standard deviation ratio of store pressure verses angular position

### ***PSP Analysis of the Support.***

PSP data runs aided in evaluating the diamond support. PSP images were taken of the side and back of the vehicle as well as the side of the store. A typical side image can be seen in Figure 29. For this image, the store was at  $x/D = 3.0$  to minimize its effects on the vehicle. The white spots on the picture are a result of the markers used to align the image during processing. A few lines are also visible due to the layers from the

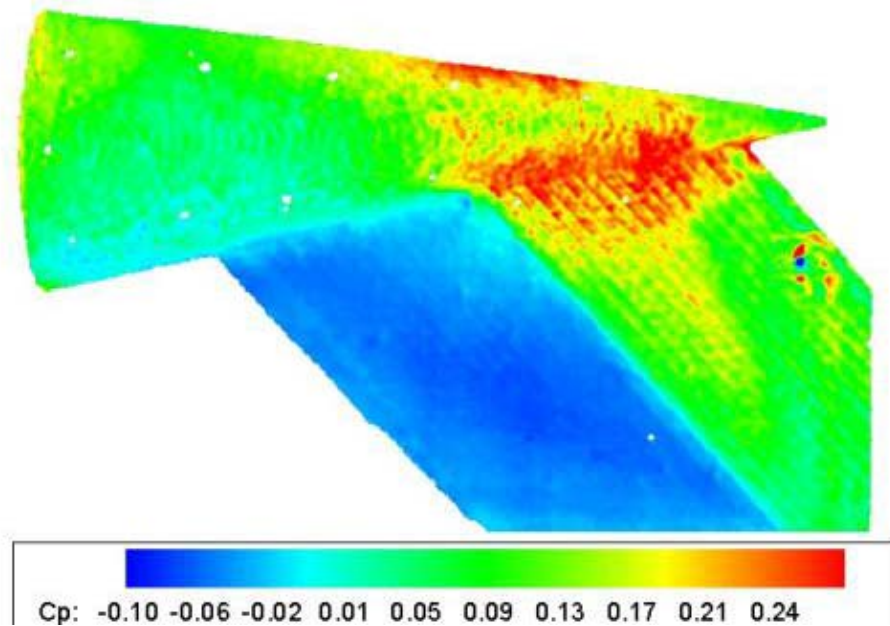


Figure 29: PSP profile view of support and vehicle model

3D printer, which limited the spatial resolution of the measurements. In order to validate the PSP results, a Taylor-MacColl technique was used to obtain the flow properties on the cone's surface. In addition, 2D oblique shock theory was used to determine the flow properties for the diamond support (1:366-371). According to these calculations, the entire cone would have a  $C_p$  of 0.05 and the leading and trailing faces of the diamond would have  $C_p$ 's of 0.11 and  $-0.06$ , respectively. These hand calculations agree very well with the PSP results seen above. These calculations also predicted a conical shock angle of 22 degrees. This explains the red, high-pressure, region on the leading face of the support. This region has gone through the conical shock as well as the oblique shock created by the support. In addition, the sweep in the strut caused the flow to be turned 5

degrees as calculated using procedures from Reference 1, which may have contributed to this disturbance. This high-pressure region created a vertical pressure gradient, which induced flow upwards. This can be seen as red, or high pressure, on the cone's lower surface above the leading face of the support. On the rear of the cone there was a similar pressure gradient, but it was not apparent due to scaling in Figure 29. Figure 30 presents the same PSP data as seen in Figure 29 with different scaling to highlight the pressure gradient on the rear of the cone caused by the strut. From this information one can conclude that the support prevented a uniform pressure distribution on the face of the cone and may induce vertical flow.

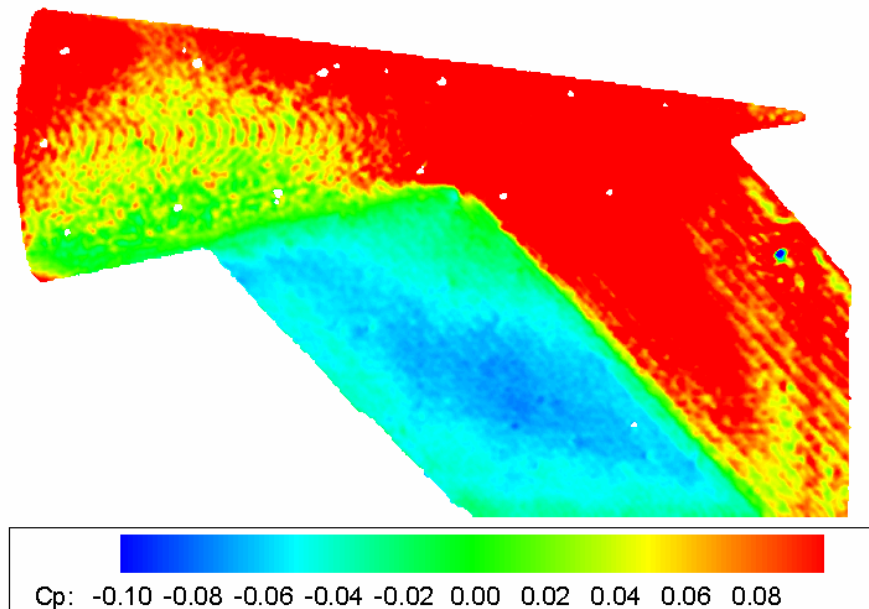


Figure 30: PSP profile view of support and vehicle model with scale changed to highlight the pressure gradient on the rear of the cone caused by the strut



Before one examines the PSP base pressure profiles, one needs to know what is expected on the base. From Dutton et al., they documented a flat pressure distribution on the base with a  $C_p$  of  $-0.102$  for a cylindrical model (10:20). However, using van Raalte and van Oudheusden's approach, one can obtain a theoretical  $C_p$  specific for the cone used here. The only value that needed to be estimated was the turning angle of the expansion fan used to obtain  $M_1$ , the Mach number behind the expansion fan in the inviscid region. This expansion angle was estimated from the Schlieren image seen in Figure 31 to be 20 degrees, which produced  $M_1 = 3.75$ . Assuming  $\gamma = 1.4$ ,  $C_{p,esc}$  was calculated to be  $-0.109$  from Equation 3, and  $C_{p,B}$  was calculated to be  $-0.125$  from Equation 4. Thus, by averaging the two a theoretical base  $C_p$  of  $-0.116$  can be estimated for Mach 2.93 and a 10-degree cone ( $L/h = 5.8$ ,  $Re_L = 2.5 \times 10^6$ ).

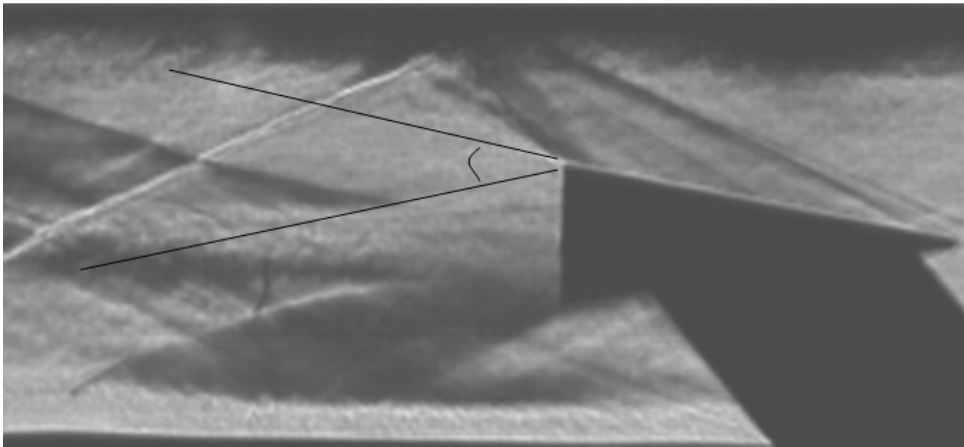


Figure 31: Schlieren image of solid vehicle used to estimate expansion angle

This theoretical base  $C_p$  can be compared to the PSP profile seen in Figure 32. The large hole in the center is the pressure tap. There was more of a left-to-right gradient

than vertical. This corresponds to the trends presented earlier in the transducer analysis. As can be seen in Figure 33, vertical and horizontal crosscuts of the PSP results were compared to Dutton et al. and to the theoretical results computed above. The PSP results contained approximately 500 data points and were smoothed using a Gaussian filter of 30 pixels. Consistent with Dutton et al., the base has a fairly uniform pressure map. Also, the results are in good agreement with the theoretical base pressure value from van Raalte and van Oudheusden.

Although the vehicle's base does not appear affected by the strut, the store was a different story. A PSP profile of the store trailing a solid vehicle at  $x/D = 0.92$  can be seen in Figure 34. The horizontal pressure gradient was expected. However, the large high-pressure region on the top was unexpected because both the Schlieren and pressure transducers indicated the bottom should encounter the reattachment shock first.

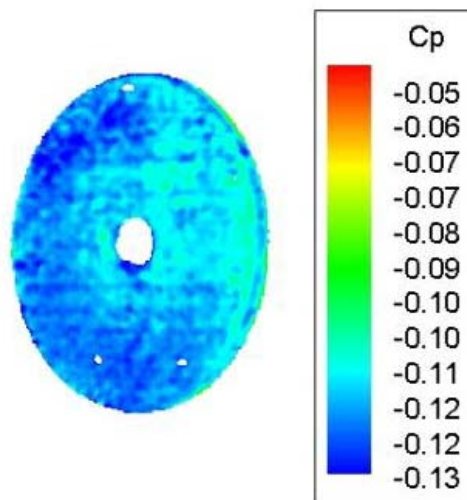


Figure 32: PSP pressure profile of the base of the vehicle with the store at  $x/D = 2.2$

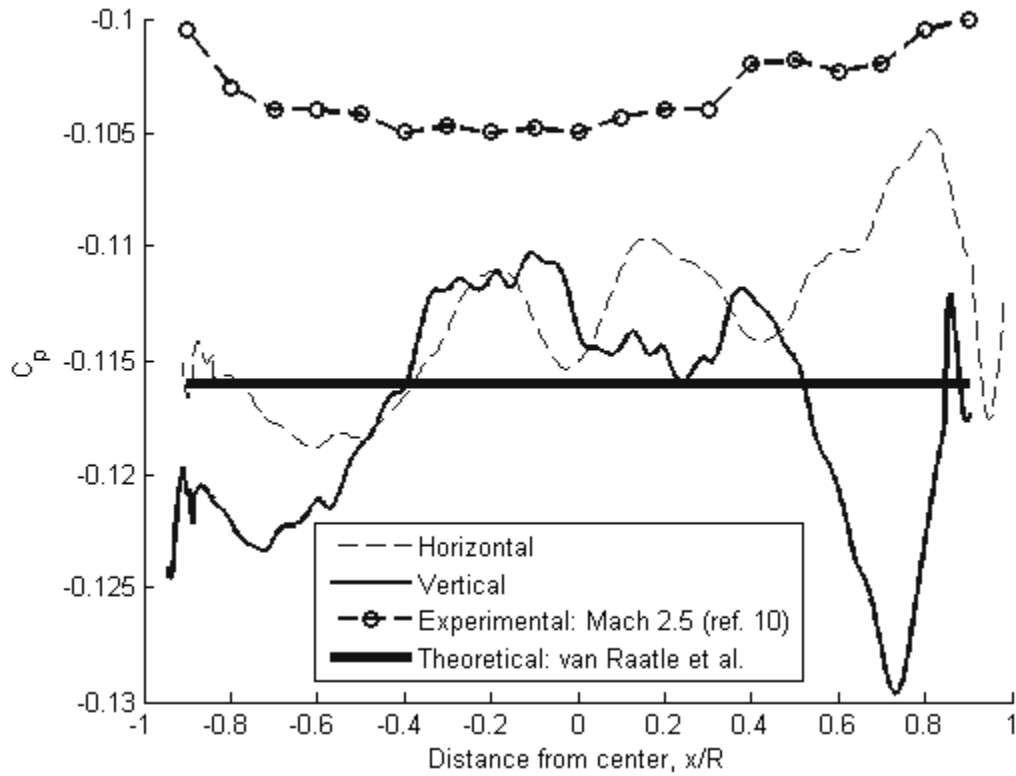


Figure 33: Comparison of PSP base pressure profile to theory and experimental data

However, as can be seen in Figure 34(b) the store was slightly higher than the wind tunnel centerline, thus moving the top of the store into the reattachment shock. Combining these PSP images with the transducer data and the Schlieren images demonstrates the good and bad of the diamond strut. Indeed, the diamond is not perfect; however, with its effects documented comprehensively, the rest of the research could be conducted. The next step was to determine the store's effects.

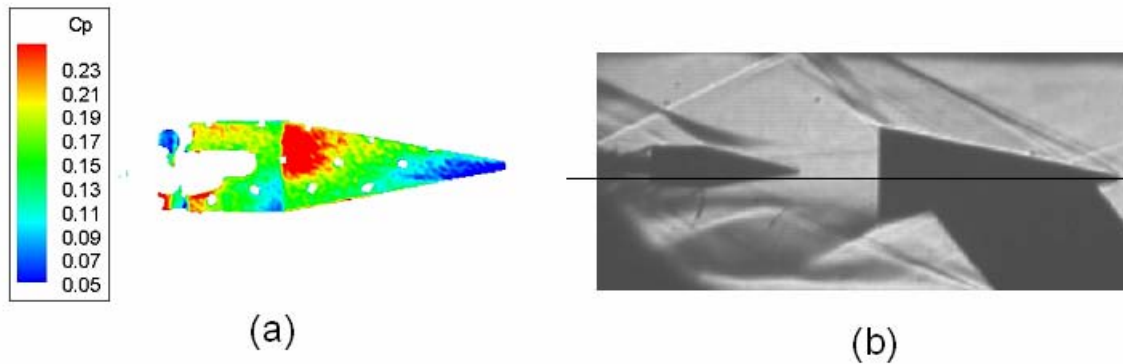


Figure 34: (a) PSP of store at  $x/D = 0.92$  trailing solid vehicle, (b) associated Schlieren image

### Section 3 – Analysis of the Effects of the Store

#### *Schlieren Image Analysis of the Store's Effects.*

The effects of the store were visualized by taking Schlieren images at various positions behind the vehicle. It should be emphasized that the store was static for all tests. Figure 35 contains a series of images of the store at seven positions behind the cavity vehicle model. A similar set of images for the store behind a solid vehicle can be viewed in Figure 36. All the images in Figures 35 and 36 have been averaged over 100 frames. These images were compared to the Schlieren images without the store, Figures 22(b) and (c), respectfully. Every image with the store and the cavity in Figure 35, has a lip shock. In Figure 36, no image with the solid and store has one. The image of the cavity alone does not have one either, as seen in Figure 22(c). The only time the lip shock is present is when the cavity and the store are combined. An open question is whether this lip shock is an effect of the store or the cavity. This will be addressed in Section 4.

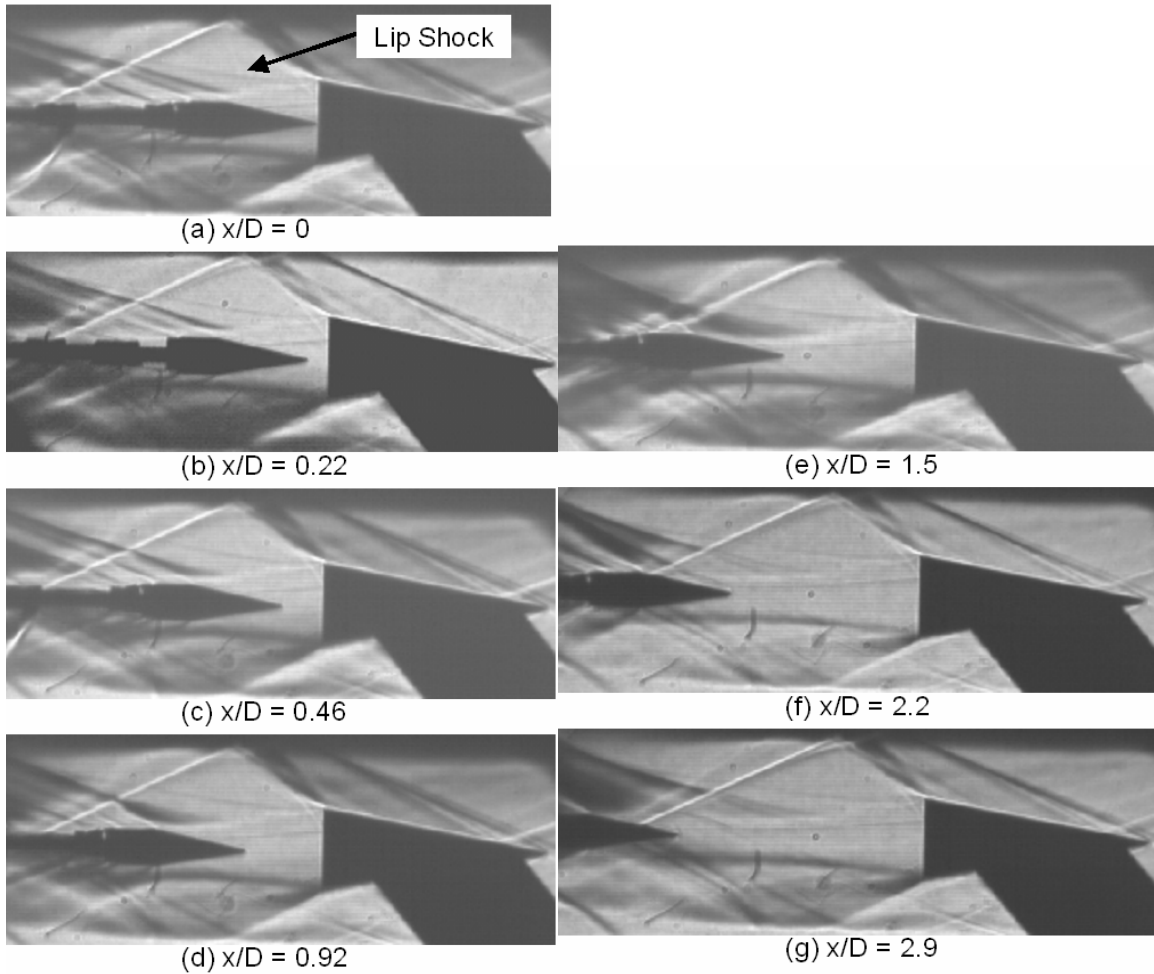


Figure 35: Schlieren images of the store behind the vehicle model with a cavity at various axial positions

The location of the reattachment shock was measured for all of the images in Figures 35 and 36. The  $x$ -location never changed. However, in Figures 35(c) and 36(d), the  $y$ -location was shifted a few millimeters away from the centerline. The effects of this movement will be discussed later. The fact that there was little movement of the trailing shocks implied that the basic shape of the wake stayed the same. Therefore, the store caused very little entrainment. It is theorized if the diameter of the store were bigger, then perhaps the effects would have been more pronounced.

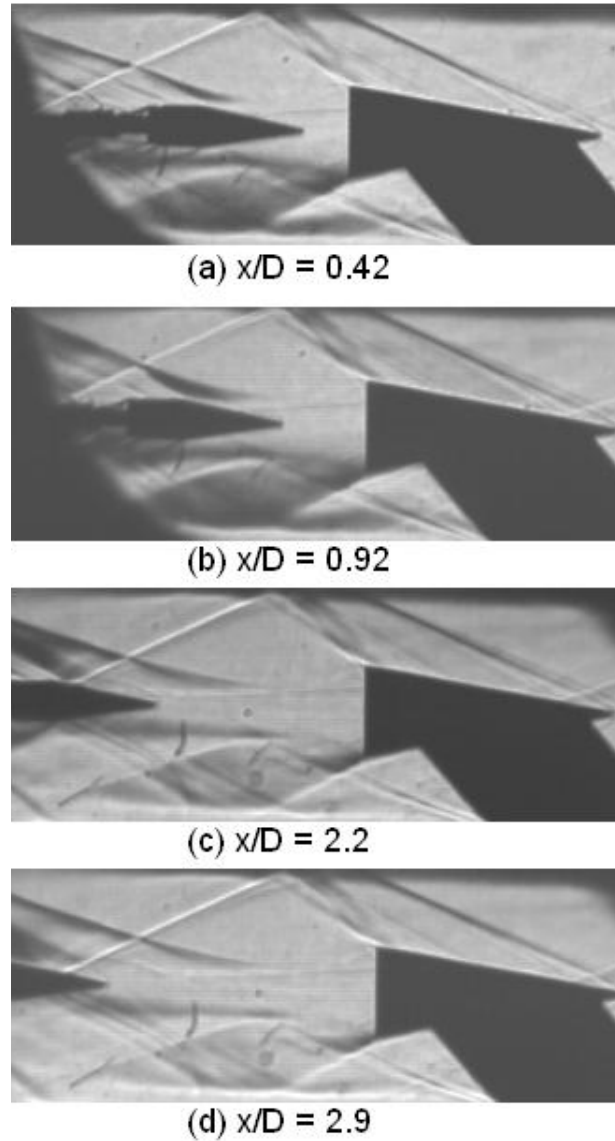


Figure 36: Schlieren images of the store behind the solid vehicle model at various axial positions

One interesting feature is present for both the solid and cavity series of images. At  $x/D = 2.2$  for both of these sets, one can see a bow shock form on the tip of the store. The maximum Mach number that can have a detached shock with a wedge angle of 10 degrees is Mach 1.38 (1:129-150). It can be inferred that the flow returned to supersonic

flow between the last photographed position of  $x/D = 1.5$  and this position of  $x/D = 2.2$ . Taking the average of these two positions, yields a sonic point of  $x/D_{\text{sonic}} = 1.85$ , which can be compared to the research of Dutton et al. (10). Remembering their research was for a cylinder and without a store at Mach 2.5, they observed supersonic flow at  $x/D = 1.75$  as can be seen in Figure 6. The sonic point is critical because in a subsonic region, the store can communicate its presence to the vehicle via pressure waves. This is no longer true in the sonic region (1:87). Therefore, these images imply that after this sonic point, the store will have diminishing impact on the wake in front of it. Another way to explain this concept is to assume the Euler equations apply (requiring no viscous or heat transfer effects). The subsonic solution to the Euler equations is an elliptical solution or a boundary problem, meaning the solution relies on the boundary and points in the region (25:19 and 321). Once the store is out of this region it is no longer part of the solution. Thus, knowing the location of the sonic point is critical to the understanding of the store's influence.

#### ***Pressure Transducer Analysis of the Store's Effect.***

Pressure transducer data was able to enhance our understanding of the store's effect on the flowfield. As discussed above, since the recirculation region is subsonic, the presence of a store will affect the entire region. Based on the Schlieren images, we would expect the store's influence to be greatly decreased after  $x/D_{\text{sonic}} = 1.85$ . Figure 37 presents the vehicle's base  $C_p$  as a function of the store position. Obviously the cavity model does not have a solid base. The cavity's *base*  $C_p$  is really the cavity's pressure

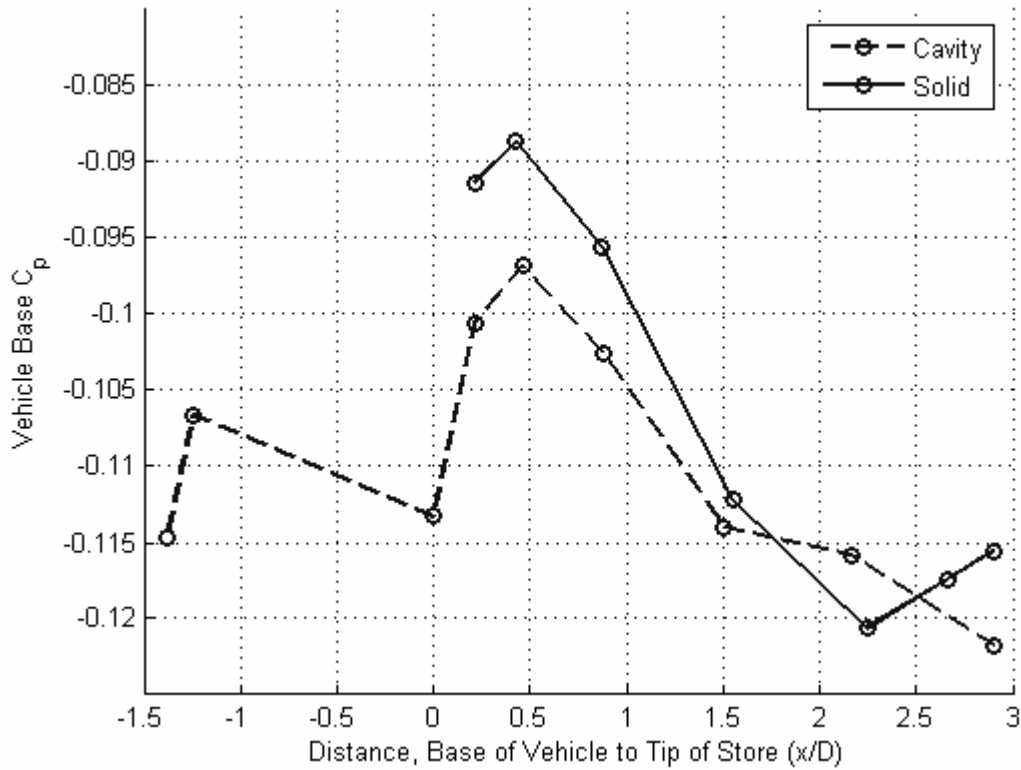


Figure 37: Carrier vehicle base  $C_p$  versus store's distance

as measured by the Kulite pressure transducer, which is 5 mm inside the cavity. One will also note that the x-axis in Figure 37 goes from  $-1.5$  to  $3$ , because for the cavity we were able to insert the store into the vehicle model. The  $C_p$  calculated for these cases was used as a  $C_p$  for the vehicle with a store in the cavity. Thus  $C_p = -0.11$  approximates a  $C_p$  of a vehicle with the store in the weapons bay. However, the store's sting biased these measurements. The far condition,  $x/D = 2$  to  $3$ , can be assumed to be virtually the same as no store. So from Figure 37, it appears the vehicle's base  $C_p$  with no store is around  $-0.115$  for both cavity and solid vehicles. This compares very well with the van Raalte and van Oudheusden's method, which predicted a  $C_p$  of  $-0.116$  (26). Thus when the



store is first released,  $x/D = 0$ , the  $C_p$  will be equal to that of just a cone, or slightly larger. Then as the store moves aft it will cause the base pressure of the vehicle to rise. Once the store is at  $x/D = 0.5$ , its effects will be maximized. At this point the pressure is approximately 20% higher than the pressure without a store. As the store moves farther aft, its influence will continue to decrease until it returns to near the original  $C_p$  at around  $x/D = 2$  which corresponds to the sonic point determined in the Schlieren image analysis.

The theory of van Raalte and van Oudheusden can explain this trend. Refer to Figure 38 to visualize the store's effect. Notional streamlines are drawn from the back of the vehicle to aide in comprehension. These streamlines are not to scale, but are drawn to demonstrate a concept. As the store moves aft it will displace the shear layer outward. Recall, minor movement was observed of the reattachment points upward in the Schlieren analysis. The expansion angle is the angle between the extended cone angle and the streamlines. A line is drawn in the images to represent the extended cone angle. As the store displaces the streamlines outward, the store will cause the expansion to turn through fewer degrees. Since it has expanded less, the pressure will be higher. As the store moves further aft, Figure 38(c), it will be mostly in the far wake and it will no longer displace the streamlines and the expansion fan will return to its original state.

Unlike the mean of the base pressure, there was very little change in the standard deviation ratio of the vehicle's pressure (Figure 39). The standard deviation ratio for the solid vehicle has limited use. As noted earlier, since the pressure transducer for this model was a long pressure tap, this transducer was used for mean pressures only. The

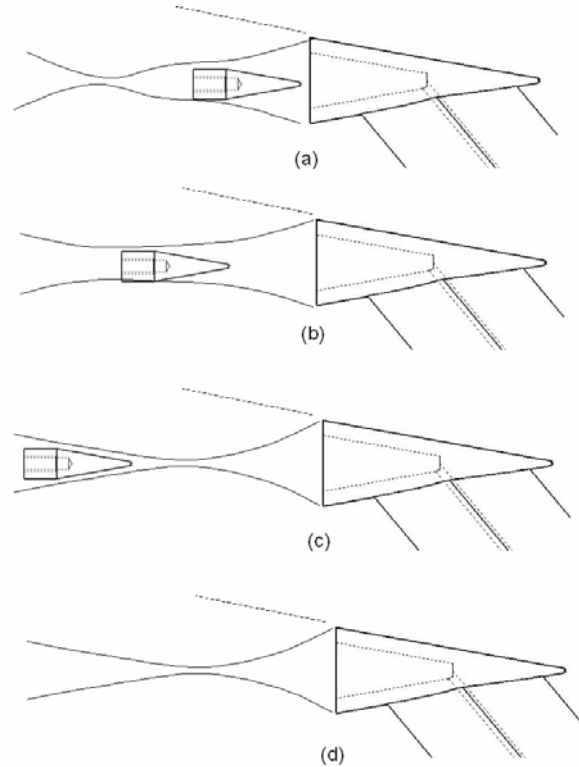


Figure 38: Pictorial representation of the store's apparent affect on the streamlines (streamlines not to scale)

standard deviation should be used with caution and thus is labeled “damped” in Figure 39. The standard deviation ratios for the cavity and solid can be compared to the runs accomplished in still air mentioned earlier. These runs showed the cavity's standard deviation ratio was 0.016 in ambient air and 0.04 in the still vacuum. Clearly this chart is close to the limits that we are capable of measuring. However, this corresponds very well with Janssen and Dutton, who saw a 0.05 standard deviation ratio (14:607). Because relatively little change was observed with variations in the store's position and these ratios compared well to Janssen and Dutton, we concluded that the store had a negligible effect on the standard deviation of the vehicle's base pressure.

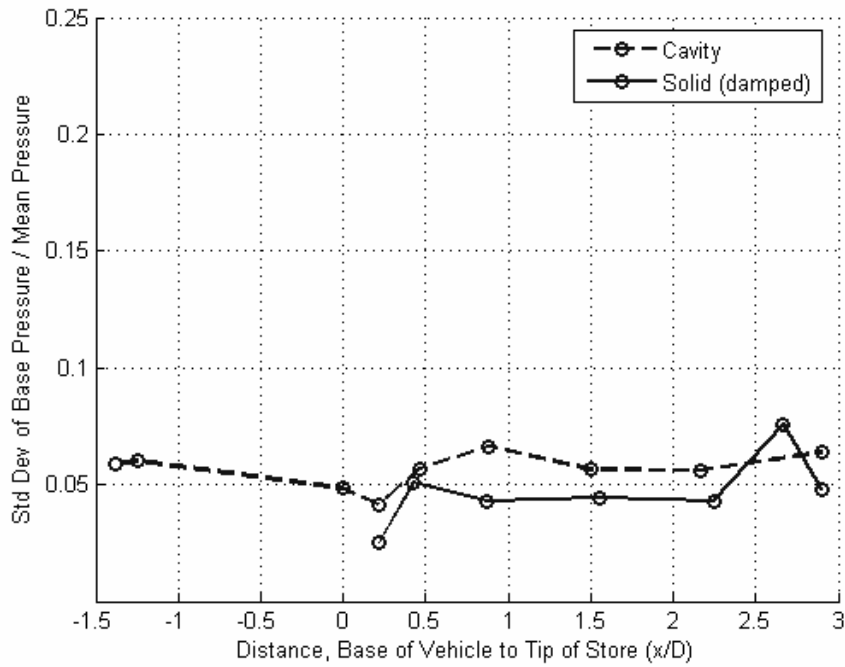


Figure 39: Standard deviation ratio of vehicle base pressure versus distance

### ***PSP Analysis of Store's Effects.***

PSP pressure plots confirmed the transducer analysis and provided additional pressure data on the entire base of the solid vehicle. Three PSP images can be seen in Figure 40 for three different store locations. The triangle-shaped regions in Figure 40(a) are a result of the store in the field of view. As one inspects these images one will note a modest decrease in  $C_p$  as the axial position is increased. Perhaps if there were more images taken at other store positions, the PSP data would have captured the maximum  $C_p$  seen in the transducer data at  $x/D = 0.5$ . However, these limited PSP images do

correspond well with the transducer data taken at these locations. Furthermore they show that the base always had a near uniform pressure distribution.

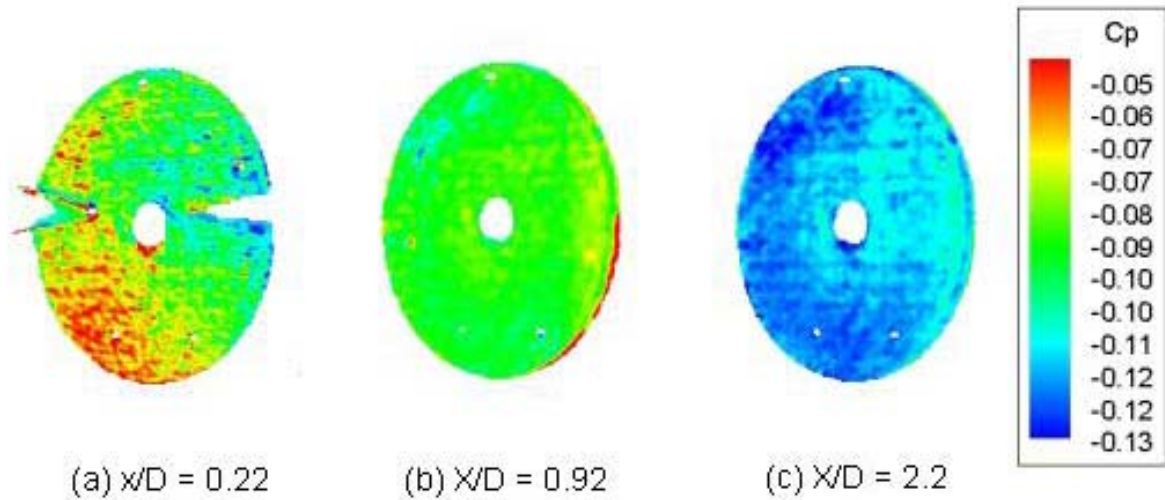
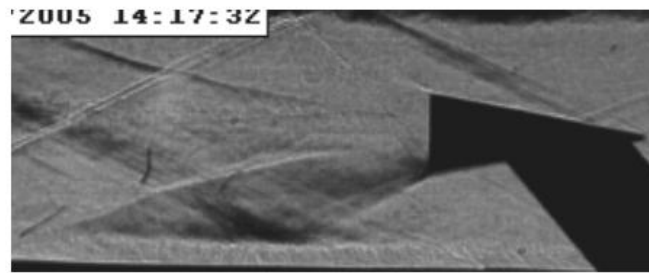


Figure 40: Vehicle base pressure profiles for various store positions (from PSP)

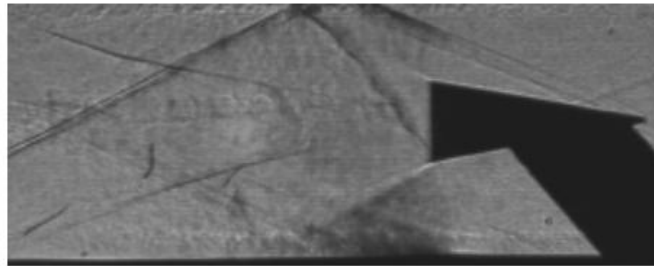
## Section 4 - Analysis of the Effects of a Cavity

### *Schlieren Image Analysis of the Effects of a Cavity.*

In order to understand how a cavity impacted the flowfield, we compared multiple Schlieren pictures. The only variation in these images was the presence of a cavity. The original models S1 and C1 aided us in understanding the significance of a cavity. Figure 41 contains images of these original models. There is no distinguishing feature that separates the two images. A similar comparison was performed using the final models,



(a) Initial Solid Model



(b) Initial Cavity Model

Figure 41: Schlieren images of initial vehicle models: (a) solid, (b) cavity

as can be seen in Figure 42. These images are very similar also. The reattachment shock locations were *slightly* different. For the solid model the shock was at  $x/D = 1.2$  and  $y/D = 0.22$  and for the cavity 1.1 and 0.32 for  $x/D$  and  $y/D$ , respectively. This may mean that the cavity moves the reattachment point closer. This would be consistent with previous research. Molezzi and Dutton also found the reattachment point moved in for a subsonic cavity (19:7). However this small change in reattachment distance was too minor to draw any conclusions. As stated earlier, the reattachment distance from Schlieren images was a qualitative tool. These differences were in the noise level of the technique.

As stated in Section 3, all Schlieren images obtained with a store trailing the vehicle with a cavity had a lip shock. Figure 43 shows two images, one with and one

without a cavity. Besides this feature there were no other changes perceived from image to image. The reattachment distances were the same for both cases.

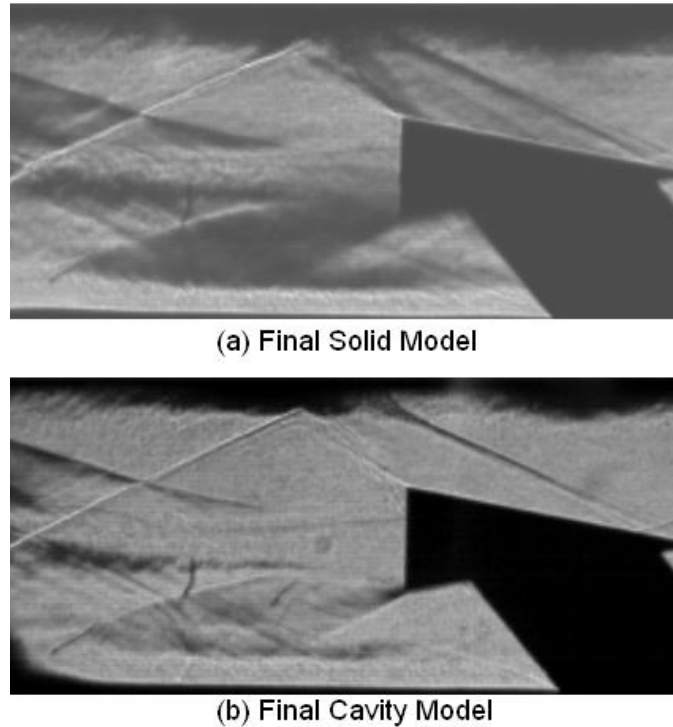


Figure 42: Schlieren images of final vehicle models: (a) solid, (b) cavity

The exact catalyst for the lip shock is not known. Lip shocks are not uncommon in base flows. For example, Martellucci et al. depict a lip shock in their base flow schematic (17:386). It is curious to point out that it is not present when there is no store, yet it is present in Figure 35(g) at the most aft position when the store should have no significant effect on the wake. In addition, the lip shock is not present in any images of a solid vehicle as can be verified in Figure 36. Van Raalte and van Oudheusden mentioned

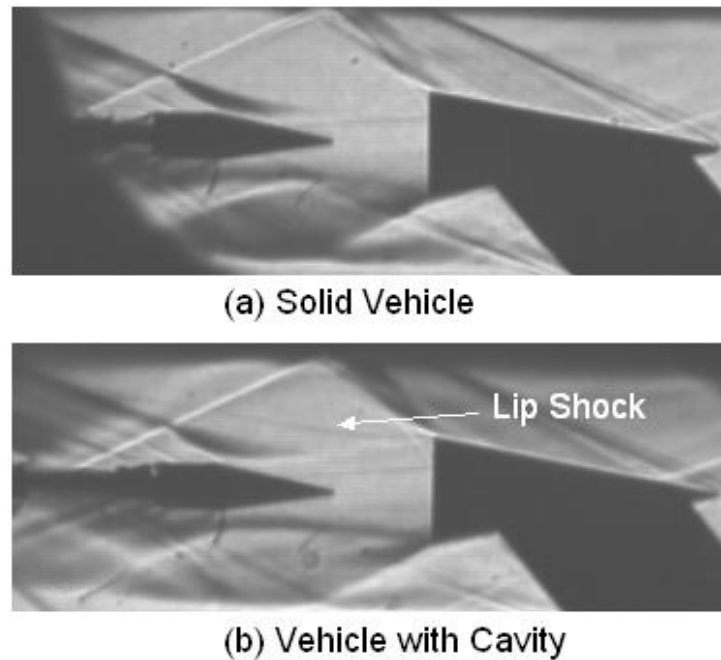


Figure 43: Schlieren images of vehicle models: (a) solid model with no lip shock, (b) cavity model with lip shock

that a lip shock is a way for the flow to correct an over-expansion of the boundary layer (26:1). This theory is supported by the fact that the two vehicle models had different surface roughness. Using the NACA report from Reference 6, it was determined that the transition Reynolds number was  $10^7$  for a 10-degree supersonic cone and we were operating at  $Re = 2.6 \times 10^6$  (6:11). Thus, the boundary layer should have been far away from turbulent transition. However, the Stratasys 3D printer applied resin in 0.010-inch layers to both models, creating a rough surface, but the primer and paint on the solid model smoothed this roughness. Therefore, it is possible the cavity model was tripped into early turbulent flow by the imperfections of the manufacturing process, while the

paint on the solid model kept the flow laminar. The paint could have also rounded the trailing edge and reduced the sharpness enough to change the flow.

On the other hand, the lip shock could have nothing to do with the surface roughness. Francis Hama did a comprehensive study on the cause of lip shocks. He theorized that they are associated with the viscous separation effect (11:1). It is possible that the cavity changed the separation process enough to create the lip shock. In summary, we could not determine the cause of the lip shock. However, all other characteristics of the Schlieren images remained the same with a cavity compared to the solid vehicle model.

#### ***Pressure Transducer Analysis of the Cavity's Effect.***

The pressure transducers were only slightly more successful than the Schlieren system at detecting changes caused by the cavity. Figure 44 presents four graphs together so one can get a global picture of the differences between the cavity and solid vehicle. As can be seen in Figure 44(a), the cavity's pressure was lower (more negative  $C_p$ ) than the solid's for all points except  $x/D = 2.2$ . In light of Mozelli and Dutton who found an aft cavity on a subsonic cylinder increased base pressure by 10 to 14%, this result was unexpected (19:2). Figure 44(c) demonstrates that the vehicle's standard deviation ratio for the cavity was moderately but consistently higher than the solid. However, because of the relative small difference in these standard deviation ratios and because the solid vehicle's pressure transducer used a pressure tap, we are hesitant to draw any conclusions from this data. The cavity's effect on the store was also minimal. Figure 44(b) graphs the  $C_p$  for the store at various axial positions. The plots are virtually



the same until the critical distance of  $x/D = 1.75$ , at which point the reflected shock from the vehicle's tip impinges on the transducer. After this point the pressure data has little relevance. The lack of any change up to this point can be attributed to the fact that the transducer was so far aft on the model that it was nearly in the far wake for all tests. Thus the pressure transducer on the store was not a good indication of the pressure on the forward portion of the store, but more of an indication of how the flow has recovered to freestream conditions. The cavity's most significant effects were on the standard deviation ratio of the store as seen in Figure 44(d). The cavity had a higher standard deviation ratio for all but one case, ranging from 20 to 100% larger than the solid vehicle. The standard deviation ratio reached a maximum at  $x/D = 0.92$ , where the standard deviation ratio was 0.2 for the cavity, which was double the ratio for the solid cone. It is also significant to note that the general shape of this curve followed a similar parabolic profile as the vehicle's base pressure in Figure 44(a).

#### ***PSP Analysis of the Cavity's Effect.***

PSP data for the store was obtained with the store at various axial positions behind both the cavity and solid vehicle. These images can be seen in Figure 45. Each row corresponds to one axial position. The left column contains images of the store following a solid vehicle. The right column contains images of the store following a vehicle with a cavity. Each image has its own scale as seen to the left of each image. Although this makes comparison a little harder, this was necessary to allow the reader to see details in all pictures. The large white spot on the rear of the model is where the pressure transducer was mounted. Also, note that these results were compared to

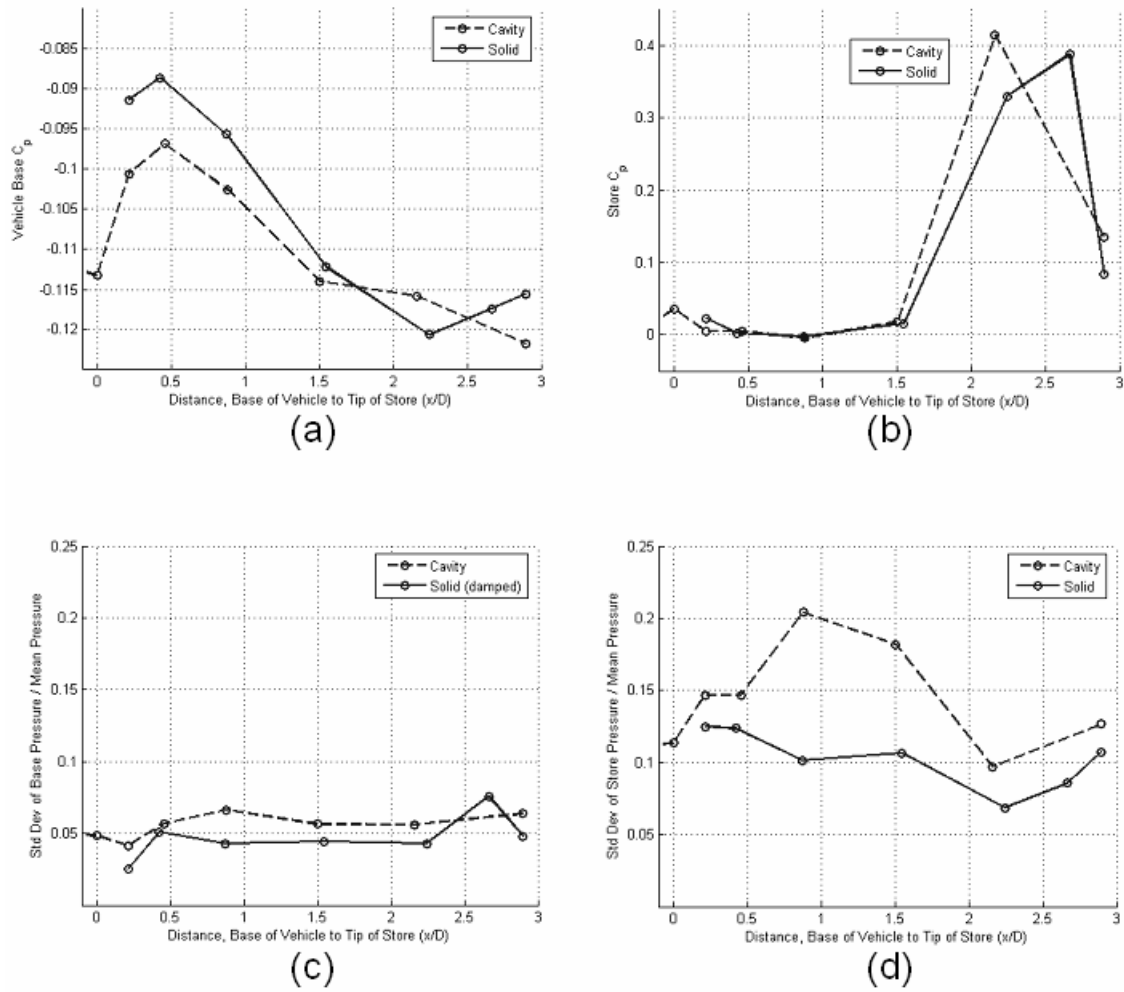


Figure 44: Cavity versus solid vehicle model: (a) base pressure, (b) store pressure, (c) vehicle base pressure standard deviation ratio, (d) store pressure standard deviation ratio

pressure transducer data in order to validate the PSP pressure readings. The transducer pressure readings can be seen above the image when available. The profiles of the solid and cavity models are quite similar. The most significant difference is that the pressures tended to be lower for the store trailing the cavity model.

If the cavity moved the reattachment point closer as observed in the Schlieren analysis, then the store behind the cavity should have experienced the adverse pressure gradient earlier. Arrows have been placed at  $x/D = 1$  on the top four images of Figure 45 to indicate where Dutton et al. found the adverse pressure gradient to begin (10:4). The vertical direction is not symmetrical for all images. For example, on the top of Figure 45(a), one can see evidence of the reattachment shock and adverse pressure gradient as a red area for the solid models. As stated earlier, this is believed to be from the store model being mounted slight above centerline. Similar pressure profiles can be seen in Figures 45(c) and 45(d), which are for  $x/D = 0.92$ . As for Figures 45(e) and 45(f), which are for  $x/D = 2.2$ , the store was behind the reattachment shock and one can see the reflected shocks impinging on the top and bottom of both images.

In order to investigate these PSP results in more detail, examine Figure 46. These graphs are traces of the pressure along the store obtained from the PSP images in Figure 45. Figure 45(a) contains a line depicting the path used to produce these plots. Figure 46 brings another fact to light. In both graphs in Figure 46, the cavity vehicle not only had lower pressure, but it also had a lower pressure gradient. This implies that the cavity model's wake had a weaker adverse pressure gradient.

In short, overall the cavity had modest effects. The combination of the PSP, pressure transducers and Schlieren images showed little changes. The most significant changes caused by the cavity were the lip shock and the slight decrease in pressure and pressure gradient revealed in the PSP analysis.

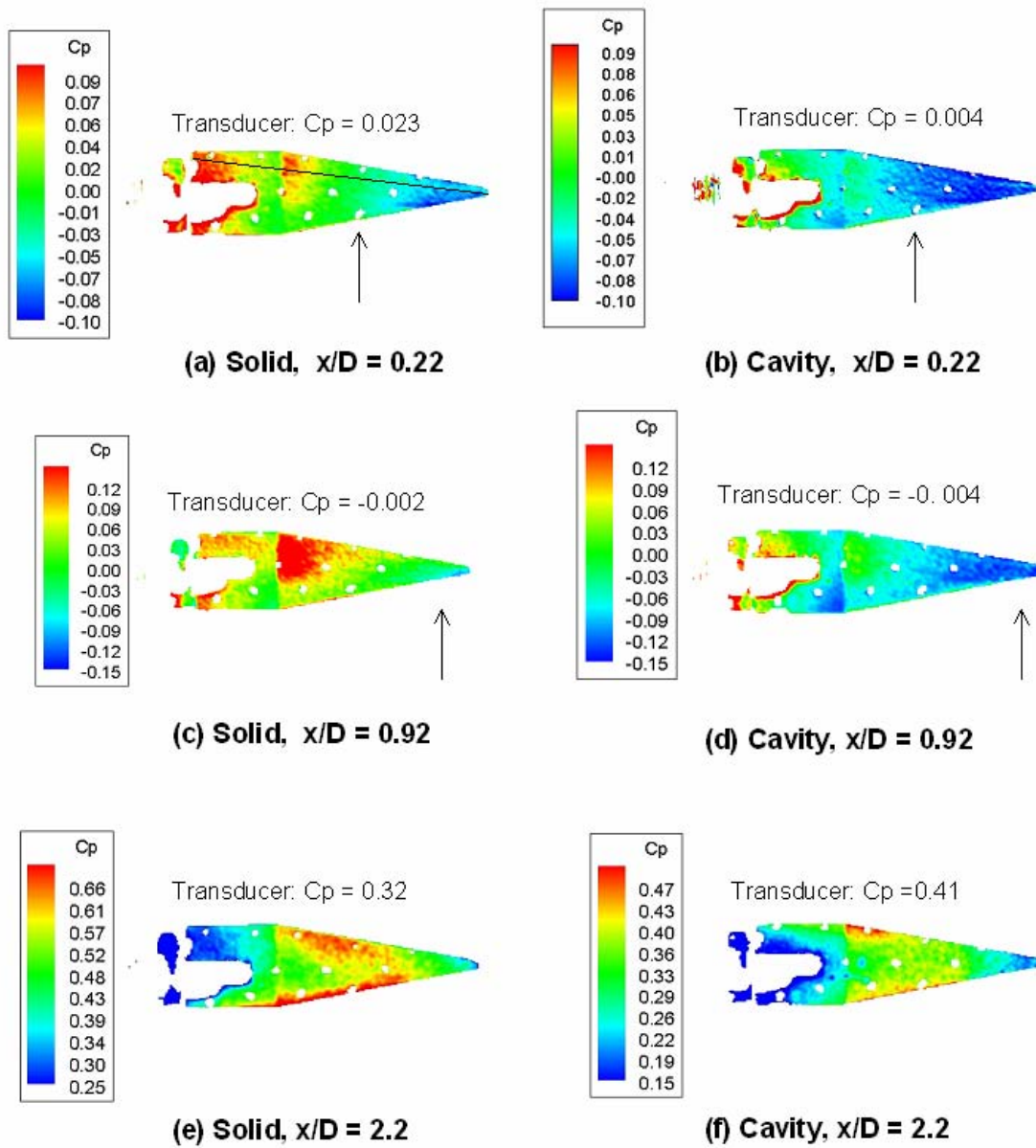


Figure 45: PSP profiles of the store at various axial positions

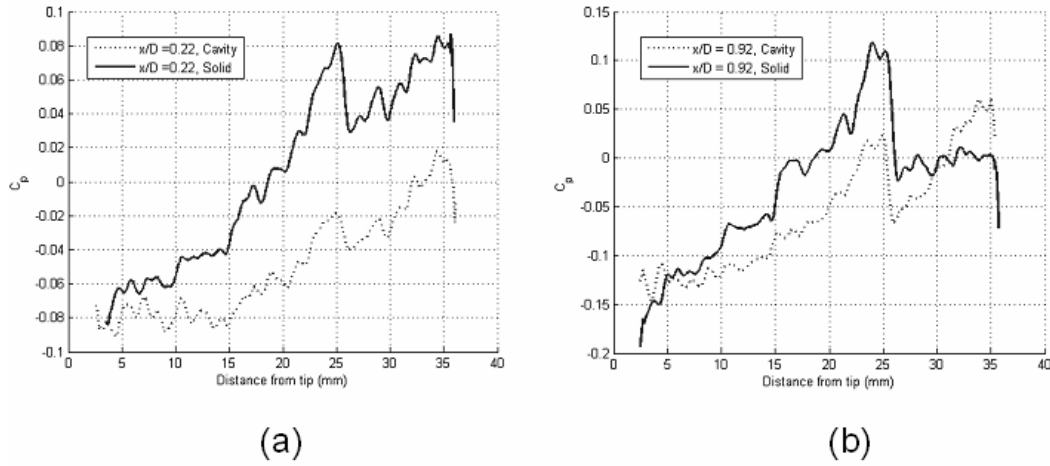


Figure 46: Pressure on the store from PSP images: (a)  $x/D = 0.22$ , (b)  $x/D = 0.92$

## Section 5 – Frequency Analysis

### *Pressure Transducer Frequency Analysis.*

Table 1 demonstrates that transducer data was taken in a similar manor as the research of Janssen and Dutton in Reference 14, which produced the PSD plots presented in Figure 7. Figure 47 shows a sample time trace from the transducer located in the vehicle's cavity for  $x/D = 0$  (Figure 47 shows 200 points of the 100,000 data file). Figure 48 shows transducer data converted to PSDs for various positions using the process outlined in Table 1. To be able to compare to Janssen and Dutton, the pressure was changed to kPa and the x-scale was made identical. In addition, Janssen and Dutton chose to multiply the PSD by frequency "...so that the fluctuating energy content at the corresponding frequency is more clearly visible (14:607)." Therefore, to maintain consistency, the same approach was used here. They determined a Strouhal number of

Table 1: Comparison of PSD processes

	Janssen and Dutton	Current
<b>Test Conditions</b>		
-- Geometry	Cylinder	Cone
-- Diameter (mm)	63.5	21.75
-- Mach	2.46	2.93
-- Velocity (m/s)	350	600
<b>Data Acquisition</b>		
-- Sample size	4,000,000	100,000
-- Sample Rate (kHz)	166	200
-- Low Pass Filter	50 kHz	40 kHz
-- Filter type	20-pole Butterworth	9-pole Butterworth
<b>FFT</b>		
-- Windows	Hanning	Hanning
-- Overlap	50%	50%
-- Bin size	8192	8192
-- Freq Resolution (Hz)	20.3	24.4

0.092 based off the characteristic peak frequency of 500 Hz seen in Figure 7. Using the flow conditions for this research, a Strouhal number of 0.092 corresponded to a frequency around 2,500 Hz. Although some minor peaks can be seen at this frequency in the PSDs in Figure 48, there is nothing as strong as their 500 Hz peak. Figure 48(a) is a PSD of the case  $x/D = -1.5$ , where the store was fully inserted in the cavity. This case excited a signal at about 7 kHz that corresponds to a Strouhal number of 0.25, which is reasonable. Similarly, Figure 48(b) is a PSD of the case of  $x/D = -0.92$ , where the store was partially inserted into the cavity. This caused the spike to decrease in magnitude

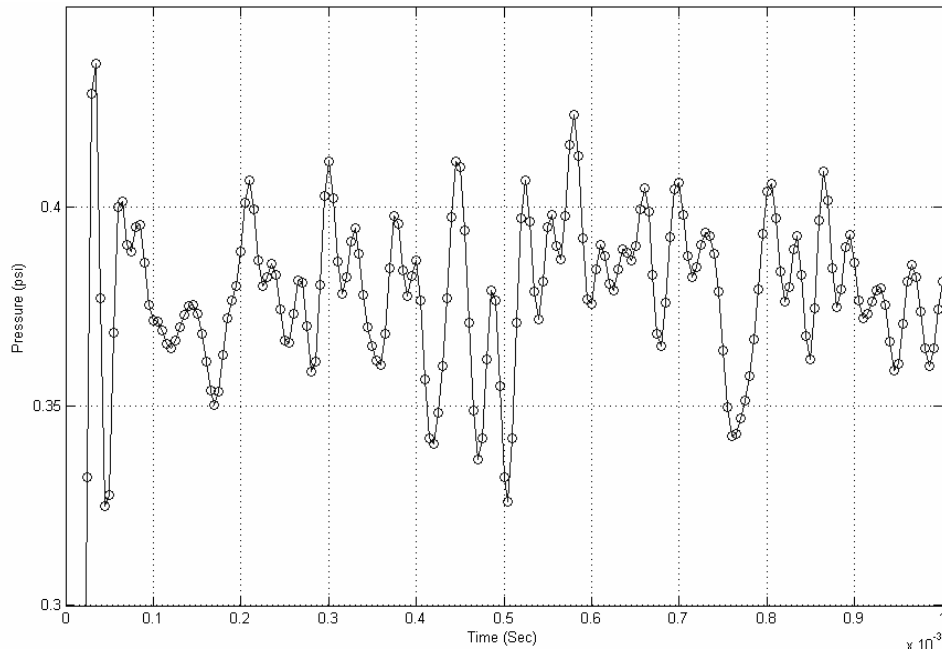


Figure 47: Sample time trace of vehicle's cavity pressure with store at  $x/D = 0$

slightly. Once the store was fully outside the cavity,  $x/D = 0$ , the 7 kHz frequency was no longer excited as can be seen in Figure 48(c). For this case, most of the energy was concentrated from 10 kHz to 40 kHz, which corresponds to Strouhal numbers from 0.39 to 1.44, which is still reasonable. All axial positions farther away produced PSDs very similar to Figure 48(c). Figure 48(d) is also for  $x/D = 0$ , but it is presented here for two reasons. First, as can be seen in Figures 48(a), (b) and (c) there are strong spikes at 10 kHz intervals. This was associated with the data acquisition system, but was not detected until after these data runs were processed. These spikes were created because the wind tunnel conditions were sampled at a rate for 10 kHz on a separate data acquisition board. When this board initiated a new data set, it caused a spike to be recorded on the data boards used by the transducers in the cavity and on the store. A Labview engineer

confirmed this phenomenon. This problem was fixed for the data run used to create Figure 48(d), which does not have these spikes. These features on the previous PSDs should be ignored. Figure 48(d) also demonstrates that the results were repeatable because except for these spikes, Figure 48(c) and (d) are very similar. Therefore, we can conclude that when the store is inserted into the cavity it excites the 7 kHz frequency range. This signal decreases as the store exits the cavity. Once the store was at the exit plane, this signal was no longer significant and then the cavity experiences mostly energy above 10 kHz.

An attempt was made to obtain frequency data from Schlieren images. However, multiple obstacles were encountered during this process. The initial plan was to use the *readavi* command in Matlab to convert the avi files into a matrix of intensities. However, the avi file format that the X-Vision camera software used was incompatible with Matlab. It was also incompatible with multiple movie editing software packages. According to the IDT technical help department, they do not recommend avi file format for high-speed files. They recommend the mrf file format, but Matlab cannot read this format. Therefore, the avi files were converted to bitmaps. Each bitmap was read into Matlab and processed individually. Due to the workload, only 10,000 frames were used to process the data. A sample time trace from this process can be seen in Figure 49, which shows only 100 data points of the 10,000 points used. This time trace represents one pixel's intensity over time. Unlike the transducer time trace in Figure 47, which had multiple data points on each cycle, the Schlieren intensity fluctuated often with no points



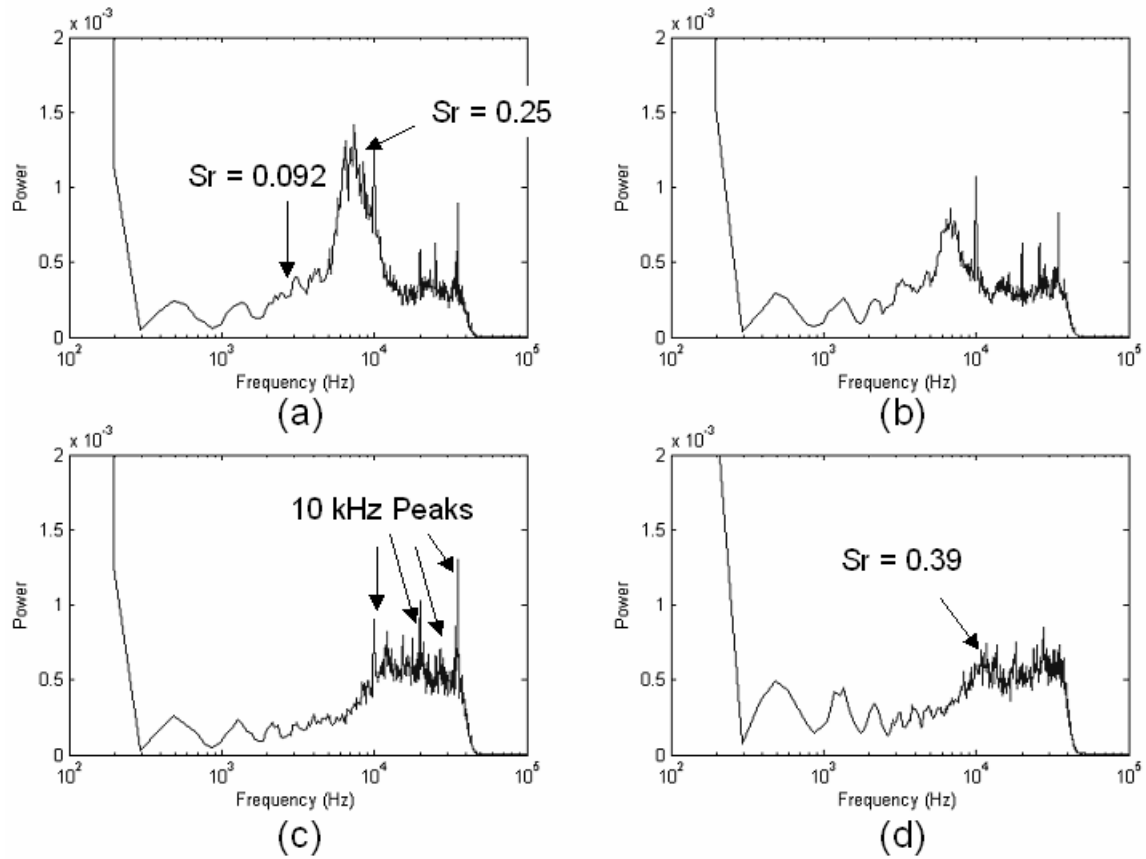


Figure 48: PSD from cavity transducer: (a)  $x/D = -1.5$ , (b)  $x/D = -0.92$ , (c)  $x/D = 0$ , (d)  $x/D = 0$  with no data acquisition feedback

in between. Therefore it was concluded the fluctuations were a result of noise in the camera and not the flow. To try to reduce this problem, an average over a  $3 \times 3$  grid around the pixel of interest was performed and then the data was converted into the frequency domain. Several points were investigated. Figure 50 presents a series of images taken at 94.5 kfps of the solid vehicle model with no store. These 12 images are a snap shot of the 10,000 frames analyzed. The Xs on the first image represent points that were investigated using the Schlieren frequency analysis. The point closest to the base is

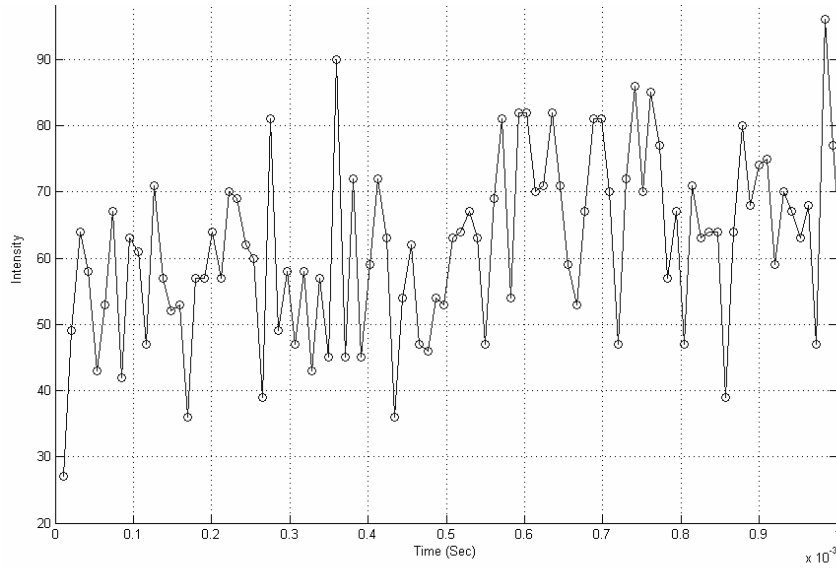


Figure 49: Sample time trace of pixel intensity over time from a Schlieren image

at a location of  $x/D = 0.22$  and  $y/D = 0.22$ . The exact same point was chosen for a series of images for the cavity model. These points were chosen with the intention of producing a frequency spectrum that could be compared with the PSDs of the cavity's pressure presented earlier. The PSDs that resulted from these points can be seen in Figure 52(a) and (b). The results produced no useful information that could be compared to the pressure transducer PSDs. Indeed, the energy level increased with the frequency, but this may be a result of the noise. Therefore, a point was chosen that visually appeared to have a stronger frequency signal. The second X on Figure 50 is at a location of  $x/D = 2.0$  and  $y/D = 0.22$ . This point was chosen in order to capture the fluctuations in the reattachment shock. Additionally, the eighth frame has a point circled. This point was examined because inside of the circle there is a turbulent structure that can be seen convecting

down stream. The frequency analysis of these points did not produce any better results than the previous two. In addition, a series of images were analyzed with a store present. 12 sample images of this series can be seen in Figure 51. Again an X is used to indicate a point investigated. The same location was chosen as the previous analysis without a store,  $x/D = 0.22$ ,  $y/D = 0.22$ , to allow comparison to the previous results. The PSD from this analysis can be seen in Figure 52(d). The results were virtually the same, with no useful information. On the sixth image in Figure 52, there is a white circle. This location was investigated because the reattachment shock was observed pulsing at this location. Again the results were almost identical as the previous points.

Although the Schlieren process worked, it did not produce useful data for this experiment. The reasons for this are many. First, as one can see in Figure 49, the intensity only varied over approximately 30 of 256 possible intensities in gray scale. The second problem was that the Schlieren process is an integrative process. Every density gradient over the collimated light bends the rays of light. In this case the mirrors were 24 feet apart, yet we were only interested in the flow behind a 21.75 mm cone. Therefore, every variation in between the mirrors affected the overall intensity. If the camera settings were adjusted so that all of the intensity scale used, then perhaps this process would have produced better results.

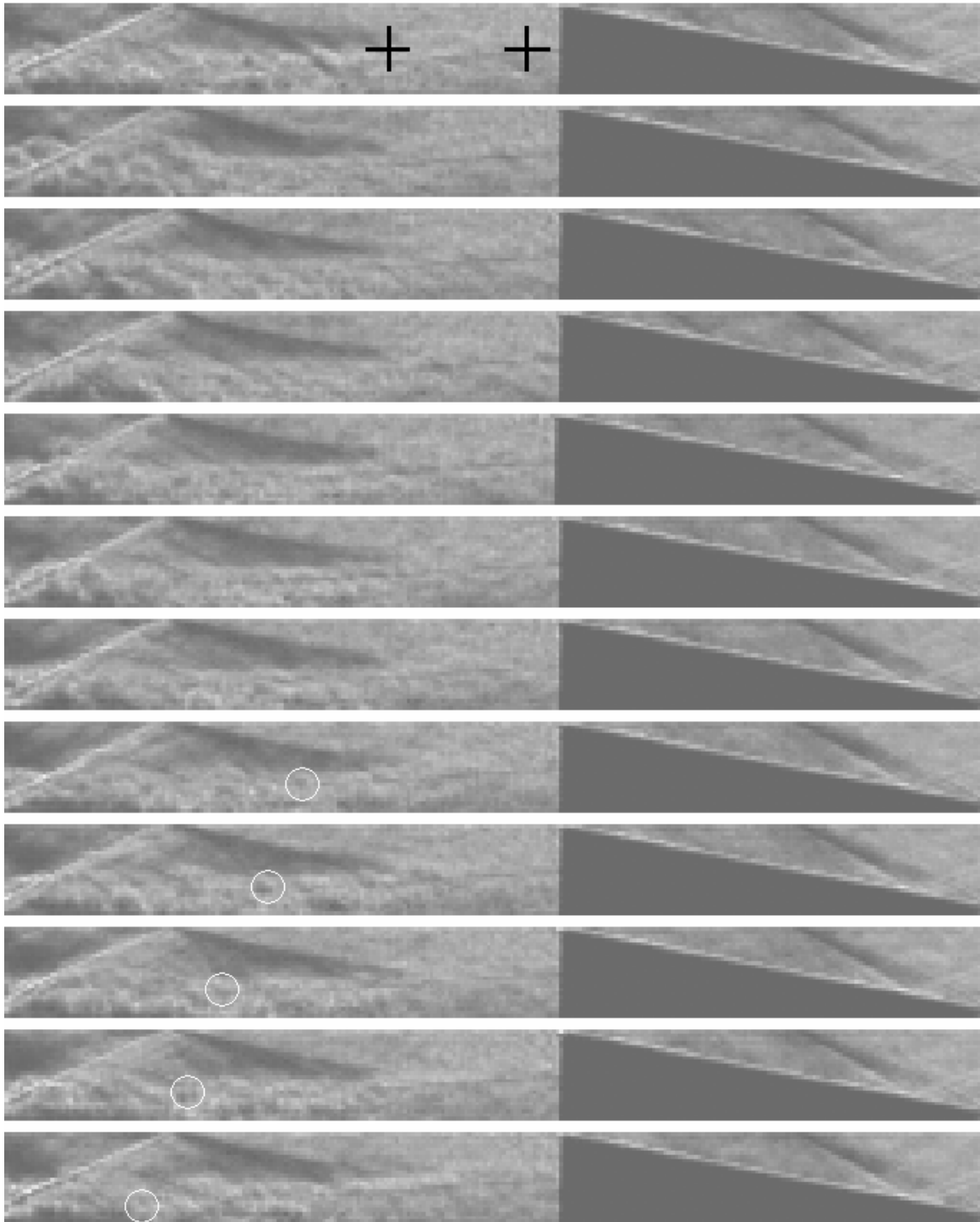


Figure 50: Schlieren images of solid vehicle model taken at 94.5 kfps. Xs on first image indicate locations investigated using Schlieren PSD technique

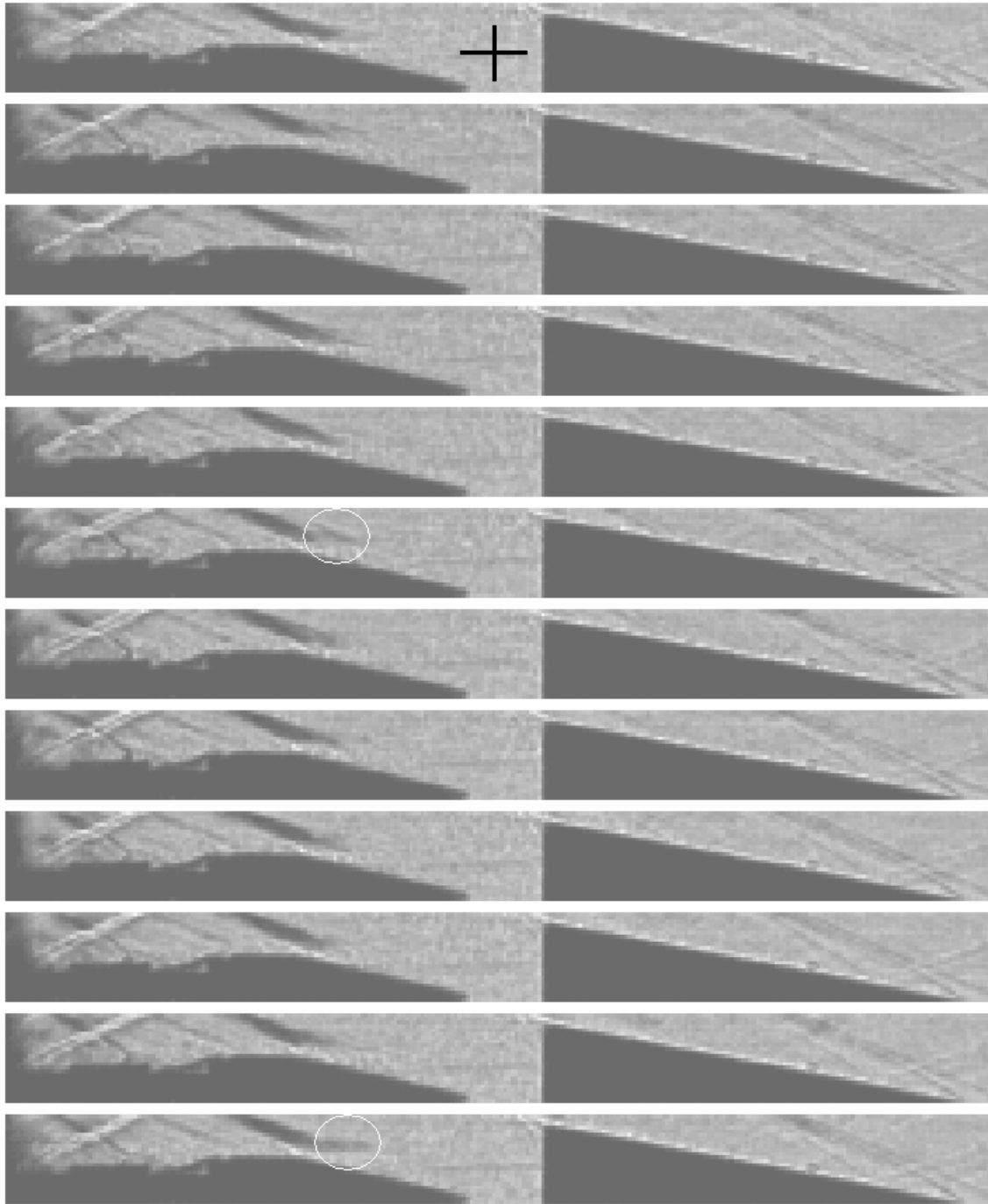


Figure 51: Schlieren images of solid vehicle model with store at  $x/D = 0.22$ , taken at 94.5 kfps. Xs on first image indicate locations investigated using Schlieren PSD technique

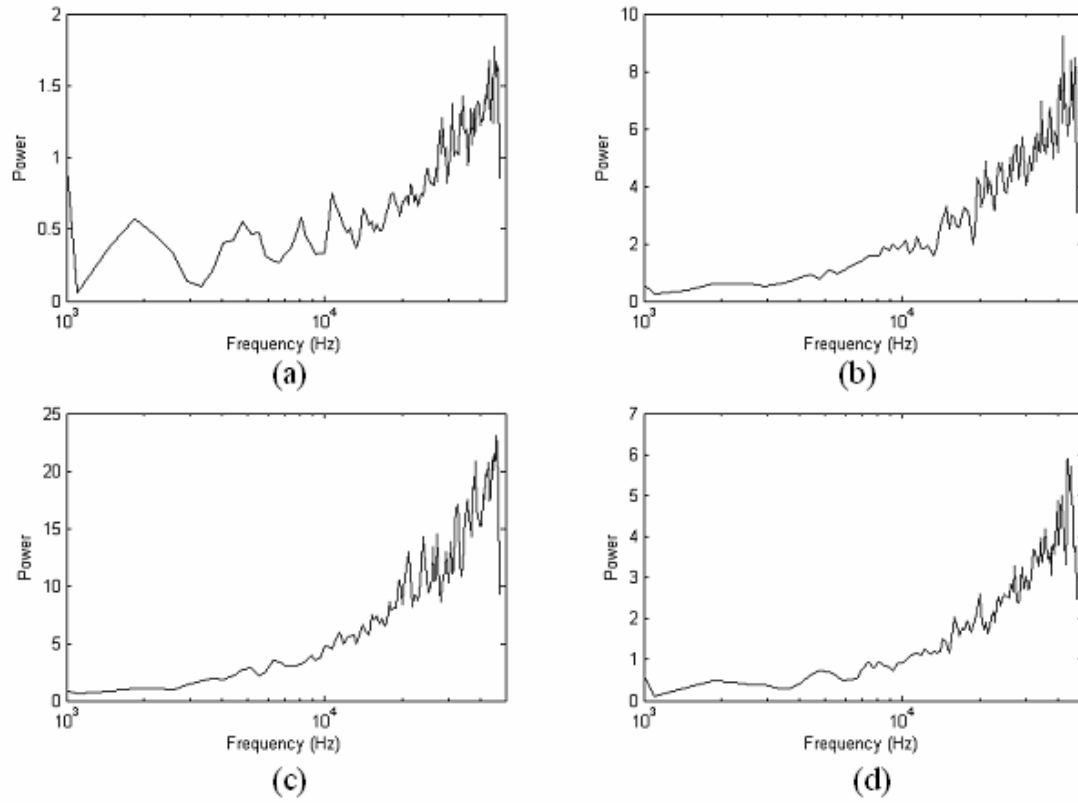


Figure 52: Schlieren PSDs based off of 10,000 images: (a)  $x/D = 0.22$  for cavity model and no store, (b)  $x/D=0.22$  for solid model and no store, (c)  $x/D = 2.0$  for solid model and no store, (d)  $x/D = 0.22$  for solid model with store at  $x/D = 0.22$

## **V. Conclusions and Recommendations**

### **Section 1 - Conclusions of Research**

This research highlighted the fundamental issues associated with releasing a store out of the aft of a supersonic vehicle. Schlieren images, high-speed pressure transducers and PSP were used to investigate this problem. One of the most basic questions that needed to be answered was how can the vehicle be mounted in the wind tunnel without affecting the base flow. Therefore, a diamond-shaped strut supporting a cone in a Mach 2.93 flow was investigated. Although the effects of this strut were observable, this research has demonstrated that these effects can be quantified and minimized.

Additionally, the effects of the store released from an aft cavity were very noticeable and documented. The effects of an aft cavity on the vehicle model were less pronounced, but appeared to lower the pressure felt by the store. Finally, the frequency analysis found a characteristic frequency associated with the store inserted into the cavity as well as documented the high frequency signals when the store was in the wake.

Schlieren images indicated that the diamond-shaped strut caused the reattachment shock to move toward the base, creating a non-axisymmetric shock. Also PSP profile images of the vehicle and strut revealed a strong interaction of the oblique shock created by the strut and the conical shock created by the vehicle. This caused a high-pressure region on the surface of the conical vehicle model. Likewise, the rear face of the strut created an expansion fan, which caused a low-pressure zone on the rear of the conical surface. This suggests that it would be difficult to use this particular strut to determine

forces and moments acting on the cone. A thinner diamond-strut would mitigate these effects. However PSP images of the vehicle's base demonstrated that the strut did not affect the base pressure in any significant manner, nor did it affect the store pressure significantly.

When the store was in the vehicle the base pressure approximated that of a solid cone. As the store was move aft the base pressure increased due to the decrease in turning angle of the expansion fan on the vehicle. The store had a maximum impact at  $x/D = 0.5$ , where there was a 20% increase in coefficient of pressure. From this point the store had decreasing effects. The sonic point was estimated at  $x/D = 1.85$ , which effectively indicated the termination point of the store's influence on the vehicle's base pressure.

The cavity's effects were less pronounced. The Schlieren images showed little change in shock location. However, the cavity model had a lip shock when the store was present. Further study is required to determine the specific cause of this feature. The PSP images indicated that the store had lower pressures over its entire length when it was trailing a vehicle with a cavity. Furthermore, the PSP on the store indicated a weaker adverse pressure gradient for a store trailing a vehicle with a cavity. The transducers saw higher standard deviation ratios behind a cavity model. Additionally, pressure transducer analysis indicated the base pressure was lower for the cavity model. This is significant because it is contrary to what previous research found for a subsonic cavity.

The frequency analysis, processed similar to Reference 14, produced two significant findings. First, when the store was inserted into the cavity, it excited a frequency of 7 kHz, which corresponds to a Strouhal number of 0.25. When the store



was removed, there was no significant energy at this frequency. With the store in the wake most of the energy was in the 10 to 40 kHz range with a Strouhal number of 0.39 to 1.44. This is higher than Strouhal numbers from studies of cylindrical afterbodies in supersonic flow..

## **Section 2 - Recommendations for Future Research**

This thesis has formed the foundation for follow-on research. As already stated, there is a CFD study that is being conducted in conjunction with this paper. However, there are many possible experimental studies that can also be done.

### ***Equipment***

AFIT's wind tunnel will be the cornerstone of any future experiments. Therefore, it is recommended that AFIT invest in a midlife upgrade and modifications be made that make it better for axisymmetric studies. This should include a design of new nozzles. A nozzle could be designed to allow a rod-through-the-nozzle design to be used. Also the flow pattern in the test section should be studied to ensure it produces axisymmetric flow. The current nozzle is a 2D nozzle. Previous axisymmetric wake studies used a 3D annular nozzle and test section. When investigating the pressure on the store, a greater pressure change was observed on the sides than behind the strut. This may be an indication of non-axisymmetric flow. The wind tunnel upgrade study should also quantify the percent turbulence expected. The final upgrade should include a PIV system. The Schlieren system has many advantages, but it is an integrative visualization technique. This means that the all density gradients in the collimated light are added up to produce the final image. This may have contributed to the difficulty of obtaining

useful frequency data from the Schlieren system. It would be insightful to look at a crosscut plane of the flow.

Once the wind tunnel is certified for axisymmetric flow studies, a detailed study of supports should be undertaken. The vehicle should be mounted at different points on the strut. The length, width and sweep angle should be varied. The sweep angle decreases the strength of the shock. However, it also turns the flow. For this reason a strut with no sweep should be investigated. It is absolutely critical to have every model perfectly aligned to do axisymmetric wake research and a technique to ensure this must be developed. For example, the University of Illinois used oil droplets to observe the flow down the cylinder. A similar technique should be developed for AFIT's wind tunnel.

#### ***Follow-on Supersonic Ejection Research.***

Future research should only be continued when the wind tunnel and support are ready. Then, there are countless variations one can pursue concerning aft ejections. A possible first step would be to investigate variations in size of the store. In order for the store to have a greater effect, the cone angle should be increase. This will get more surface area closer to the vehicle's base. Also, I recommend varying the size of the store's diameter. It is believed that the store used in this research was too small. The store slipped through the reattaching shocks. If it were 75% the size of the vehicle instead of 42%, then its effects would have been more pronounced. After the store research, one could vary the size and shape of the cavity to determine its effects more clearly. This research found the cavity decreased base pressure. Future research should verify this result with a more comprehensive study. Finally, with the above experiments

as a basis, one could pursue variations in angle of attack, collect force and moment data, and finally attempt a dynamic separation. Obviously, it would be desirable to have the store move during the data acquisition. A dynamic store would entrain more flow due to the no-slip condition on the wall of the store. The road ahead has countless options. This thesis should be used as a foundation to build upon.

## Appendix A: Pressure Transducer Specifications



### ULTRAMINIATURE THIN LINE IS® PRESSURE TRANSDUCERS

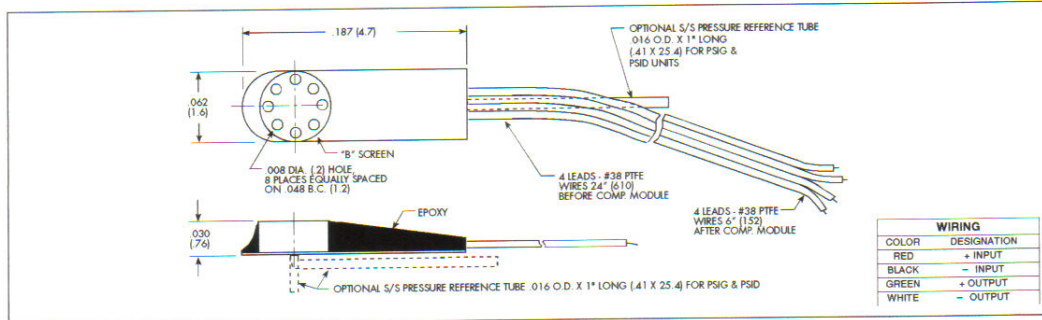
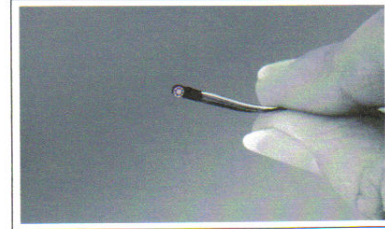
#### LQ-062 SERIES

- Ideal For Wind Tunnel Applications
- Excellent Static And Dynamic Performance
- High Natural Frequency

#### LE-062 SERIES

- High Temperature Capabilities -65°F + 450°F
- Excellent Static And Dynamic Performance
- High Natural Frequency

The LQ/LE Series demonstrates Kulite's ability to provide pressure transducers suited for adaptation into custom packages. These devices can be integrated into various test articles such as fan blades, engine nozzles of various types, etc. The features of these transducers include small foot print, high natural frequency, extreme resistance to vibration and shock, and wide temperature range.



INPUT	1.7	3.5	7	17	35	70 BAR
Pressure Range	25	50	100	250	500	1000 PSI
Operational Mode	Absolute, Gage, Sealed Gage, Differential			Absolute, Sealed Gage		
Over Pressure	2 Times Rated Pressure With No Change In Calibration					
Burst Pressure	3 Times Rated Pressure					
Pressure Media	All Nonconductive, Noncorrosive Liquids or Gases					
Rated Electrical Excitation	10 VDC/AC					
Maximum Electrical Excitation	15 VDC/AC					
Input Impedance	1000 Ohms (Min.)					
OUTPUT	1000 Ohms (Nom.)					
Output Impedance	100 mV (Nom.)					
Full Scale Output (FSO)	± 5 mV (Typ.)					
Residual Unbalance	± 0.1% FSO BFSL (Typ.) ± 0.5% FSO (Max.)					
Combined Non-Linearity, Hysteresis and Repeatability	± 0.1% FSO BFSL (Typ.) ± 0.5% FSO (Max.)					
Resolution	Infinitesimal					
Natural Frequency (KHz) (Typ.)	240	300	380	550	700	1000
Acceleration Sensitivity % FS/g Perpendicular	5.0x10 <sup>-4</sup>	3.0x10 <sup>-4</sup>	1.5x10 <sup>-4</sup>	1.0x10 <sup>-4</sup>	6.0x10 <sup>-5</sup>	4.0x10 <sup>-5</sup>
Transverse	6.0x10 <sup>-5</sup>	4.0x10 <sup>-5</sup>	2.0x10 <sup>-5</sup>	9.0x10 <sup>-6</sup>	6.0x10 <sup>-6</sup>	3.0x10 <sup>-6</sup>
Insulation Resistance	100 Megohm Min. at 50 VDC					
ENVIRONMENTAL	LQ SERIES -65° F to 250° F (-55° C to 120° C) LE SERIES -65° F to 450° F (-55° C to 235° C)					
Operating Temperature Range	LQ SERIES 80° F to 180° F (25° C to 80° C) Any 100° F Range Within The Operating Range on Request LE SERIES 80° F to 450° F (25° C to 235° C)					
Compensated Temperature Range	± 1% FS/100° F (Typ.)					
Thermal Zero Shift	± 1% FS/100° F (Typ.)					
Thermal Sensitivity Shift	10,000g. (Max.)					
Steady Acceleration	10-2,000 Hz Sine, 100g. Max.					
Linear Vibration	4 Leads 38 AWG 30" Long					
PHYSICAL	.2 Gram (Nom.) Excluding Module and Leads					
Electrical Connection	Fully Active Four Arm Wheatstone Bridge Dielectrically Isolated Silicon on Silicon					
Weight						
Sensing Principle						

Note: Custom pressure ranges, accuracies and mechanical configurations available. Dimensions are in inches. Dimensions in parenthesis are in millimeters. Continuous development and refinement of our products may result in specification changes without notice - all dimensions nominal. (D)

# Piezoresistive Pressure Transducer

## Model 8530C-15, -50 and -100

- 15 to 100 psia, 225 mV Full Scale
- Absolute Reference

**ENDEVCO<sup>®</sup>**  
**MODEL**  
**8530C**

### DESCRIPTION

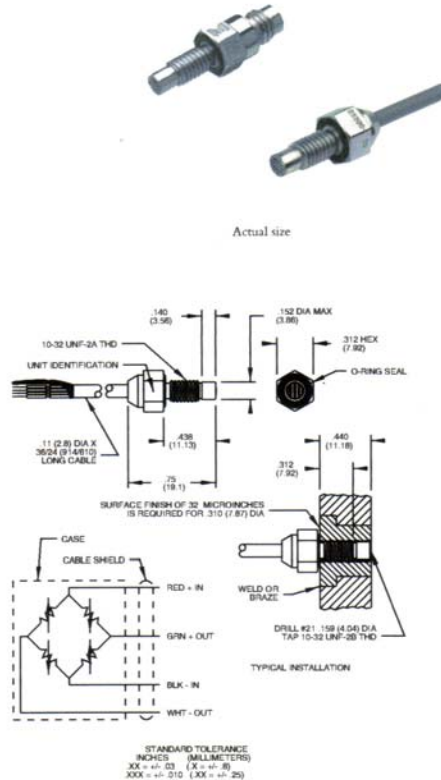
The ENDEVCO<sup>®</sup> Model 8530C is a miniature, high sensitivity piezoresistive pressure transducer for measuring absolute pressure. The volume behind the diaphragm is evacuated and glass sealed to provide an absolute pressure reference. Full scale output is 225 mV with high overload capability and high frequency response. It is available in ranges from 15 psia to 100 psia. The Model 8530B is available for higher pressure ranges.

ENDEVCO pressure transducers feature a four-arm strain gage bridge ion implanted into a unique sculptured silicon diaphragm for maximum sensitivity and wideband frequency response. Self-contained hybrid temperature compensation provides stable performance over the temperature range of 0°F to 200°F (-18°C to +93°C). ENDEVCO transducers also feature excellent linearity (even to 3X range), high shock resistance, and high stability during temperature transients.

The Model 8530C has been used successfully in many blast test situations. For this application, a protective coating is recommended to eliminate photoflash sensitivity and provide particle impingement protection. This coating does not degrade the superior dynamic response characteristics of the sensor.

The Model 8530C is available with Metric M5 mounting thread as 8530C-XXM5 on special order. Also available with integral four-pin connector as Model 8530C-XXM37.

ENDEVCO Model 136 Three-Channel System, Model 4428A or 4430A Signal Conditioner, or OASIS 2000 Computer-Controlled System are recommended as signal conditioner and power supply.



### SPECIFICATIONS

**CERTIFIED PERFORMANCE:** All specifications assume +75°F (+24°C) and 10 Vdc excitation unless otherwise stated. The following parameters are 100% tested. Calibration data, traceable to the National Institute of Standards and Technology (NIST), is supplied.

	Units	8530C-15	-50	-100
RANGE [1]	psia	0 - 15	0 - 50	0 - 100
SENSITIVITY [1]	mV/psi Typ (Min)	15.0 (9.3)	4.5 (2.8)	2.25 (1.4)
COMBINED: NON-LINEARITY, NON-REPEATABILITY,				
PRESSURE HYSTERESIS [2]	% FSO RSS Max	0.50	0.40	0.40
Non-Linearity, Independent	% FSO Typ	0.15	0.1	0.1
Non-Repeatability	% FSO Typ	0.1	0.1	0.1
Pressure Hysteresis	% FSO Typ	0.1	0.1	0.1
ZERO MEASURAND OUTPUT [3]	mV Max	±20	±20	±20
ZERO SHIFT AFTER 3X RANGE	±% 3X FSO Max	0.2	0.2	0.2
THERMAL ZERO SHIFT				
From 0°F to 200°F (-18°C to +93°C)	±% FSO Max	3	3	3
THERMAL SENSITIVITY SHIFT				
From 0°F to 200°F (-18°C to +93°C)	±% Max	3	3	3



**ENDEVCO**  
**MODEL**  
**530C**

## Piezoresistive Pressure Transducer

### SPECIFICATIONS—continued

TYPICAL PERFORMANCE CHARACTERISTICS: The following parameters are established from testing of sample units.

	Units	8530C-15	-50	-100
RESONANCE FREQUENCY	Hz	180 000	320 000	500 000
NON-LINEARITY AT 3X RANGE	% 3X FSO	1.0	1.0	1.0
ZERO SHIFT WITH MOUNTING TORQUE 15 lbf-in. (1.7 Nm)	% FSO	0.2	0.5	0.5
THERMAL TRANSIENT RESPONSE PER ISA-S37.10, PARA. 6.7, PROCEDURE I [4]	psi/°F	0.003	0.003	0.010
	psi/°C	0.005	0.005	0.018
PHOTOFLASH RESPONSE [5]	Equiv. psi	0.1	0.3	0.6
WARM-UP TIME [6]	ms	1	1	1
ACCELERATION SENSITIVITY	Equiv. psi/g	0.00015	0.00015	0.00015
BURST PRESSURE (Diaphragm)	psia Min	75	250	400
CASE PRESSURE [7]	psia Min	1000	1000	1000

#### ELECTRICAL

FULL SCALE OUTPUT	225 mV typical (140 mV minimum) at 10.0 Vdc
SUPPLY VOLTAGE [8]	10.0 Vdc recommended, 15 Vdc maximum
ELECTRICAL CONFIGURATION	Active four-arm piezoresistive bridge
POLARITY	Positive output for increasing pressure
RESISTANCE	
Input	2600 ohms typical, 1700 ohms minimum
Output	1500 ohms typical, 2200 ohms maximum
Isolation	100 megohms minimum at 50 Volts; leads to case, leads to shield, shield to case
NOISE	5 microvolts rms typical, dc to 50 000 Hz; 50 microvolts rms maximum, dc to 50 000 Hz

#### MECHANICAL

CASE, MATERIAL	Stainless Steel (17-4 PH CRES)
CABLE, INTEGRAL	Four conductor No. 32 AWG Teflon® insulated leads, braided shield, silicone jacket, 30 ±6 in (760 ±150mm)
DEAD VOLUME (+) PORT	0.0003 cubic inches (0.005 cc)
MOUNTING/TORQUE	10-32 UNF-2A threaded Case 0.438 inch (11.12 mm) long/15 ± 5 lbf-in (1.7 ±0.6 Nm)
WEIGHT	2.3 grams (cable weighs 9 grams/meter)

#### ENVIRONMENTAL

MEDIA [9]	Internal seals are epoxy compatible with clean dry gas media. Media is exposed to CRES, ceramic, silicon, Parylene C, epoxy, silicone rubber, and the O-Ring. For use in water or corrosive media, contact the factory for modifications and installation precautions which may be taken to extend service life
TEMPERATURE [10]	-65°F to +250°F (-54°C to +121°C)
VIBRATION	1000 g pk
ACCELERATION	1000 g
SHOCK	20 000 g, 100 microsecond haversine pulse
HUMIDITY	Isolation resistance greater than 100 megohms at 50 volts when tested per MIL-STD-202E, Method 103B, Test Condition

#### CALIBRATION DATA

Data supplied for all parameters in Certified Performance section. Optional calibrations available for all parameters in Typical Performance section.

#### ACCESSORY

EHR93	O-RING, VITON
3027A-120	CABLE ASSEMBLY

#### OPTIONAL ACCESSORIES

EHR96	O-RING, FLUOROSILICONE
24328	4 CONDUCTOR SHIELDED CABLE

#### NOTES

- 1 psi = 6.895 kPa = 0.069 bar.
- FSO (Full Scale Output) is defined as transducer output change from 0 psia to + full scale pressure.
- Zero Measurand Output (ZMO) is the transducer output with 0 psia applied.
- Significantly higher thermal transient errors occur if the excitation voltage exceeds 10 Vdc. For sensitive phase change studies, many users reduce the excitation to 5 Vdc or even 1 Vdc.
- Per ISA-S37.10, Para. 6.7, Proc. II. The metal screen partially shields the silicon diaphragm from incident radiation. Accordingly, light incident at acute angles to the screen generally increases the error by a factor of 2 or 3.

6. Warm-up time is defined as elapsed time from excitation voltage "turn on" until the transducer output is within ±1% of reading accuracy.
7. Case pressure identifies media containment pressure in the event of diaphragm rupture.
8. For best results when using excitation voltages other than 10.0 Vdc, it is recommended that the transducer be calibrated at the desired excitation during manufacture. Otherwise larger thermal errors may occur, especially at voltages above 10 Vdc.
9. O-Ring, ENDEVCO part number EHR93 PARKER 5-125, compound V747-75 (VITON®) is supplied unless otherwise specified on purchase order. Fluorosilicone O-ring, Endevco part number EHR96 Parker material L677-70, for leak tight operation below 0°F is available on special order.
10. Maintain high levels of precision and accuracy using Endevco's factory calibration services. Call Endevco's inside sales force at 800-982-6732 for recommended intervals, pricing and turn-around time for these services as well as for quotations on our standard products.

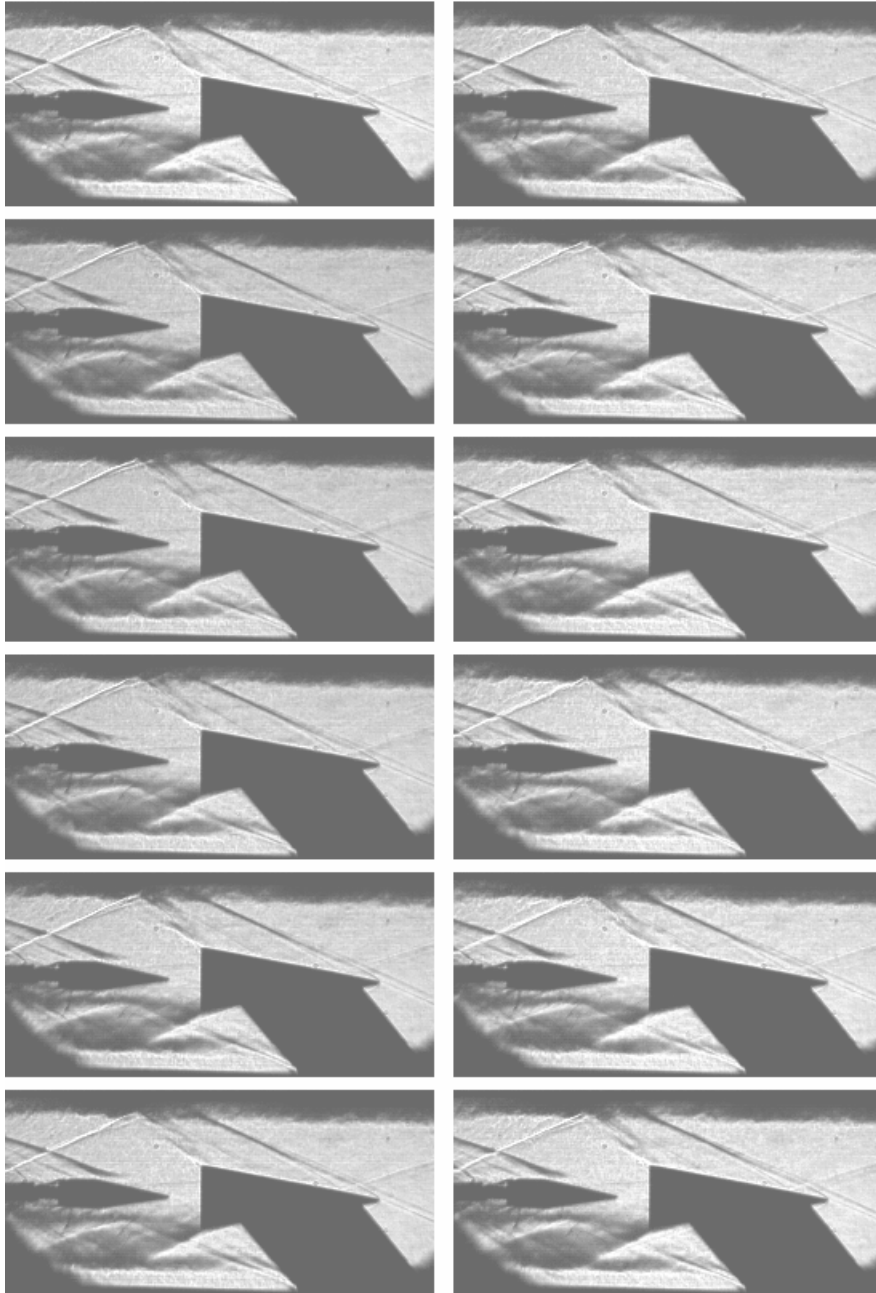
NOTE: Tighter specifications are available on special order.

Continued product improvement necessitates that Endevco reserve the right to modify these specifications without notice. Endevco maintains a program of constant surveillance over all products to ensure a high level of reliability. This program includes attention to reliability factors during product design, the support of stringent Quality Control requirements, and compulsory corrective action procedures. These measures, together with conservative specifications have made the name Endevco synonymous with reliability.

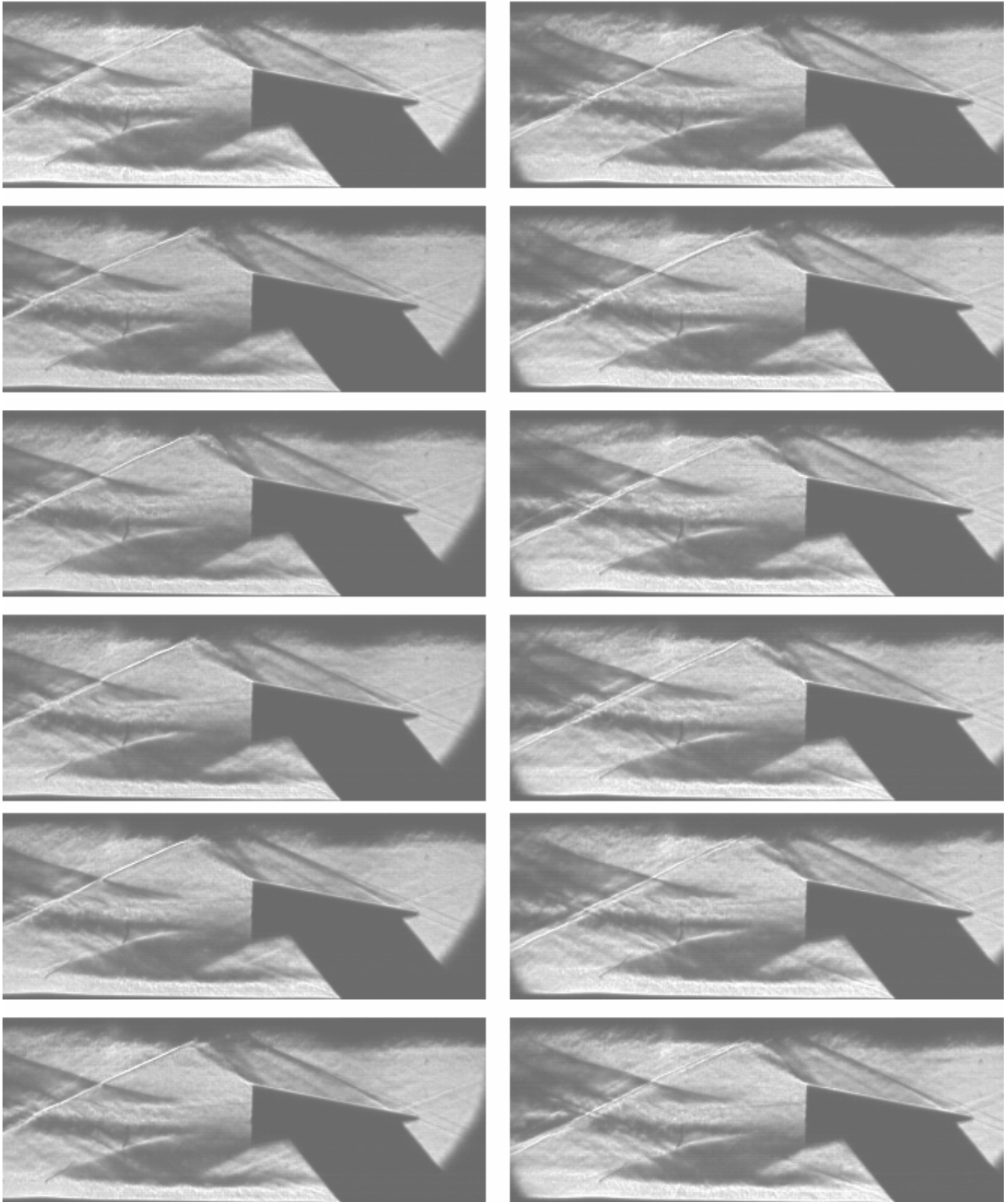
ENDEVCO CORPORATION, 30700 RANCHO VIEJO ROAD, SAN JUAN CAPISTRANO, CA 92675 U.S.A. (949) 982-6732 FAX (949) 492-8181 Telex (949) 661-7221

## Appendix B: Additional Schlieren Images

Images of solid vehicle with store at  $x/D = 0.22$ , taken at 20.1 kfps

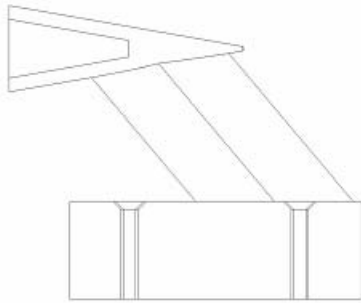


Images of solid vehicle taken at 20.1 kfps

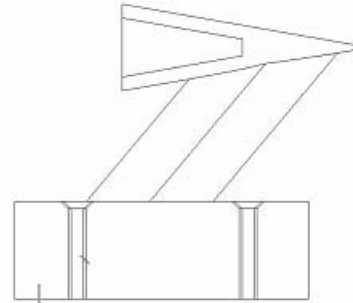




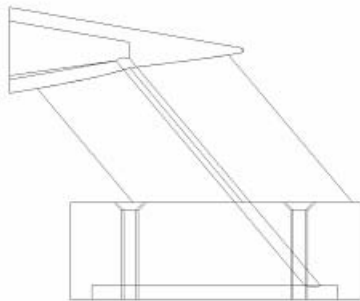
## Appendix C: Profile Views of Various Vehicle Models



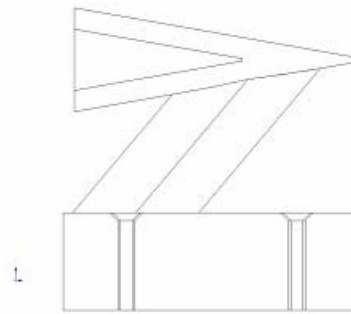
C1



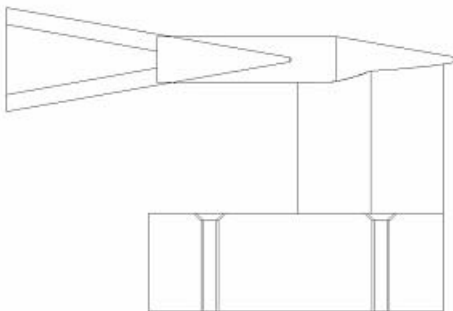
C2



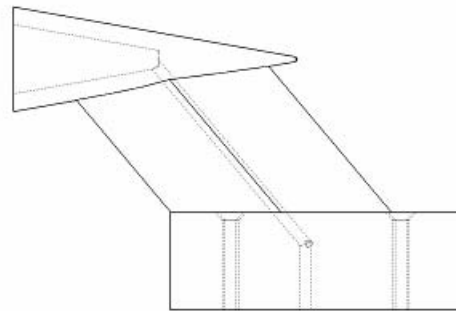
C3



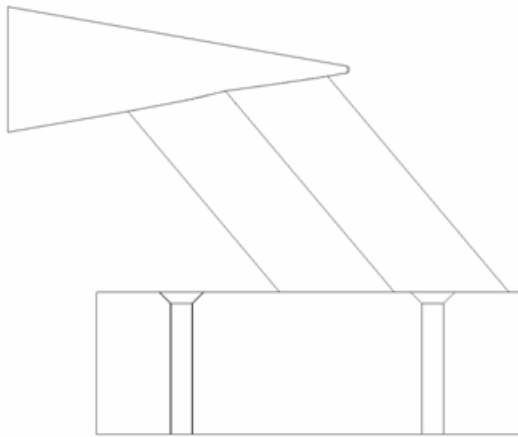
C4



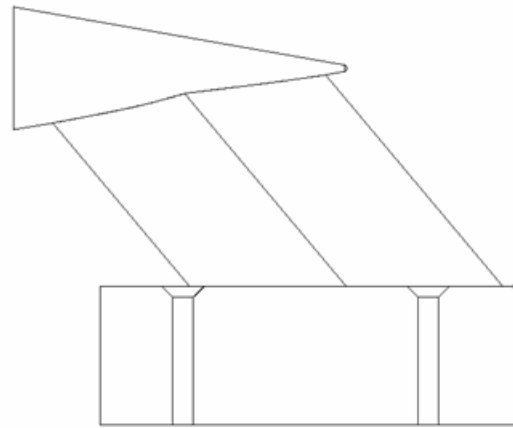
C5



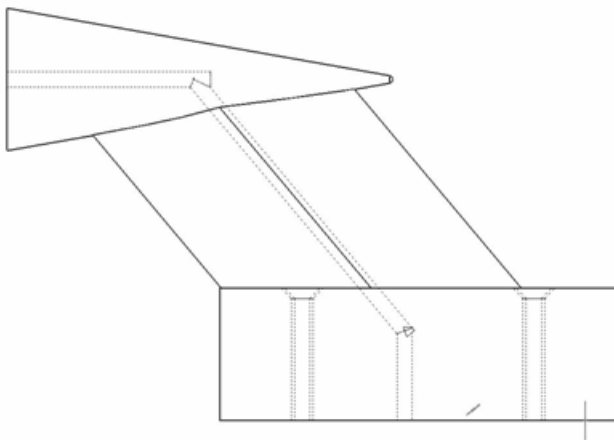
C6



S1



S2



S3

## Bibliography

1. Anderson, John D. *Modern Compressible Flow*. 3<sup>rd</sup> Ed. Boston: McGraw-Hill, 2003
2. August, Henry and others. "Leeside Separation of Hypersonic Weapons." ADA318744: Hughes Aircraft, 1993.
3. Bell, J. H. and others. "Surface Pressure Measurements Using Luminescent Coatings." *Annual Review of Fluid Mechanics*, Vol 33: 155-206, (2001).
4. Burt, M., P. Miller and J. Agrell. "Transonic and Supersonic Flowfield Measurements about Axisymmetric Afterbodies for Validation of Advanced CFD Codes." AGARD Conference Proceedings, CP-535: 9-1 to 9-28 (July 1994).
5. Crafton, Jim et al. "Simultaneous Measurements of Pressure and Deformation on a UCAV in the SARL." AIAA paper 2005-1028.
6. Czarnecki, K.R. and M. W. Jackson. "Effects of Nose Angle and Mach Number on Transition on Cones at Supersonic Speeds." NACA Technical Note 4388 (September 1958).
7. Dayman, B., Jr. *Optical Free-Flight Wake Studies*. JPL Technical Report 32-364. Pasadena, 1 October 1962.
8. ----. *Simplified Free-Flight Testing in a Conventional Wind Tunnel*. JPL Technical Report 32-346. Pasadena, 1 November 1962.
9. Dayman, B., Jr. and D. W. Kurtz. "Forebody Effects on Drogue Drag in Supersonic Flow." *Journal of Spacecraft*, Vol. 5 No. 11: 1335-1340 (November 1968).
10. Dutton, J.C. and others. "Recent Progress on High-Speed Separated Base Flows." AIAA Paper 1995-0472.
11. Hama, Francis R. "Experimental Studies on the Lip Shock." *AIAA Journal*, Vol. 6, no. 2: 212-219 (1968).
12. Herrin, J. L. and J. C. Dutton. "Supersonic Base Flow Experiments in the Near Wake of a Cylindrical Afterbody." *AIAA Journal*, Vol 32, #1: 77-83 (January 1994).

13. ----. "Supersonic Near-Wake Afterbody Boattailing Effects on Axisymmetric Bodies." *Journal of Spacecraft and Rockets*, Vol 31, No 6:1021-1028 (November-December 1994).
14. Janssen, J. R. and J. C. Dutton. "Time-Series Analysis of Supersonic Base-Pressure Fluctuations." *AIAA Journal*, Vol 42, #3: 605-613 (March 2004).
15. Kastengren, A.L. and J. C. Dutton. "Large-Structure Topography in a Three-Dimensional Supersonic Base Flow." *AIAA Journal*, Vol. 43, no. 43: 1053-1063 (5 May 2005).
16. Mather, T. and J. C. Dutton. "Base Bleed Experiments with a Cylindrical Afterbody in Supersonic Flow." *AIAA 95-0062*, January 1995.
17. Martellucci, A. and A. Agnone. "Measurements of the Turbulent Near Wake of a Cone at Mach 6," *AIAA Journal*, Vol 10, #3: 385-391 (March 1966).
18. Mishra, J. N. and A. K. Chatterjee. "Following Body Effects on Base Pressure in Supersonic Stream." *Journal of Spacecraft and Rockets*, Vol. 12, No. 5: 317 (May 1975).
19. Molezzi, M. J. and Dutton, J. C. "Study of the Near-Wake Structure of a Subsonic Base Cavity Flowfield Using PIV." *AIAA 1993-3040*.
20. Newman, Gary and others. "On the Aerodynamics/Dynamics of Store Separation from Hypersonic Aircraft." *AIAA Paper 1992-2722*.
21. "Pressure Sensitive Paints: Products." ISSI web site, 10 November 2005, [http://innssi.com/psp/index\\_products\\_psp\\_summaryhtm](http://innssi.com/psp/index_products_psp_summaryhtm).
22. Raymer, Daniel P. *Aircraft Design: A Conceptual Approach*. Washington, D.C.: AIAA, Inc., 1989.
23. Schlichting, H. and K. Gersten. *Boundary Layer Theory*. 8<sup>th</sup> Ed. Berlin: Springer, 2000.
24. Tanner, Mauri. Base Pressure in Supersonic Flow: Further Thoughts about a Theory. *AIAA Journal*, Vol 30, No2 :565-566 (1992).
25. Tannerhill, J. C. *Computational Fluid Mechanics and Heat Transfer*. 2<sup>nd</sup> Ed. Philadelphia: Taylor and Francis, 1997.
26. Van Raalte, M. H. and B. W. van Oudheusden. "An Analytical Model to Describe the Reynolds Number Effects In Supersonic Base Flow." *AIAA Paper 2001-2785*.

27. Settles, G.S. *Schlieren and Shadowgraph Techniques*. Berlin: Springer Publishing, 2001.

REPORT DOCUMENTATION PAGE				Form Approved OMB No. 074-0188	
<p>The public reporting burden for this collection of information is estimated to average 1 hour per response, including the time for reviewing instructions, searching existing data sources, gathering and maintaining the data needed, and completing and reviewing the collection of information. Send comments regarding this burden estimate or any other aspect of the collection of information, including suggestions for reducing this burden to Department of Defense, Washington Headquarters Services, Directorate for Information Operations and Reports (0704-0188), 1215 Jefferson Davis Highway, Suite 1204, Arlington, VA 22202-4302. Respondents should be aware that notwithstanding any other provision of law, no person shall be subject to a penalty for failing to comply with a collection of information if it does not display a currently valid OMB control number.</p> <p><b>PLEASE DO NOT RETURN YOUR FORM TO THE ABOVE ADDRESS.</b></p>					
1. REPORT DATE (DD-MM-YYYY) 22-12-2005		2. REPORT TYPE Master's Thesis		3. DATES COVERED (From - To) June 2004 - December 2005	
4. TITLE AND SUBTITLE  Wind Tunnel Study of Interference Effects Relating to Aft Supersonic Ejection of a Store				5a. CONTRACT NUMBER	
				5b. GRANT NUMBER	
				5c. PROGRAM ELEMENT NUMBER JON #05-304	
6. AUTHOR(S)  Jung, Timothy P, Major, USAF				5d. PROJECT NUMBER	
				5e. TASK NUMBER	
				5f. WORK UNIT NUMBER	
7. PERFORMING ORGANIZATION NAMES(S) AND ADDRESS(S) Air Force Institute of Technology Graduate School of Engineering and Management (AFIT/EN) 2950 Hobson Way, Building 640 WPAFB OH 45433-8865				8. PERFORMING ORGANIZATION REPORT NUMBER  AFIT/GAE/ENY/06-04	
9. SPONSORING/MONITORING AGENCY NAME(S) AND ADDRESS(ES) Air Force Research Laboratory, Air Vehicles Directorate Weapons Integration Team 2130 Eighth St, WPAFB, OH, 45433				10. SPONSOR/MONITOR'S ACRONYM(S)	
				11. SPONSOR/MONITOR'S REPORT NUMBER(S)	
12. DISTRIBUTION/AVAILABILITY STATEMENT  APPROVED FOR PUBLIC RELEASE; DISTRIBUTION UNLIMITED.					
13. SUPPLEMENTARY NOTES					
<p><b>14. ABSTRACT</b> An investigation into the issues surrounding the release of a store into a supersonic wake was conducted. A 10-degree half-angle cone was used to model the carrier vehicle as well as the store. The store was 42% than the vehicle. The experiments were conducted at a freestream Mach number of 2.93 and at zero degrees angle of attack. This study analyzed the effects of a support or strut mounted under the wind tunnel model. Research was conducted on the effects of a store at various positions in the wake, as well as the effects of a rear cavity in the carrier. Real-time sequences of Schlieren images were used to obtain a visual understanding of these effects. Fast-response pressure transducers and pressure-sensitive paint (PSP) provided pressure information on the carrier vehicle and store models. Visualizations showed the strut caused the reattachment shock to move closer to the base. Transducers recorded a slight decrease in mean and an increase in standard deviation of pressure behind the strut. From a PSP profile image, the interaction of the oblique shock of the strut with the model's conical shock was found to create a vertical pressure gradient. However, base pressure was only modestly affected. The store was manually moved to various axial positions behind the vehicle. The store caused the pressure to rise as the store moved aft. At distance equal to half of the vehicle's base diameter, the store had maximum effect, causing an increase in the base's coefficient of pressure. As the store moved farther aft, the store had diminishing effects. The cavity was found to have minimal effects on the flowfield. The cavity caused a drop in the vehicle's base pressure and the pressure on the store. When the store was inserted into the cavity it excited a characteristic frequency corresponding to a Strouhal number of 0.25, but when the store was removed there were no significant frequencies signals in this range.</p>					
15. SUBJECT TERMS					
16. SECURITY CLASSIFICATION OF:			17. LIMITATION OF ABSTRACT	18. NUMBER OF PAGES	19a. NAME OF RESPONSIBLE PERSON
a. REPORT	b. ABSTRACT	c. THIS PAGE			Mark F. Reeder, Ph.D., Civ
U	U	U	UU	118	19b. TELEPHONE NUMBER (Include area code) (937) 255-3636, ext 4530 (mark.reeder@afit.edu)